UNIVERSITY OF SOUTHAMPTON

FACULTY OF ENGINEERING SCIENCES & MATHEMATICS

School of Ocean & Earth Sciences

Growth & Motion at the Weddell Sea Ice Edge

by

Martin Jonathan Doble

Thesis for the degree of Doctor of Philosophy

September 2007

UNIVERSITY OF SOUTHAMPTON

ABSTRACT

FACULTY OF ENGINEERING SCIENCES & MATHEMATICS
SCHOOL OF OCEAN & EARTH SCIENCES

Doctor of Philosophy

GROWTH & MOTION AT THE WEDDELL SEA ICE EDGE

by Martin Jonathan Doble

The formation of sea ice in the presence of turbulence was studied using data from drifting buoy deployments and ice sampling in the Weddell Sea during April 2000. The study sought to improve understanding of pancake ice in terms of dynamics, heat fluxes, ice growth rates and mechanisms.

Ice motion at high frequencies was examined using GPS buoy positions at a 20-minute sampling interval. Relative motions of the buoy array were characterised by a marked oscillation at the highest frequencies, with an RMS value two orders of magnitude higher than previously seen in the Weddell Sea. This motion ceased overnight as the pancakes consolidated. Wave forcing, either surface gravity or internal, was postulated as the cause. The oscillation was found to significantly influence the proportions of pancake and frazil ice, though the nature of the ice cover meant that ice production rates were unaffected, in contrast to the enhanced growth this would imply for congelation ice. Momentum transfer parameters were found to be similar to those found for the Greenland Sea Odden ice tongue.

Pancakes were found to be dominantly thickened by over-topping of the surrounding frazil ice crystals, termed ‘scavenging’, and gave rise to distinct morphologies, which were classified. A physical model was developed to describe the evolution of the pancake ice cover to consolidation. Ice production in the pancake/frazil process was found to proceed at approximately double the rate of the equivalent congelation ice cover, or 0.58 times the limiting free-surface frazil production. It was suggested that the discrepancy will seriously impact large-scale modelling attempts to simulate heat and momentum fluxes between the ocean and atmosphere, as well as salt rejection and subsequent water mass modification, though it is acknowledged that further field measurements are required to place some currently empirical parameters into a physical context.

Contents

List of Figures

List of Tables

DECLARATION OF AUTHORSHIP

I, **Martin Jonathan Doble**

declare that the thesis entitled

Growth and motion at the Weddell Sea ice edge

and the work presented in it are my own. I confirm that:

- this work was done wholly or mainly while in candidature for a research degree at this University;
- where any part of this thesis has previously been submitted for a degree or any other qualification at this University or any other institution, this has been clearly stated;
- where I have consulted the published work of others, this is always clearly attributed;
- where I have quoted from the work of others, the source is always given. With the exception of such quotations, this thesis is entirely my own work;
- I have acknowledged all main sources of help;
- where the thesis is based on work done by myself jointly with others, I have made clear exactly what was done by others and what I have contributed myself;
- Parts of this work have been published as:

Doble, M. J. and P. Wadhams (2006). Dynamical contrasts between pancake and pack ice, investigated with a drifting buoy array. *J. Geophys. Res.* **111**(C11S24): doi:10.1029/2005JC003320.

Doble, M. J., M. D. Coon and P. Wadhams (2003). Pancake ice formation in the Weddell Sea. *J. Geophys. Res.* **108**(C7): doi: 10.1029/2002JC001373.

Signed: ……..

Date:……..…….

Acknowledgements

Thanks are primarily due to the people who made the field experiment on which this thesis is based such a success. First amongst these must be the Captain and crew of the *Polarstern*, operated by the Alfred Wegener Institute (AWI), who were so helpful during buoy deployments and ice sampling. I also thank the Cruise Leader, Wolf Arntz (AWI), for being so generous with ship time for the experiment. Sincere thanks are due to Max Coon (North West Research Associates) who responded at very short notice to accompany me on my first sea ice experiment in the role of 'grizzled advisor'. He was inspirational in demonstrating how to plan and conduct an experiment and I also acknowledge his pivotal role in identifying the pancake formation mechanism elucidated here, during discussions on board. Oli Peppe (Dunstaffnage Marine Laboratory, DML) made massive efforts to assemble and test the buoy electronics on board the ship in the first weeks of the cruise, despite zapping our only spare microprocessors on the first day. I'll never forget the expression on his face. Duncan Mercer (DML) burnt similar amounts of midnight oil back on land, developing the control software for the buoys in the ridiculously short time available (as usual). Thanks to Peter Wadhams for first employing me after my Masters degree, introducing me to the field of Polar Oceanography and for many successful and satisfying collaborations since with various European partners and to my supervisor, Neil Wells, for pushing me just hard enough to get this done.

The thesis was begun at the Scott Polar Research Institute and continued at the Department of Applied Mathematics and Theoretical Physics, Cambridge. Final work and writing up was done at the Laboratoire d'Océanographie de Villefranche (LOV), and I thank directors Michel Glass and Louis Legendre for the opportunity to join them in the sunny South of France as a Visiting Scientist.

I was supported by three grants during the lengthy gestation of this thesis: UK Natural Environment Research Council grant GR3/12592, the EU Framework 5 GreenICE project (Greenland Arctic Shelf Ice and Climate Experiment, Project No. EVK2-2001-00280) and the EU Framework 6 project DAMOCLES (Developing Arctic Modelling and Observing Capabilites for Long-term Environment Studies, Project No. 018509).

Abbreviations

ACC	Antarctic Circumpolar Current
ASL	Above Sea Level
AWI	Alfred Wegener Institut
BADC	British Atmospheric Data Centre
CTD	Conductivity, Temperature, Depth
CW/CCW	Clockwise / Counterclockwise
DKP	Differential Kinematic Parameter
DML	Dunstaffnage Marine Laboratory
DTU	Danish Technical University
ECMWF	European Centre for Medium-range Weather Forecasting
FFT	Fast Fourier Transform
GPS/DGPS	Global Positioning System / Differential GPS
GTS	Global Telecommunication System
HF/LF	High Frequency / Low Frequency
HSVA	Hamburgische Schiffbau-Versuchsanstalt GmBH
LEO	Low-Earth Orbit
LIMEX	Labrador Ice Margin Experiment
LPF	Low Pass Filter
LW/SW	Long Wave/ Short Wave
MIZ	Marginal Ice Zone
MIZEX	Marginal Ice Zone Experiment
OBL	Ocean Boundary Layer
PSD	Power Spectral Density
RMS	Root Mean Square
ROV	Remotely Operated Vehicle
SA	Selective Availability
SEDNA	Sea-ice Experiment: Dynamic Nature of the Arctic
SIE	Solid Ice Equivalent
SLP	Sea Level Pressure
SSM/I	Special Sensor Microwave/Imager
SVPB	Surface Velocity Profiling Barometer

Symbols

A	Area
C_E	Turbulent exchange coefficient
C_f	Cloud correction factor
C_p	Specific heat capacity of air
e_i	Saturation vapour pressure over ice
e_p	Water vapour pressure
e_S	Saturation vapour pressure over water
f_p	Area fraction of pancakes
f_f	Area fraction of frazil
f_{ow}	Area fraction of open water
f_{floe}	Area fraction of broken floe pieces
F_w	Ocean heat flux
h	Thickness (ice thickness)
h_p	Pancake thickness (solid ice equivalent)
h_f	Frazil slick thickness (solid ice equivalent)
H	Equivalent thickness (volume / area)
H_s	Significant wave height
I_0	Short-wave radiation penetrating the ice
k	Frequency index
L	Latent heat of fusion, latent heat of vaporisation, latent heat of sublimation
m_n	Spectral moment, n^{th} order
p	Atmospheric pressure
q_a	Specific humidity at air temperature
q_s	Saturation specific humidity at the ice surface temperature
Q_B	Downwelling long wave flux
Q_C	Conductive heat flux upward to the ice surface
Q_{CB}	Conductive heat flux through the bottom of the ice
Q_E	Latent heat flux
Q_H	Sensible heat flux
Q_{net}	Net heat flux (positive melts ice)
Q_S	Downwelling short wave radiation flux

Q_{S0}	Global shortwave radiation flux
Q_{up}	Upwelling long wave radiation flux from the ice surface
r_s	Spearman's rank correlation
R	Gas constant for dry air
R^2	Degree of explanation
s	Scale
S_i	Salinity of ice
S_0	Solar constant
t_s	Solar time
T_1	Mean period
T_a	Air temperature
T_{cc}	Fractional cloud cover
T_{melt}	Melting temperature of saline ice
T_0	Ice surface temperature
T_f	Freezing temperature of seawater
T_r	Clear sky transmittance
u, v	Velocity components with respect to the array centroid
x, y	Distances from the array centroid
v_{10}	wind speed at 10 m ASL
V_p	Volume fraction of ice in pancakes
V_f	Volume fraction of ice in frazil slick
w	mixing ratio

α	Wind factor, spectral slope, albedo, lag-1 autocorrelation
δ	Turning angle
δj	Sub-scale interval
Δf	Frequency interval
Δt	Time interval
η	Solar zenith angle
ε	Scavenging efficiency, error, ratio of gas constants for dry air and water vapour
ε_a	Emissivity of air
θ_0	Potential temperature

ι	Solar inclination angle
φ	Latitude
κ_i	Conductivity of saline ice
κ_0	Conductivity of pure ice
λ	Wavelength, Fourier period
ρ_a	Density of moist air
ρ_f	Frazil ice density
ρ_i	Ice density
ρ_w	Water density
σ	Stephan-Boltzmann constant
σ_ε	Variance of residual drift velocity
σ_0	Variance of observed ice drift velocity
Σ	Sum
τ	Solar hour angle
ω	Angular frequency

CHAPTER 1: INTRODUCTION

This section gives a general overview of the formation of Antarctic sea ice, from its turbulent beginnings to the familiar pack ice. The present lack of knowledge concerning the process is highlighted and buoy deployments - designed to examine growth and motion at the advancing ice edge - are described. The aims of the thesis are then set out, and an overview of the thesis structure given.

1.1 The Southern Ocean ice cover

The seasonal variability of the sea ice cover in the Southern Ocean is one of the most climatically important features of the southern hemisphere. The area of the planet's surface involved is enormous: the sea ice extent in the Antarctic varies from a minimum of $4x10^6$ km^2 at the end of summer (mostly confined to thick, deformed, ice in the far south-western corner of the Weddell Sea) to a maximum of $19x10^6$ km^2 in winter. Yet the processes by which the ice forms, especially in the outer part of the pack, are not well understood and have only been studied *in situ* since 1986 (Wadhams *et al.* 1987). Investigations of sea ice have instead tended to concentrate on the more easily-accessible Arctic, where large-scale ice features allow satellite motion-tracking without recourse to expensive *in situ* instrumentation, and the persistence of ice throughout the year allows its study in summer, when most cruises to ice covered regions occur.

Young ice at the Antarctic ice edge is, by definition, a far more transient form and one which requires the deployment of *in situ* instrumentation from cruises during the Austral winter. The ice cover begins to advance northwards from March onwards, when cooling of the ocean surface seaward of the summer ice edge starts to freeze the surface waters. The high turbulence levels of the Southern Ocean do not allow this ice to form the familiar coherent sheet (termed ‘congelation ice’). Ice instead forms as a suspension of unconsolidated crystals, known as frazil or grease ice. These are mixed down into the water by the ocean wind and wave fields, often occurring as linear streaks (Figure 1.1), herded into Langmuir plumes (Dethleff 2005; Kempema and Dethleff 2006) with volume concentration around 20-40% (Martin and Kaufmann 1981; Smedsrud and Skogseth 2006) though values of up to 57% have been observed in the laboratory (Newyear and Martin 1997). The mixing allows the continued exposure of sea surface to the colder air, the maintenance of a high ocean-atmosphere heat flux and consequently a much higher ice production rate than would be achieved under calm conditions.

Early studies of frazil crystal formation rates and processes tended to focus on freshwater cases, since these have direct impact in colder countries, such as blocking the cooling water intakes of Canadian power stations (Osterkamp 1978). There has been a

resurgence of interest in oceanic frazil formation, however, though this has focussed on production in polynyas (Alam and Curry 1998; Smedsrud and Skogseth 2006), and under ice shelves (Smedsrud and Jenkins 2004). Frazil production in polynyas is parameterised in terms of fetch, a threshold wind speed for frazil formation and the frazil collection depth at the downwind edge of the polynya. These have a strong influence on ice production within the polynya and, consequently, how long the polynya remains open and active, but are not applicable to the wave-induced turbulence of the advancing marginal ice zone (MIZ) considered here.

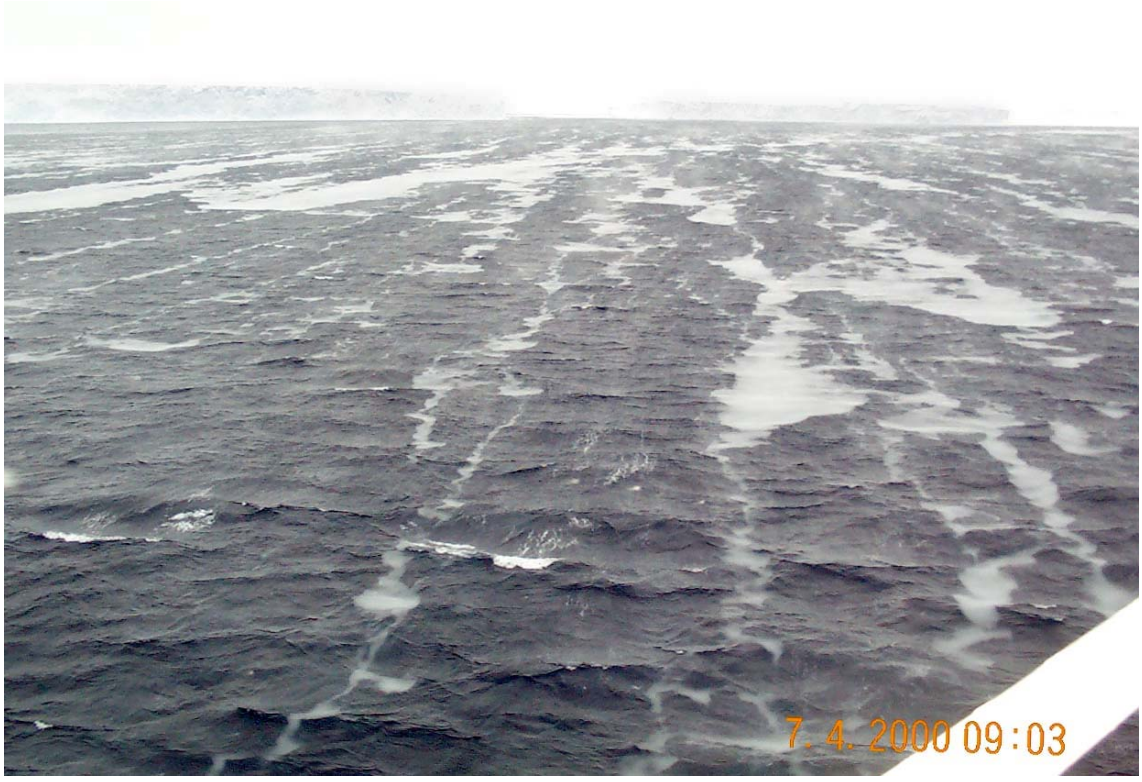

Figure 1.1: Frazil ice forming in a coastal polynya off Kap Norvegia in the Antarctic. Air temperature was -17°C with a wind speed of 20 m s^{-1}.

In the case of ice shelves, rising, supercooled water forms frazil (termed 'platelet ice' in this context) as it flows underneath the ice shelf under buoyancy forcing. Accumulation of this frazil forms 'marine ice', which becomes visible as striking dark-green ice when icebergs, calved from the ice shelf, turn over as they melt (Warren *et al.* 1993).

Figure 1.2: A ‘green’ iceberg, formed from frazil ice accumulating at depth under an Antarctic ice shelf. This iceberg was photographed in open water north of the Weddell Sea ice edge. Also evident are bands of sediment, presumably scavenged by the rising frazil crystals.

In the MIZ, the frazil suspension gradually consolidates into small cakes – known as ‘pancake ice’ – by the agglomeration of the crystals, driven by the absorption of short-wave energy by the frazil slick and augmented by the cyclic compression and rarefaction under the influence of passing troughs and peaks (respectively) of longer waves. Agglomeration is assumed to occur both from below and laterally as the buoyant crystals rise to the surface, with the consolidation being driven by the temperature gradient to the cold atmosphere (Shen *et al.* 2001). A frazil slick has never been observed to be deeper than the pancakes embedded within it, though upward-looking sonars have observed the presence of deep scattering layers in coastal polynyas (Drucker *et al.* 2003), suggesting this does occur in the presence of wind-induced mixing. The frazil crystals are sintered together at their point of contact, minimising their surface free energy (Martin 1981). This overcomes their noted reluctance to stick

together, caused by an enveloping layer of brine (Hanley and Tsang 1984), contrasting with the behaviour of freshwater frazil crystals which rapidly form relatively strong aggregations or “flocs” (Martin 1981). Using shadowgraph techniques, brine has been observed streaming from crystals both as they ascend under buoyancy forcing after their initial formation, and from an established frazil layer (Ushio and Wakatsuchi 1993). This brine drainage continues as the pancakes age, with relatively open structure allowing very rapid salinity reduction compared to the congelation ice equivalent.

The pancakes are initially only a few centimetres in diameter and are known as ‘shuga’ (Figure 1.3) in their earliest agglomerations (Armstrong *et al.* 1973) or ‘dollar pancakes’ (Wadhams and Wilkinson 1999) as the disc form becomes more pronounced. The size of the pancakes is controlled by the dominant wavelength (λ) present. Tank experiments

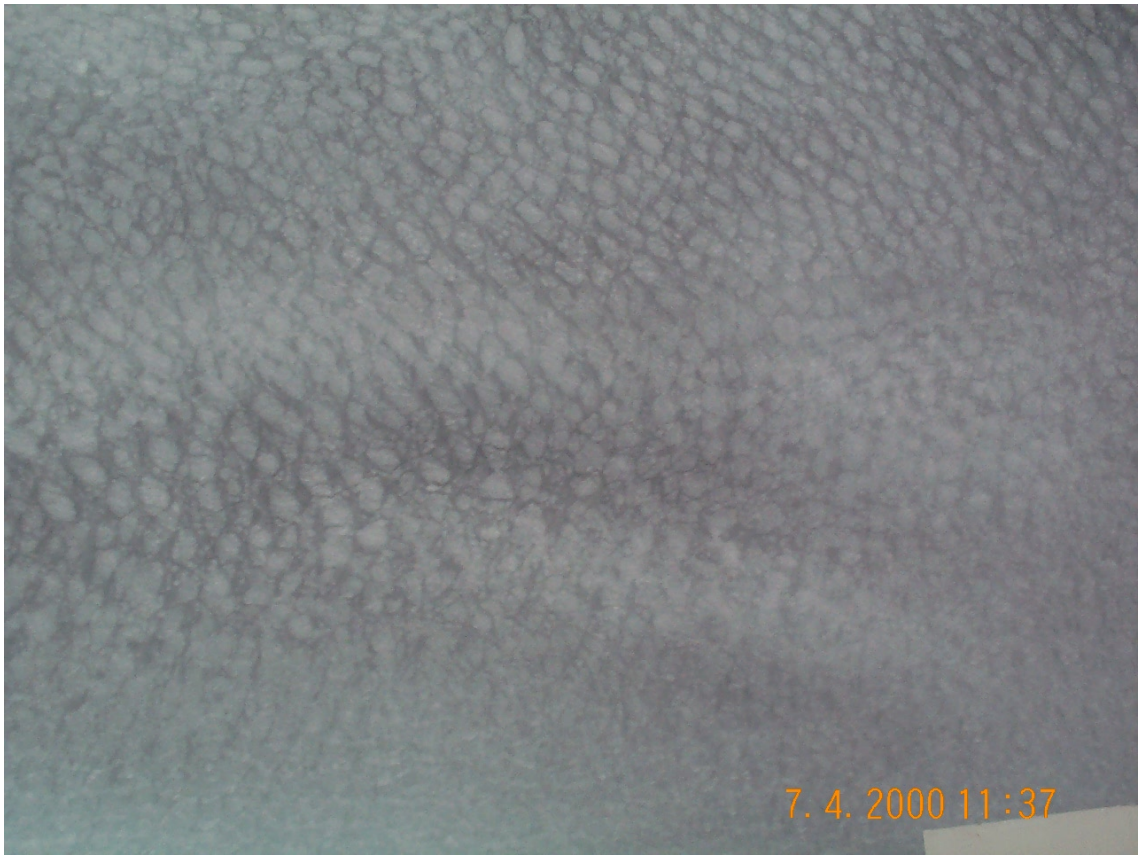

Figure 1.3: Shuga; the first stage in the agglomeration of frazil crystals in the pancake cycle. The photograph was taken looking straight down from the ship’s aft deck, with the individual agglomerations around 5 cm diameter.

suggest that pancakes are approximately 0.01λ in diameter (Leonard *et al.* 1998b) and a theoretical framework which broadly matched this result was developed by Shen *et al.* (2001). Lateral growth occurs by the freezing on of frazil crystals from the surrounding slush and by the agglomeration of other mature pancakes. Frazil is piled onto the edges of the pancakes as they come together, forming slushy ridges up to several centimetres high. Vertical thickening can also occur by rafting one pancake onto another, through either large-scale or local compression.

Figure 1.4: Mature pancake ice, displaying multiple rafting and agglomeration of smaller pancakes. Raised rims are particularly evident in this view. The stick towards the middle of the photograph is one metre long.

The wavelength/pancake size relation continues to evolve as the shortest waves are damped in their progress across the ice cover and the dominant wavelength increases, until pancakes of more than 5 m diameter and 50 cm thickness are observed. Only at a

considerable distance from the ice edge – up to 270 km (Wadhams *et al.* 1987) - is the ocean swell damped enough to allow the pancakes to freeze together to form a continuous ice sheet, termed "consolidated pancake ice". This then thickens, by the usual processes of congelation ice growth on its underside and snowfall on its upper surface, to form the familiar pack ice.

The pancake cycle thus exerts a dominant influence on Antarctic ice types (Weeks 1998) and textural investigations of ice in the central Weddell Sea have revealed that pancake ice growth is the dominant mechanism for pack ice formation in this area (Clarke and Ackley 1984; Gow *et al.* 1987; Lange *et al.* 1989; Lange and Eicken 1991).

The importance of pancake ice formation lies in the fact that an ice cover of reasonable thickness can establish itself despite a high oceanic heat flux (Squire 1998). The ice growth is thought to occur at near the open water rate (Wadhams *et al.* 1987), though quantitative estimates of growth rates during pancake formation are currently entirely lacking. Once the cover cements together to become continuous, growth drops rapidly to the low levels consistent with a *c*.50 cm thick ice cover. This subsequent rate is in fact almost zero in the Weddell Sea, since the oceanic heat flux then almost balances the loss by conduction through the ice (Gordon and Huber 1990). Wadhams *et al.* (1987) estimated that only 4 cm of further ice growth took place after the pancake ice cover consolidated.

This thesis aims to increase our understanding of these early stages of ice growth, using data from a drifting buoy array, deployed into the Weddell Sea pancake ice by the author in April 2000. The next sections detail these buoy deployments and set out the scope of the thesis.

1.2 Data sources

The dearth of knowledge about pancake ice has stemmed largely from the fact that no *in situ* instrumentation had been deployed into a pancake zone, other than three position-only buoys into the Odden region of the Greenland Sea (Wilkinson 2005). Field

experiments in the MIZ instead focussed on instrumenting relatively large floes before recovery a short time afterwards, most notably as part of the MIZEX (Bering Sea, February 1983; Fram Strait, July 1983; Greenland Sea, June-July 1984) and LIMEX (Newfoundland, March 1987 & March 1989) experiments (Wadhams and Squire 1986; Wadhams *et al.* 1988; Liu *et al.* 1992). The only previous experimental data covering the growth of pancake ice and its transition to pack ice came from tank experiments (Shen and Ackley 1995; Leonard *et al.* 1998a; Onstott *et al.* 1998). These suffered from something of a scaling problem, since frazil crystals are 'life-sized' while other parameters are not. Limitations of satellite systems (*i.e*. the Argos system) made the satellite telemetry of large amounts of data impossible and locations were infrequently (three-hourly) and inaccurately (*c*.350 m accuracy) assessed (Geiger *et al.* 1998).

The author therefore proposed and was funded (Natural Environment Research Council Grant No. GR3/12952) to design and deploy an array of six drifting buoys into the advancing ice edge region of the Weddell Sea, during the ANT-17/3 cruise of the Alfred Wegener Institute's research vessel *Polarstern* (Doble *et al.* 2001). The buoys were designed to survive harsh impact conditions while mimicking the response of the pancakes to wind and waves. They were also designed to freeze into the ice once the pancakes consolidated, with a tapered hull shape allowing the buoys to be squeezed up and out of the ice should significant convergence be encountered. Figure 1.5 shows one of buoys afloat, shortly after deployment down the ship's stern ramp.

The buoys were comprehensively instrumented, measuring their GPS position every twenty minutes, meteorological parameters (wind speed and direction, air temperature) every hour and a vertical wave spectrum every three hours. Data were transmitted over the *Orbcomm* low-Earth orbit (LEO) satellite system (Meldrum *et al.* 2000) to cope with the relatively large data volumes generated. A standard MetOcean surface velocity profiling barometer (SVPB) buoy was incorporated in the design, as a backup to the untried and hastily-assembled *Orbcomm* system. The SVPB independently transmitted air pressure data and Argos positions to the Global Telecommunications System (GTS) for use by operational weather forecasting models (Tenhunan *et al.* 2007).

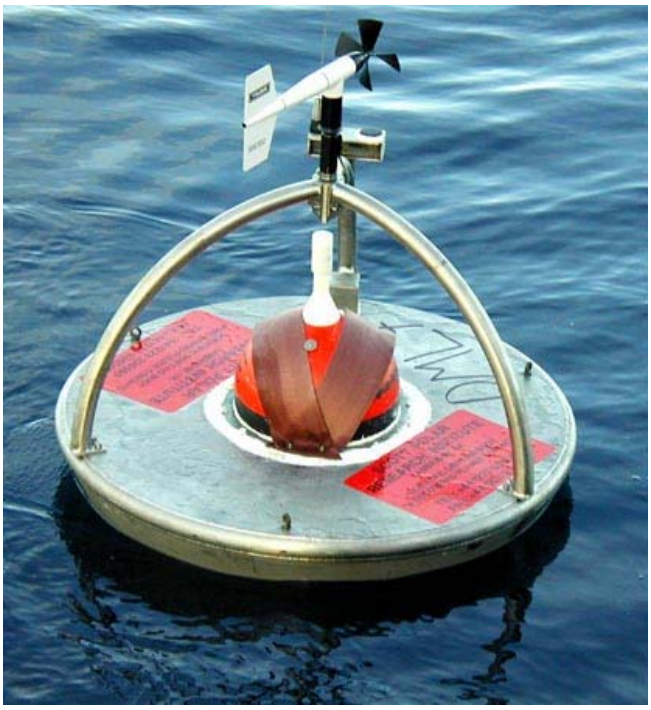

Figure 1.5: One of the six ‘pancake buoys’, afloat in the Weddell Sea. The orange sphere in the middle of the buoy is the self-contained MetOcean SVPB Argos buoy.

The buoys were deployed in a ‘five dice’ pattern; with one buoy at each corner of a *c*.100 km square and the fifth unit in the centre. The array was positioned near the centre of the Weddell Gyre (Kottmeier *et al.* 1997), in order to minimise advection and hence maximise residence time in the ice. An additional unit was deployed *c*.300 km further to the west, to verify that the motion of the main array was representative of the ice edge as a whole. This is subsequently referred to as the “long-scale buoy”. This arrangement was found to provide the best compromise between cost and dynamical information in previous MIZ campaigns (e.g. the MIZEX experiments in the Arctic, 1983-9).

Deployment positions are shown in Figure 1.6, which also shows the ice concentration at their deployment, from passive microwave (SSM/I) satellite data. An algorithm developed by the Danish Technical University (DTU) was used to process the raw SSM/I data as this had been optimised for young, wet ice, such as pancakes (Pedersen

and Coon 2004). The numbers show the nomenclature employed for the buoys, which are numbered sequentially (DML4 – DML9) according to their electronics package.

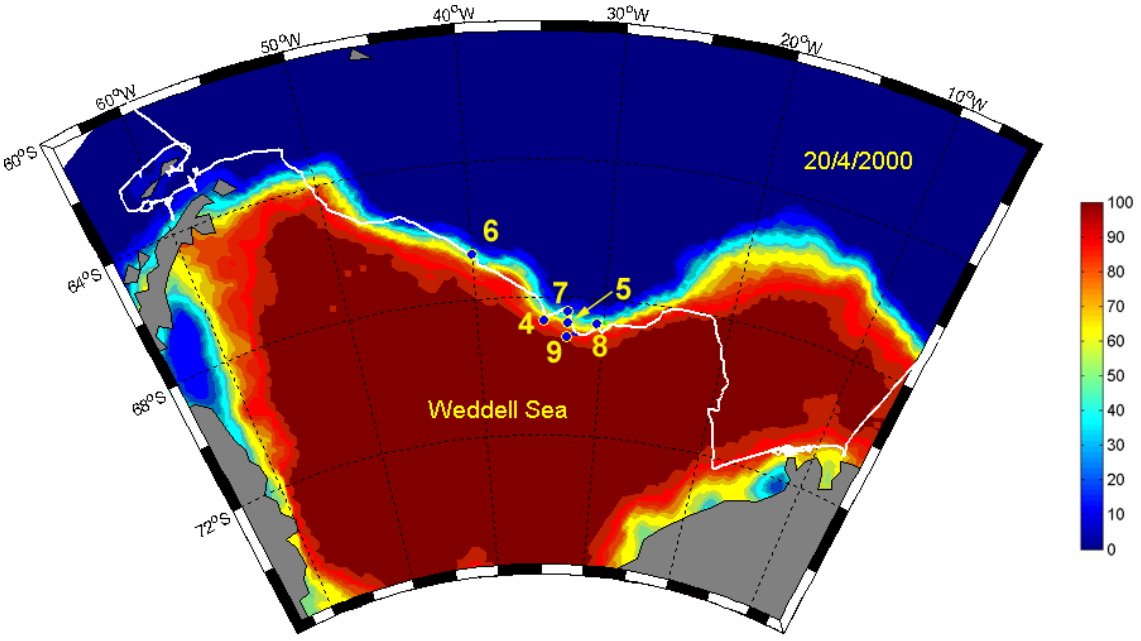

Figure 1.6: Buoy deployments (blue dots) at the ice edge of the Weddell Sea, shown superimposed on SSM/I ice concentration (colour scale in percent) for 20 April 2000. Low concentration areas in the far west and southeast are the algorithm's response to glacial ice shelves, not indicated by the grey land mask. The ship track is shown in white. The numbers indicate the buoy IDs referred to in the text.

The buoys proved to be very robust, with all six units surviving the critical pancake consolidation phase. The resulting dataset is unique, since no-one had previously placed buoys so close to the advancing ice edge and watched consolidation proceed.

Further data are provided by the European Centre for Medium-range Weather Forecasting (ECMWF), in the form of six-hourly analyses of meteorological parameters obtained *via* the British Atmospheric Data Centre (BADC). The author also took part in the collaborative European INTERICE project at the Hamburg large-scale ice tank facility (Thomas and Wilkinson 2001), which provided verification of processes inferred from the Weddell field experiment.

1.3 Scientific Aims

This thesis aims to produce a better understanding and parameterisation of the pancake ice cover in terms of ocean-ice-atmosphere heat fluxes, momentum transfer and ice growth. Pancake ice is a difficult medium to study given its small size and rapidly changing aggregations, and the dynamic environment essential for its formation and survival. Much therefore remains to be done in understanding its formation and response to wind and wave forcing. We cannot hope to portray the overall ice cover accurately without knowing the evolution of ocean-atmosphere heat flux, ice formation (and concomitant salt injection to the upper ocean), drift and deformation across this vast area of the Antarctic. Specific questions which the thesis seeks to answer are:

- What are the characteristics of the unconsolidated ice motion (both absolute and relative) at time scales which are newly-resolvable by these GPS data (20 minute intervals), but not seen in Argos positions (three hour intervals)? How do the air-ice momentum transfer coefficients change as the ice consolidates and ages? What are representative values of wind factor and turning angle for Antarctic pancake ice?
- What is the rate of ice production during pancake formation? How does it compare to the two limiting cases of congelation ice growth (slowest) and frazil ice production at a free surface (fastest)? What are the processes involved in building a pancake from the surrounding frazil slush?
- What are the implications of any differential motion (convergence/divergence cycles) for ocean-atmosphere heat flux and hence ice production within the ice cover? Do current models accurately represent these values?

1.4 Thesis structure

The study consists of three data chapters, preceded by an introductory chapter and followed by a discussion chapter which brings the results together into a coherent whole. The output of one chapter is used in the next, moving towards a better parameterisation of the young ice cover in terms of ocean-ice-atmosphere heat and momentum fluxes. The data chapters of the thesis are:

Chapter Two (Dynamics) presents a detailed analysis of the drifting buoy data, with particular emphasis on the additional information provided by the high resolution (temporal and spatial) of the buoy locations. The onset of consolidation (when pancakes freeze together to form a continuous pack) is established and the dynamical contrast between the two regimes examined, particularly with respect to the momentum transfer and differential kinematic parameters (DKPs). The analysis is used as input to later chapters.

Chapter Three (Thermodynamics) describes a new mechanism for the growth of pancake ice and uses modelling to support the hypothesis. In doing so, an attempt is made to quantitatively describe the growth rate of pancakes by both 'classical' and novel mechanisms, in an advance to the oft-stated but never qualified "*fast*". The air-ice momentum transfer parameters calculated in the previous chapter are used to drive the kinematic portion of a thermodynamic-kinematic model, which tracks the movement of the ice back from the observation time to its formation and extracts the appropriate forcing from ECMWF and *in situ* meteorological data as it goes. The thermodynamic model then uses this forcing to grow ice forwards in time, using both congelation and free-surface frazil parameterisations. The observed pancake thicknesses (corrected for area and volume concentration) are then compared to these two limiting cases to derive a comparative rate for ice production.

Chapter Four (Growth and motion) combines the growth model and rates, developed in the Chapter 3, with the DKPs developed in Chapter 2 to examine the implications of differential motion for ice production. The divergence-convergence cycles undergone by an ice cover are often termed the "ice accordion" since the motion enhances ice production by exposing open water during the divergent events (allowing rapid ice growth) and redistributing ice (building ice thickness) during convergence. We postulate that any motion at the short time scales measured by the buoys has a significant impact on the magnitude of the ocean-atmosphere heat flux within the ice cover and the volume of ice produced as a result. To elucidate this effect, the thermodynamic growth model is combined with a model for the redistribution of ice thickness by deformation (rafting and ridging), driven by the previously-calculated

DKPs. Ice is grown applying the growth rate *versus* thickness relations determined in the previous chapter. The combined model is driven with both the 20-minute forcing measured by the buoys, and with a low-pass filtered timeseries more representative of previous, Argos-based, instruments.

A final chapter then discusses the results and conclusions of the thesis, and suggests further work to deal with the remaining questions.

CHAPTER 2: DYNAMICS

The aim of this chapter is to determine the particular dynamic characteristics of pancake ice, contrast them with the more familiar pack-ice and examine whether high-frequency motion plays a significant role.

2.1 Introduction

The main innovation of the Weddell Sea buoys was to measure accurate GPS positions at relatively short time intervals. The unconstrained nature of the pancake ice suggested that motions at higher frequencies than traditional Argos measurements could resolve may be significant and that short time-scale alternations of convergence and divergence might have important implications for overall ice production rates through exposure of new sea surface. Studies by Leppäranta and Hibler (1987), for instance, suggested that more than 25% of the energy of the strain rate invariants in sea ice may occur at periods between 30 minutes and three hours. Though the 1983 Marginal Ice Zone Experiment (MIZEX '83) measured the positions of ice floes at three-minute intervals (using radar transponders), such high-frequency measurements have never been performed in the highly mobile pancake zone, to the author's knowledge.

The GPS positions, apart from being more frequent, are also considerably more accurate, allowing an improved representation of the buoys' (hence the ice's) drift. The location qualities of the two systems are demonstrated by Figure 2.1, which compares a section of drift track: GPS locations clearly show loops and meanders in the track, which are masked by the poor quality of the Argos fixes.

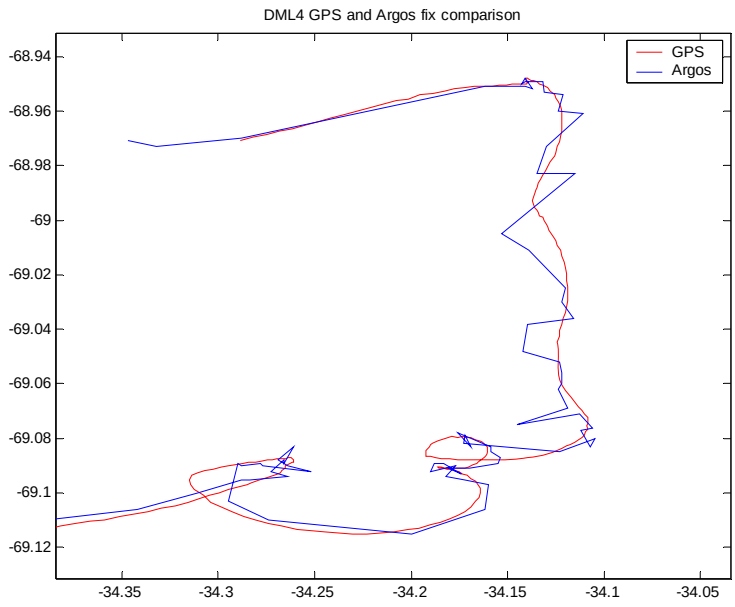

Figure 2.1: A section of drift track, showing the greatly increased quality of locations afforded by the 20-minute interval GPS locations (red), over the more traditional Argos system (blue).

The buoys were originally deployed at a slight embayment in the ice edge - as seen in Figure 1.6 - and it was expected that the boundary between pancake and pack ice (the consolidation boundary) would advance smoothly through the buoy array as the season progressed. In fact, the ice advanced northwards on either side of the array while remaining essentially stationary at the buoys' longitude, leaving the buoys in a deep embayment. This bay then froze rapidly, with the 60% ice concentration contour advancing more than three degrees of latitude between April 30th and May 4th, leaving the buoys far from open water and the influence of wave action. The progress of the 60% ice concentration contour is shown in Figure 2.2, colour-coded by day-of-year:

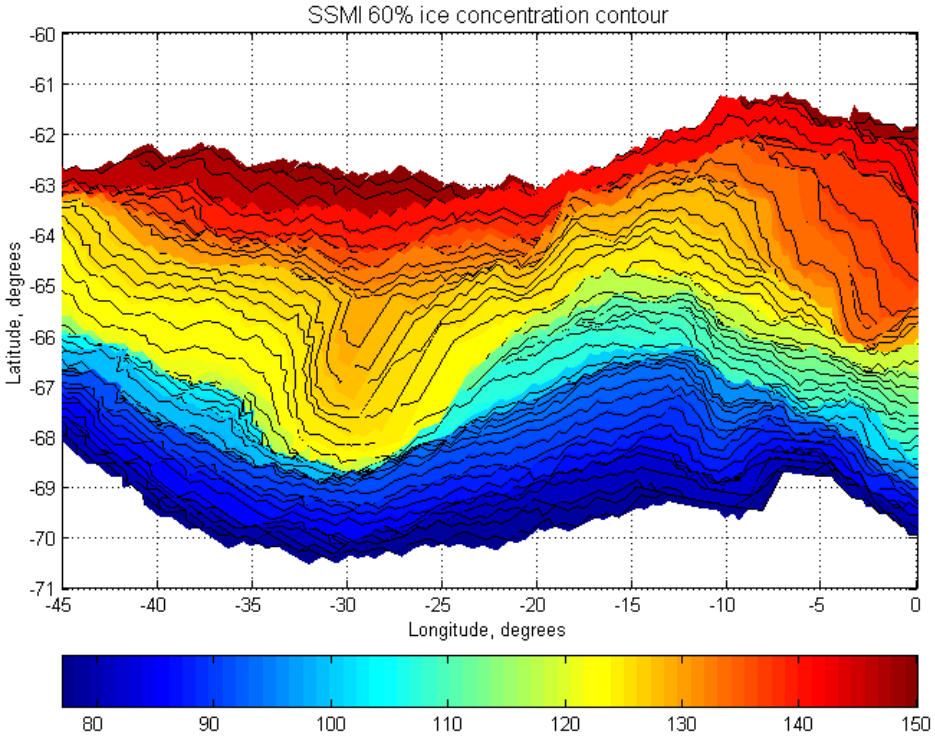

Figure 2.2: Position of the 60% SSM/I-derived ice concentration contour, showing the pinching-out and rapid freezing of the embayment into which the buoys were deployed. Colour scale shows day-of-year. The buoys were deployed between Days 108 and 110.

This extensive freezing was driven by both the removal of the wave field's mechanical constraint and a significant drop in air temperature. Both aspects resulted from a low-pressure system passing over the embayment, with its associated winds switching from

relatively warm (-2°C) on-ice northerlies, to cold (-17°C) off-ice southerlies, with reduced fetch and thus reduced ability to raise a significant wave field.

Though unforeseen, this rapid transition from unconsolidated pancakes to a situation where the buoys are embedded deep within the consolidated pack ice is ideal for comparing the dynamical behaviour across a sharp consolidation boundary, and this is done in the following sections. The timing of consolidation at each buoy site is examined in the next section.

2.2 Detection of consolidation

The most reliable indication of the onset of consolidation is the wave spectra measured by the buoys, since the passage of waves is the physical phenomenon which prevents the freezing together of the pancakes and hence maintains the unconsolidated cover. Figure 2.3 shows the significant waveheight, H_s, and mean period T_1 for three of the buoys, located at the outer, middle and inner pancake zones. Parameters are calculated from spectral moments transmitted by the buoys:

$$H_s = 4.m_0^{1/2} \qquad \text{(Eq. 2.1)}$$

$$T_1 = m_0 / m_1 \qquad \text{(Eq. 2.2)}$$

where m_n is the nth spectral moment, calculated using the relation:

$$m_n = \sum_{i=1}^{N} f_{centre}^{\,n}(i).\Delta f\,.p(i) \qquad \text{(Eq. 2.3)}$$

where $p(i)$ is the power spectral density (PSD) vector, Δf is the frequency interval of the calculated PSD and f_{centre} is the centre frequency of a given interval. Though rather an abstract concept, spectral moments allow the calculation of parameters without requiring the subjective choice of thresholds, as would be necessary for time domain approaches.

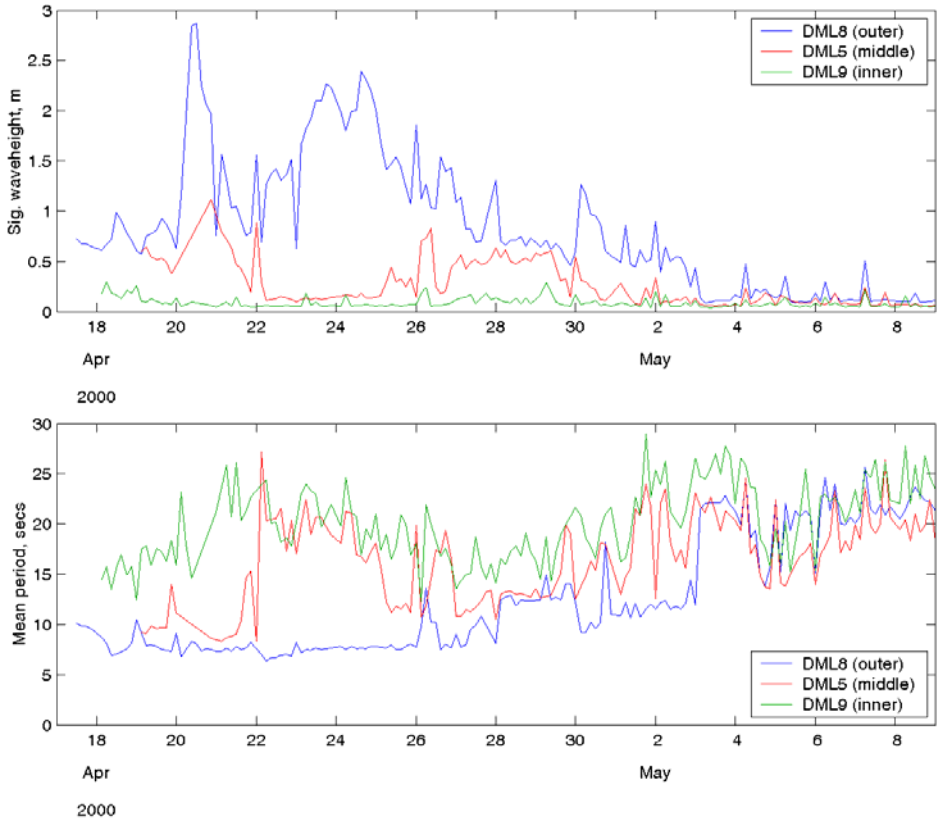

Figure 2.3: Significant waveheight and mean period for three buoys in the array, showing the sharp reduction following consolidation on May 3rd.

Waveheights decreased with distance from the ice edge, with the outer buoys measuring a peak value of around 3 m and inner buoys showing little vertical motion at any time. Wave motion effectively ceased for all buoys by May 3rd 2000. Mean wave periods evolved from low initial values (7 – 8 seconds) at the outer buoys, to a consolidated value of more than 20 seconds by May 3rd. Inner buoys displayed a period close to 20 seconds throughout.

Determination of the exact time of consolidation was made with reference to the full spectra for each buoy, such as that shown in Figure 2.4, and the buoy heading (its orientation with respect to magnetic north), which also showed considerable contrast across the boundary: the axisymmetric buoys were free to rotate in pancakes, but remained fixed once the ice sheet consolidated.

Dates of consolidation, and hence the duration of the pancake phase at each buoy, are shown in Table 2.1.

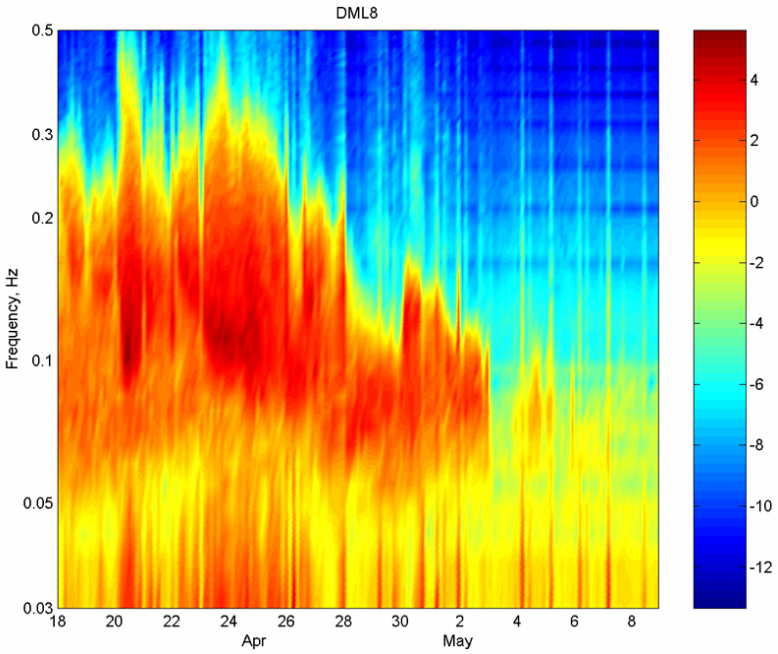

Figure 2.4: The evolution of power spectral density (PSD), displayed here as a contour plot of $\log_{10}$(PSD) in units of m^2s. The sharp drop in power at the consolidation boundary (May 3rd) is clearly shown.

Table 2.1: Buoy deployment details. Columns give the position of the buoy within the ice edge (*i.e.* outer is furthest north), together with the dates of deployment, consolidation (transition from pancake to pack ice) and last transmission over the two satellite systems. All dates refer to the year 2000.

Buoy ID	Argos ID	WMO ID	Position	Deployed	Consol/d	Last Orbcomm	Last Argos
DML4	16187	71583	Inner	19 Apr	20 Apr	15 May	15 May
DML9	19080	71581	Inner	17 Apr	18 Apr	3 Aug	3 Nov
DML5	19075	71511	Centre	18 Apr	29 Apr	13 Oct	24 Oct
DML7	19079	71513	Outer	18 Apr	2 May	30 May	14 Sept
DML8	19076	71512	Outer	17 Apr	3 May	14 Jul	20 Dec
DML6	19081	71582	Long-scale	20 Apr	30 Apr	13 Jul	15 Sept

2.3 GPS issues

Before comparing drift behaviour across the consolidation boundary, it should be noted that the consolidation of the outer buoys on May 2nd and 3rd coincided almost exactly with the ending of intentional degradation of GPS accuracy available to civilian users. This degradation – termed *selective availability*, or SA – was removed at 0430Z on May 2nd 2000. It must be ensured that the dynamical differences in the behaviour of pancake and pack ice, derived from these GPS positions, are free from the effects of the varying positional accuracy between SA and non-SA eras.

To this end, data from a GPS base station installed at the German *Neumayer* station (70°39'S, 8°15'W) prior to the deployments is examined. The base station was installed at the beginning of the cruise to enable differential post-processing correction of the buoy positions and achieve an SA-era position accuracy of around 10 m.

The statistical distribution of position errors before and after the SA transition was examined. The situation is slightly complicated by the fact that *Neumayer* is moving slowly northwards as its ice shelf advances towards the sea. The position error was calculated from both the mean and median position during Week 18 (the consolidation week). Little difference in statistical descriptors was found between the two methods, and the mean was used for further work since this includes all data and is a more statistically valid approach. Identical length data (3082 points) were used before and after the SA transition.

The difference in errors either side of the transition is striking. Position data had a median of 18.0 m and variance 143.9 m during the SA era. In the post-SA era, median and variance were 2.8 m and 5.2 m respectively. Both 'before' and 'after' data fail the Kolmogorov-Smirnov test for normality, but fitted gamma distributions well. No statistically-significant difference (using the Mann-Whitney rank sum test) was found between modelled distributions and the actual data, to a high confidence level (P=0.729 and 0.745 respectively). Modelled and real data are shown in Figure 2.5.

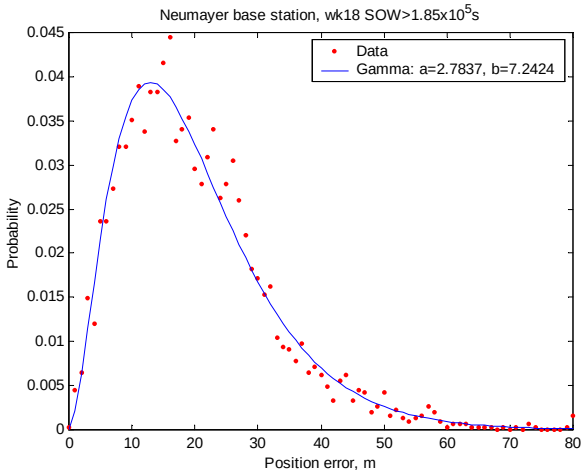

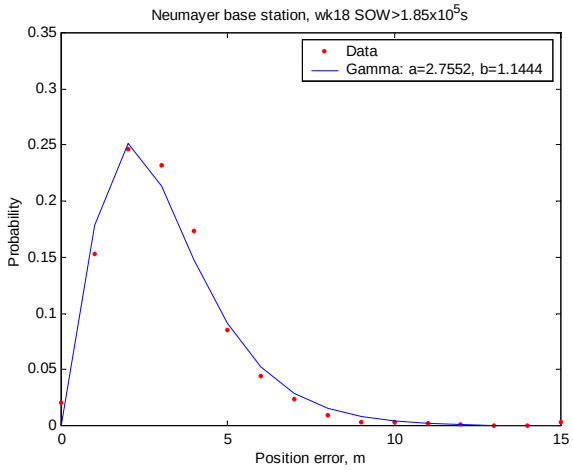

Figure 2.5: Modelled and real data compared for SA (top) and post-SA era (bottom) position errors for the *Neumayer* station DGPS base station. The gamma distributions can be seen to fit the data well.

Velocity errors were examined and also fitted gamma distributions to a high degree (P=0.902 and 0.964). Median error speeds were 0.89 cm s^{-1} and 0.13 cm s^{-1}, with variances of 4.5 cm s^{-1} and 0.03 cm s^{-1} for SA and post-SA eras respectively. These errors are smaller than would be obtained from applying the mean position error for each period, *i.e.* we might expect the velocity errors to be of the order of:

$$u_{err} = v_{err} = \sqrt{2}\,\frac{\overline{x}_{err}}{\Delta t} \qquad \text{(Eq. 2.4)}$$

where u_{err}, v_{err} are the component velocity errors, x_{err} is the mean position error and Δt is the timestep (Geiger *et al.* 1998). This gives expected scalar velocity errors of 3.4 cm s^{-1} and 0.5 cm s^{-1} for SA and post-SA eras respectively, whereas we achieve

approximately one third of these figures. The magnitude of these speed errors (*c.f.* an RMS drift speed around 25 cm s^{-1}) shows the value of GPS fixes over Argos positions: Argos velocity errors are typically around 5 cm s^{-1}, with a three hour fix interval (Geiger *et al.* 1998).

Modelled errors were used to degrade the post-SA buoy positions, to achieve the same error distribution as the SA-era fixes and ensure that any dynamical differences are due to physical, rather than instrumental, changes. A series of random numbers fitting the SA model were generated and imposed at a random angle on the post-SA positions. The resulting distribution is similar to the SA-era data (P=0.790 from Mann-Whitney). All further analysis was performed on this "error normalised" position data.

An additional complication arises, since the buoys experienced differing rates of GPS position loss (drop-out) during their lifetimes. A GPS almanac bug in the buoy control code resulted in an increasing rate of drop-outs after the initial deployment. Remotely rebooting the units over the two-way *Orbcomm* satellite link cured the problem, but marked differences remain between buoys and with time. Daily valid fix proportions (of the required 72 per day) are shown in Figure 2.6, which displays the steady decline during the first 25 days of deployment.

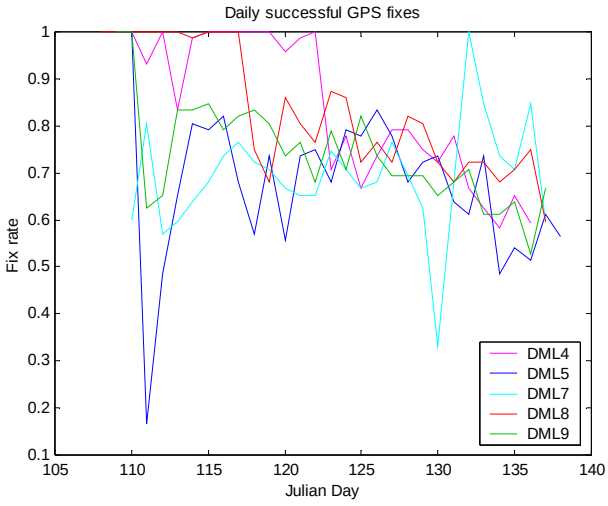

Figure 2.6: The proportion of daily valid fixes achieved by each buoy in the array, prior to being remotely-rebooted to cure the problem.

These missing fixes tend to reduce the high-frequency power present in a buoy's drift record, reinforcing the expected decline in HF power caused by increasing rectification of the ice movement as the pack consolidates. The effect will be minimised for DML7 and DML9, however, since these retain a similar fix rate throughout the period of interest. Missing fixes were interpolated to the standard 20-minute interval using a cubic spline technique. The interpolation is demonstrated in Figure 2.7, which shows a large gap in DML5's record (this buoy had the most numerous drop-outs)

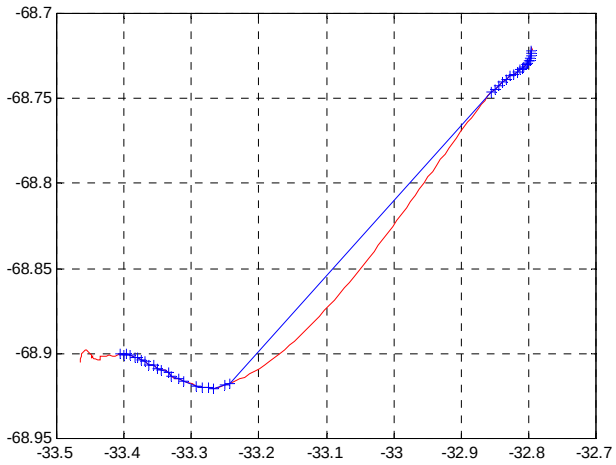

Figure 2.7: Cubic spline interpolation of DML5's drift track. Actual position fixes are indicated by crosses, with the cubic spline interpolated portion of the track shown in red. The spline follows the curvature of the track at either end of the gap, filling it in a more realistic manner than simple linear interpolation (straight blue line).

Drift analysis

Analysis of the buoy drift data is split into three sections:

- Drift of the individual buoys
- Transfer functions between buoy drift and wind forcing
- Relative motion of the buoys in the array

Each is considered first in the time domain, then in the frequency domain. Since the drift parameters were expected to vary as the ice cover evolved, calculations were generally done using a running window, set to 10 days duration, moving forwards at one-day intervals. The window length was chosen to be similar to the duration of the pancake phase of the outer buoys, while providing sufficient samples within the window to allow robust calculations.

2.4 Drift velocities

2.4.1 Time Domain

The buoys had initial scalar drift speeds of between 22 and 35 cm s^{-1}. The scalar speed of each buoy was largely determined by its *v*-component (north-south, approximately perpendicular to the ice edge). The drift speed of all buoys fell gradually during the deployment, reaching a minimum of 18 cm s^{-1} by August (mid-winter) shown in Figure 2.8. The trend was not reflected in the 10-day average winds (ECMWF, 10 m level), which remained around 4 m s^{-1} throughout.

During the initial period, the outer buoys had significantly higher drift speeds (29 – 35 cm s^{-1}) than the inner buoys (23 cm s^{-1}), with the central buoy having an intermediate response (29 cm s^{-1}). The disparity was not reflected in the local wind forcing, as measured by the buoys' anemometers. The behaviour was a robust character of the motion, since very similar trends were observed with varying lengths of the running window. Scalar variance – defined as the root-sum-square of the component velocity variances (Kottmeier *et al.* 1997) – was low, at around 2 cm s^{-1}. Drift speeds for all remaining buoys became very similar past Day 160 once the array was embedded in the pack ice far from the open ocean. Drift speeds continued to fall past Day 180, mostly explained by the reduction in wind speed experienced by the array, before picking up once more as the only surviving buoy began to be influenced by the increasing wind speeds above the Antarctic Circumpolar Current (ACC) at the northern limit of the pack ice.

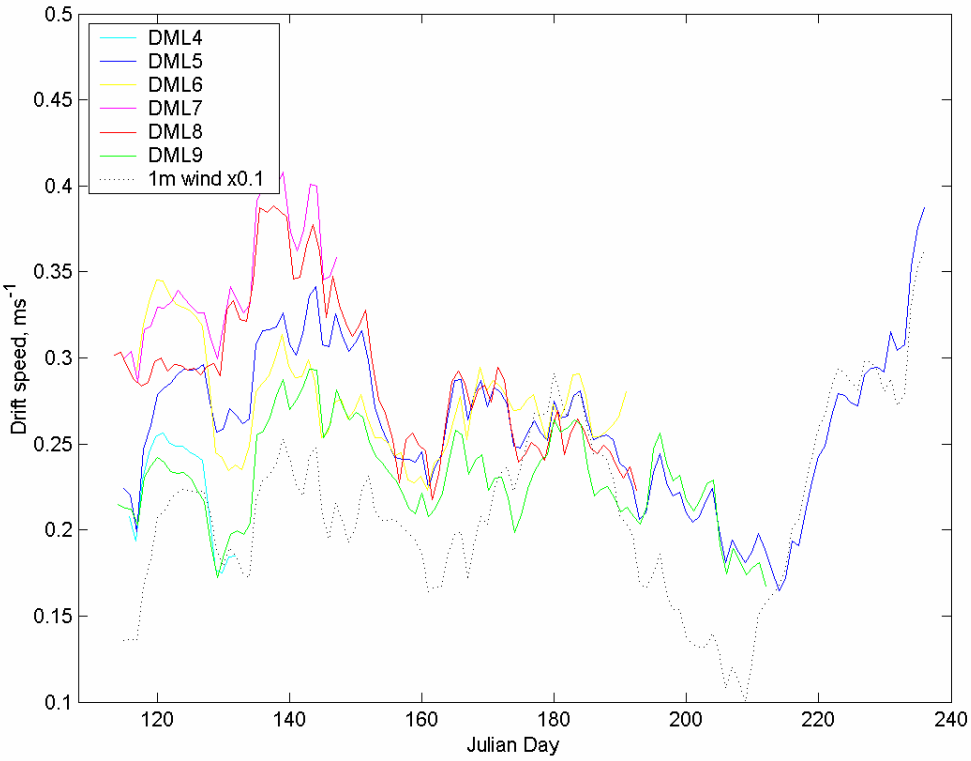

Figure 2.8: Scalar RMS drift speeds for all buoys, for the entire duration of their deployments, calculated with a running 10 day window advancing in one day steps. Also plotted is the scalar wind speed measured by the central buoy (DML5), scaled by 0.1 to plot on the same axes.

2.4.2 Frequency domain

The relatively low number of samples during the unconsolidated phase (less than 1118) makes producing a useful power spectral density something of a challenge. The following methods were compared:

- Simple periodogram, 1024-point FFT (zero padded when shorter) with various windows applied. The Kaiser window, with β set to 7 to ensure the window drops to zero at record ends, provided the best compromise between spectral resolution and variance
- Welch averaged/overlapped segments, using (a) 2x512-point segments, (b) 4x256-point segments, overlapped by 50% of their width and windowed with boxcar, Hamming, Kaiser and Parzen windows. This is a similar method to that

used in the on-board wave spectrum algorithm of the buoys themselves, as it gives the smallest possible variance per data point

- Thompson's multi-taper method, with various time-bandwidth parameters. This gave inferior results in the high-frequency part of the spectrum

The two-segment, overlapped Welch method with Hamming window gave the best results and this was used in all further FFTs. Example *v*-component spectra for DML7 (outer MIZ) and DML4 (inner MIZ) are shown in Figure 2.9, together with those for the *in situ* (1 m ASL) windspeed measured at DML7. Spectra are plotted for the pre-consolidation period of DML7 and for an equivalent period (11 days) post-consolidation.

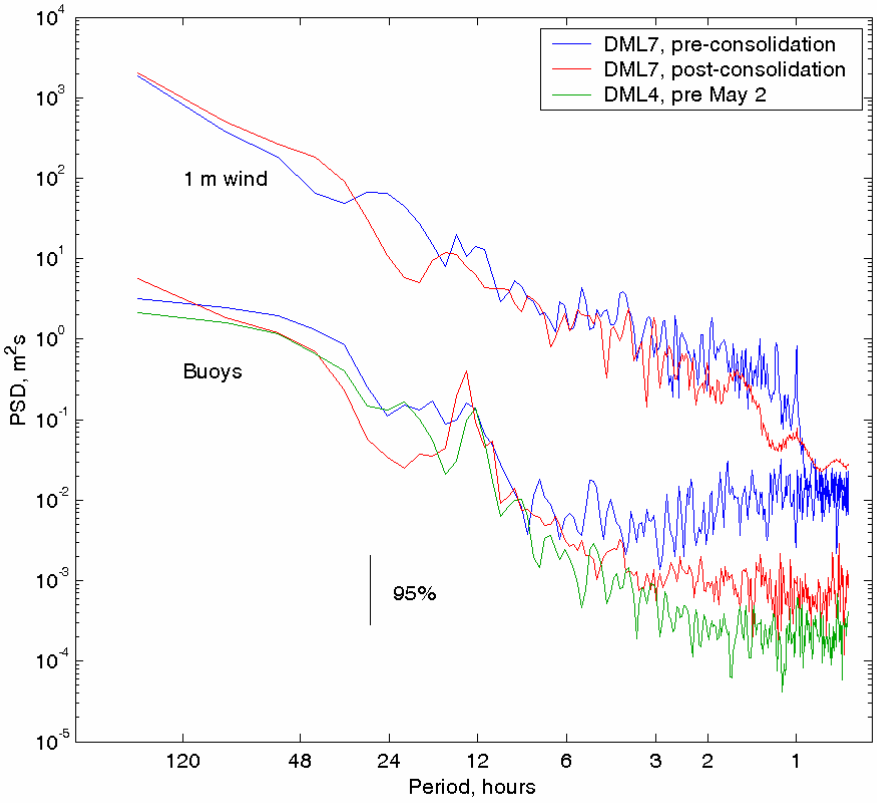

Figure 2.9: *v*-component drift spectra for outer (DML7) and inner (DML4) ice edge buoys. Only one spectrum is plotted for the inner buoy, since the post-May 2nd spectrum is very similar to that shown and is therefore omitted for clarity. Also shown are spectra for the scalar *in situ* windspeed measured at DML7.

All spectra show increasing spectral power towards the low-frequency end of the spectrum. This 'red noise' behaviour is characteristic of many geophysical parameters and persists here when the mean (DC component) of the drift is removed, as done here.

Considerable contrast is evident between pre- and post-consolidation spectra for the outer buoy, with higher power at all frequencies and an order of magnitude increase at high frequencies during the pancake phase. The increased contribution of motion at timescales shorter than six hours is clearly shown by the elevated power in DML7's pre-consolidation spectrum. This energy is not present post-consolidation. The scalar *in situ* wind spectra show no such contrast. The inner buoy displays little change in its spectra between the two periods, and the post-May-2nd spectrum is omitted for clarity. Power in both phases is similar to that shown by DML7's post-consolidation spectrum.

The significant peak in the buoys' post-consolidation drift at around 12 hours was investigated using rotary spectra (Emery and Thomson 1998) to determine whether its origin was tidal or inertial: inertial motions only appear in the counter-clockwise (CCW) component for the Southern Hemisphere, while tidal cycles appear in both clockwise (CW) and CCW spectra. Figure 2.10 shows the peak in the CCW spectrum only, indicating the inertial nature of the oscillation. The inertial influence is expected, since the array was deployed in an area of very little tidal influence (Padman and Kottmeier 2000). Also marked on Figure 2.10 is the inertial period at the buoy's latitude, given by:

$$T = \pi / \omega \sin \phi = 12.85 \text{ hours} \qquad \text{(Eq. 2.5)}$$

Where ϕ is the latitude and ω is the angular velocity of the Earth, 7.272×10^{-5} rads s^{-1}. The dominance of the inertial peak suggests that the pack ice is essentially in free-drift behaviour throughout, since relatively compact ice fields tend to damp inertial motion due to phase mismatches between nearby interacting inertial cycles (McPhee 1980).

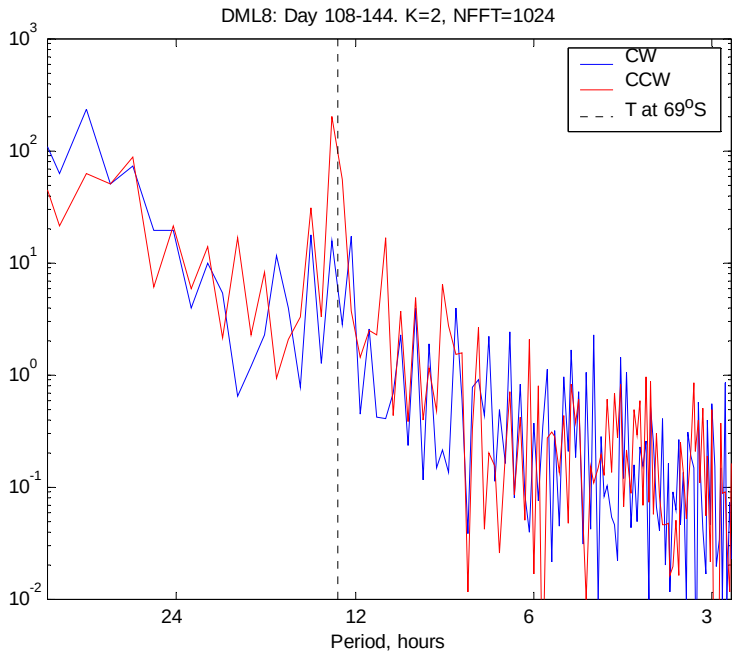

Figure 2.10: Rotary spectra for DML8, showing the inertial peak in the CCW spectrum only. The inertial period of 12.85 hours is indicated by the dotted line. (Matlab code for rotary spectra courtesy of Timo Vihma, FIMR).

The effect of missing fixes on the HF spectra, mentioned in the previous section, was investigated by imposing an artificial drop-out rate on otherwise complete data. Even inflicting the maximum loss rate seen (32%) had very little effect on the resulting spectrum, and any differences in this portion of the spectrum result from physical differences alone.

The time evolution of the spectra was examined with reference to the spectral slope (α). Slope was calculated from the spectrum between 3-hour and 12-hour periods, corresponding to the largely linear (in log-log space) portion of the spectrum. Spectral slope is defined as:

$$S = \omega^{-\alpha} \qquad \text{(Eq. 2.6)}$$

where S is power spectral density and ω is the angular frequency. Results are displayed in Figure 2.11, for the *u*-component of motion; *v*-component results are similar.

Spectral slopes for the various buoys largely overlay, showing a trend towards increasing values – *i.e.* a reduction in HF motion – until Day 190 (mid July), with a similar gradient decrease (increase in HF motion) thereafter. The decrease after Day 190 suggests that the pack ice is becoming less constrained after this date, consistent with its generally divergent nature towards the maximum ice extent. Values are lower during the pancake phase than generally seen in the literature (e.g. 3, Leppäranta 2005), consistent with the increased influence of HF motion. They compare with typical values of 5/3 for oceanic velocity spectra at centimetric scales and 2 at eddy scales. The slope for the outer buoys therefore suggests that the ice cover is responding to the oceanic velocities almost without modification (value close to 2).

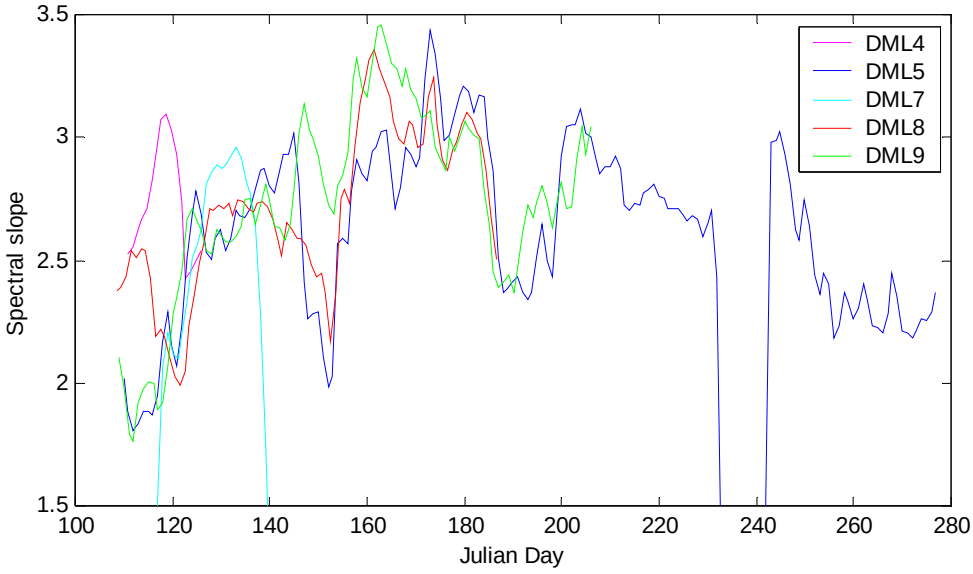

Figure 2.11: Spectral slope with time for the full duration of the buoy deployments.

Variations in integrated power at high- and low-frequencies over time were also studied, since changes in the spectral slope give no information on the magnitude of power at any frequency, only its variation over the chosen spectrum. The division between LF and HF regimes was set at 15 hours period, to include the inertial component, and was also investigated at 4 hours cutoff. Results are shown in Figure 2.12 for a 15 hour

cutoff. Both cutoff values showed a similar trend, with HF power dropping exponentially (linearly on a log scale) until Day 200 and then increasing thereafter. Characteristics for all buoys again largely overlay, mirroring the character of the α curve. The HF power and α, which both depend on the freedom of movement, correlate at $-0.65 < r < -0.88$. Power at LF shows a contrasting character, oscillating around a more constant value.

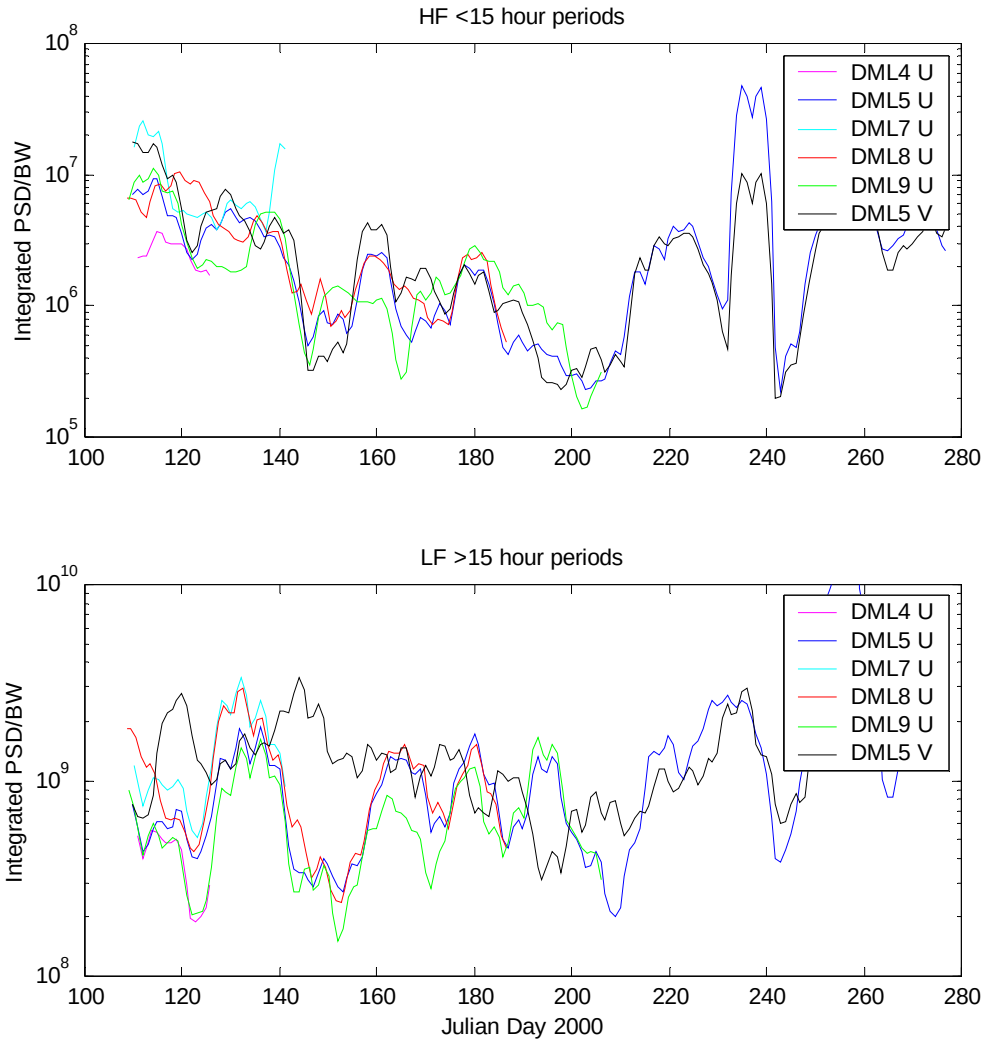

Figure 2.12: Integrated power spectral density per bandwidth, for HF (top) and LF (bottom) periods. HF power shows a cyclical character as constraint is increased then relaxed, while LF power is more constant throughout.

The analysis shows that the increase in spectral slope seen previously arises from a very marked reduction in the HF power, which drops by two orders of magnitude between the pancake era and the point of 'maximum constraint' (Day 200), while the lower frequency power has a more constant character, oscillating around a mean value and represents the overall advection in the Weddell Gyre. Since the scalar drift speed (Figure 2.8) mirrors the form of the HF curve, it can be concluded that this high-frequency energy contributes significantly to the overall motion of the buoys during their initial deployments.

All parameters suggest a cycle of constraint: As the ice edge advances past the buoys, constraint increases to a maximum in mid-August (Day 200), after which the increasingly divergent nature of the pack ice reduces constraint once more, before the ice finally breaks up at its northern limit in December. The pancake regime does not appear radically different from the pack ice in this aspect of the study, and can be considered a starting point in the cyclical evolution of constraint from the ice's formation to its break-up.

2.4.3 Wavelet Analysis

The ten-day running window used in the preceding analysis necessarily averages the parameter under study over the window period. It is perhaps interesting to examine whether the unconstrained high-frequency motion is a continuous feature of the pancakes' motion, or whether it is more periodic, varying as low pressure systems pass the array. Reducing the FFT window length often gives rather arbitrary results, however, as the number of points in the FFT drops to below tractable values. Frequencies are also treated inconsistently in such an analysis, since low frequencies are only represented by a limited number of cycles in each window (reducing frequency localisation - the routine's ability to discriminate the frequency of a component) while high frequencies have so many cycles in the window that it is difficult to determine where the component begins and ends (time localisation).

Wavelet analysis offers a possible solution to the problem, though it has been criticised for providing 'pretty pictures' but little quantitative information, especially with regard

to statistical significance. Wavelet routines with significance and confidence testing have been developed (Torrence and Compo 1998), however, and these are used here in an attempt to overcome such objections. Details of the wavelet analysis are given in Appendix A.

Wavelet spectra are shown for the central buoy (DML5, Figure 2.13) for the initial period of interest (to Day 142). The *v*-component velocity is chosen since it shows the greatest contrast between pancake and pack ice regimes, though the *u*-component results are similar. The figure demonstrates the additional insight that wavelet analysis can provide: Though the high frequency energy is clearly evident throughout the first half of the timeseries (top graph), it shows considerable power variation in the wavelet spectrum (middle graph), alternating between periods of high energy (yellow) in the 1-6 hour band and even higher energy episodes when the orange colour intrudes into the same band. The periodicity in this variation is of the order of five days, which is approximately the time taken for an atmospheric low-pressure system to pass the array, from the initial, compacting, northerly winds to the final, rarefying, southerlies. Such a conclusion suggests that the highest frequency energy is forced by the wind, but this is not supported by analysis of the *in situ* wind records themselves, which show no such variation in HF power. The wavelet analysis therefore gives the insight to suggest that variations in the buoys' HF motion are caused indirectly by the winds – for instance by the wind direction determining the state of compression of the pancake zone, and hence its ability to respond to other, possibly oceanic, forcing.

DML5's inertial energy appears non-significant (bottom graph) and the inner buoys display even less power in this band, suggesting that these latter buoys undergo more damped motion from the start of their records. Intermittent oscillations are seen in the outer buoy's plots.

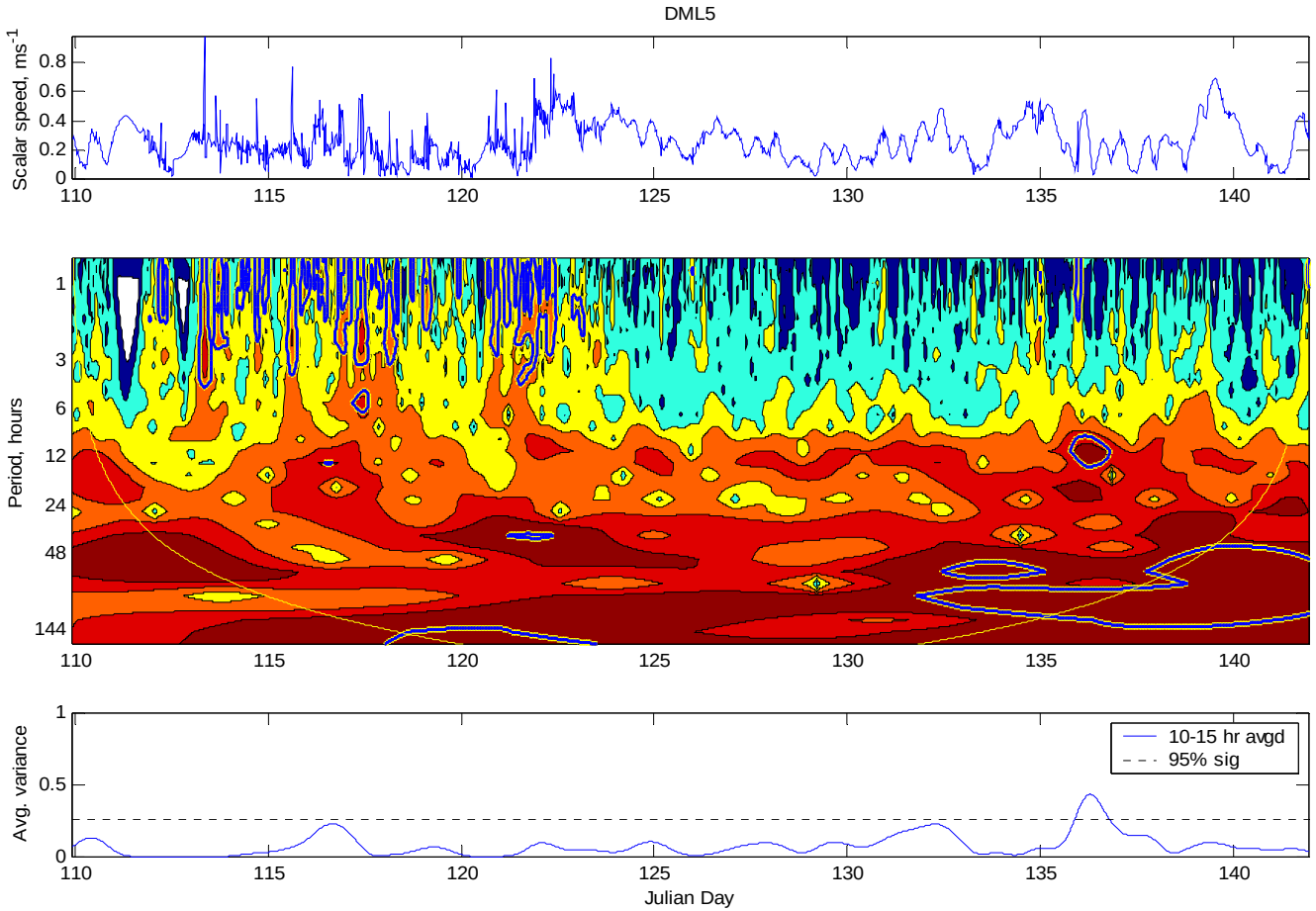

Figure 2.13: Wavelet power spectrum for the central buoy (DML5) around the consolidation boundary. Top graph shows the scalar velocity timeseries. Middle graph shows the wavelet power spectrum, with the cone of influence marked as a yellow line and the 95% confidence contour marked as a thick blue line overlaying a thicker yellow contour. The bottom graph shows the integrated wavelet power across 10-15 hour scales, and is a measure of the total power in the inertial 12 hour peak. The dotted line corresponds to the 95% significance level.

2.5 Momentum transfer coefficients

The preceding analysis demonstrated progressively decreasing scalar drift speeds in the presence of relatively constant wind forcing. These results imply either that the ability of the wind to transfer its momentum to the ice is changing – due, for instance to the ice roughness changing as the ice evolves – or that the influence of other forcing, not related directly to the local wind speed (such as the large-scale wind curl which drives the Weddell Gyre), is varying. The transfer of energy from the atmosphere to the ice and hence to the ocean is important for the modelling community. Parameters must be known accurately in order to model the drift of the ice. The track and hence residence time of a particular piece of ice in the pack determines its rate of formation, thickening (thermodynamically and by deformation) and subsequent melt. Such information allows estimation of heat, salt and momentum fluxes throughout the polar oceans and is crucial to understanding the physical processes operating there. Accordingly, these momentum transfer parameters are investigated in some detail in this section, since values for Antarctic pancake ice are currently entirely unconstrained.

Momentum transfer from surface winds to buoys or ice can be described by a simple linear ratio, known as the wind factor, α, with turning angle, δ, between the wind and the forced object (CCW in the Southern hemisphere). Linear ratios have been shown to approximate the non-linear momentum balance well (McPhee 1980; Thorndike and Colony 1982; Martinson and Wamser 1990; Kottmeier *et al.* 1992), especially for thin Antarctic ice where the Coriolis term is relatively small. Alternative methods, such as the solution of quadratic drag coefficients, involve assumptions about the roughness lengths of air and water interfaces which are unknown (Thomas 1999).

Wind factor and turning angle were calculated using both the winds measured by the buoys (1 m ASL) and ECMWF 10 m winds, both interpolated to the 20 minute fix interval using a cubic spline. Points with a wind speed value of less than 1 m s^{-1} were removed, to eliminate sensor freeze-up events (actually quite rare) and light-and-variable conditions. Turning angle was calculated after removing outlying points, which were defined as being those exceeding an absolute angle of more than 120°.

In situ wind directions were unfortunately not available from DML6, DML7 and DML8, due to faults in their compasses. Though the headings of other buoys varied through the full 360° during the unconsolidated phase, headings for these three buoys varied through very limited angles (*e.g.* 280° to 360° for DML7). This is unlikely and points to a fault in these compass units (Honeywell HMR3000) or in their calibrations. It was not possible to perform an in-hull calibration of the compass units, as the buoys were constructed on board the ship in the presence of many hard- and soft-iron influences, but these results indicate that this is essential if reliable directions are to be obtained from future deployments.

The wind direction is calculated (post-transmission) as a combination of the wind sensor direction with respect to an on-board reference and the buoy magnetic heading. Magnetic deviation in the area of the buoys is almost exactly zero, and is ignored. The wind direction information for these three buoys must therefore be completely disregarded, which is unfortunate, since these are the buoys which remained in pancake ice the longest.

ECMWF 10 m winds are generated from pressure analyses at the lowest model level (30 m), estimating the surface roughness length and atmospheric stability (Kottmeier *et al.* 1997). These 10 m results were then interpolated from the ECMWF 1.125°×1.125° grid to a 0.5°×0.5° grid, using the Kriging technique.

2.5.1 Buoy and model winds compared

The correspondence between modelled (10 m) winds and measured (1 m) winds was examined in terms of their correlation, velocity ratios and turning angles, for scalar speeds and vector components. Results are shown in Table 2.2. Values for the magnitude relation are very consistent and have low standard deviations, though the turning angles have a greater spread.

Table 2.2: Magnitude ratio and angle (degrees) between buoy-mounted wind measurements (1 m ASL) and ECMWF 10 m model output, for the whole lifetime of each buoy, expressed as the median and standard deviation (SD). Directions are omitted for buoys with faulty compasses. Calculations for DML5 do not include the period of open water drift at the end of its deployment.

DML	**Median v_1/v_{10}**	**SD v_1/v_{10}**	**Median Angle**	**SD Angle**
4	0.60	0.24	73	34
5	0.56	0.29	53	53
6	0.56	0.26		
7	0.57	0.85		
8	0.60	0.37		
9	0.59	0.31	50	28
Mean	**0.58**		**59**	

The published literature contains few references to winds at this low height, which was dictated by stability requirements in the heavy icing conditions that the buoys were expected to experience. Rare measurements come from ice camps in mature pack ice such as the 0.6 m measurements at Ice Station Weddell (Andreas and Claffey 1995), for which the $V_{0.6}$:V_{10} ratio was ~0.25. A minimum height of 4 m is more usual, with quoted transfer coefficients over winter pack ice of 0.53 to 0.55 (with respect to the geostrophic wind), with a turning angle of 7-30^o (Vihma *et al.* 1996; Uotila *et al.* 2000).

Buoy winds were then rotated by the mean angle calculated above and correlation between buoy and model winds examined, for vector and scalar components. Results are shown in Table 2.3. Coefficients are high for all valid components and scalar speeds. They are similar to those seen in published literature (*e.g.* Uotila *et al*. 2000) though sensor heights were typically 4 m there, and give some confidence in the

ECMWF results. It should be noted that the buoys were transmitting pressure data to the Global Telecommunications System (GTS) throughout their lives, giving the model unusually well-constrained surface pressure fields for the region. They are not, therefore, independent functions and we would expect results for the Weddell Sea to be significantly worse in the absence of this mesoscale array.

Table 2.3: Correlation components (r_S^2) between ECMWF 10 m winds and the buoy 1 m winds rotated by the mean angle of 59°. Component correlations cannot be calculated for buoys with faulty compasses.

DML	*u*-component	*v*-component	Scalar
4	0.84	0.92	0.80
5	0.84	0.86	0.73
6			0.77
7			0.70
8			0.71
9	0.90	0.92	0.76

ECMWF winds might be expected to be less accurate while the array is close to the ice edge, since local effects of the ice-ocean boundary are not explicitly accounted for by that model. While the lack of outer-buoy wind directions hampers this comparison, the change in correlation between model and *in situ* wind speeds can be examined. This was done, splitting the record at Day 125 (when the outer buoys consolidated) and comparing correlation coefficients for the two (similar length) periods until DML4 stopped transmitting on Day 136. Table 2.4 gives the coefficients, and a plot of model and *in situ* winds for outer and inner arrays is shown in Figure 2.14.

Table 2.4: Correlation coefficients between *in situ* and 10 m model winds for the early buoy lifetimes, contrasting the success of the model winds at the outer and inner ice edge. *In situ* winds are low-pass filtered with a 6 hour cutoff to match the sampling interval of the model winds.

	Buoy ID	**<Day 125**	**Day 125-136**
Inner ice edge	**DML4**	0.77	0.83
	DML9	0.66	0.76
Outer ice edge	**DML7**	0.63	0.89
	DML8	0.52	0.82

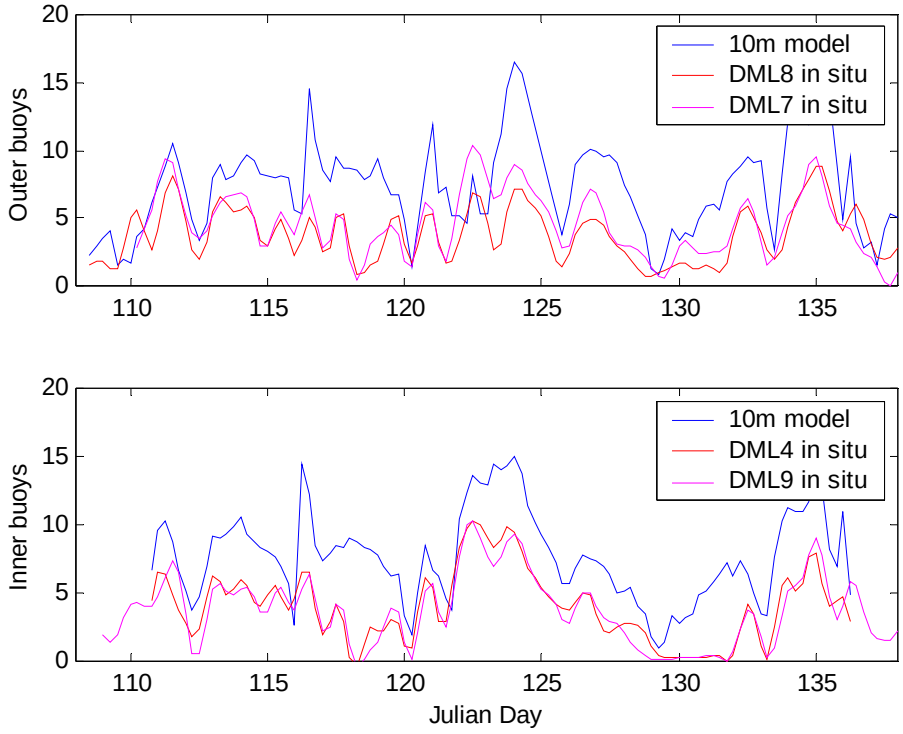

Figure 2.14: Timeseries of outer (top) and inner (bottom) ice edge windspeeds (m s^{-1}), illustrating the inferior performance of the model during the initial consolidation phase, for both outer and inner arrays. *In situ* winds are 6 hour low-pass filtered. Only one model wind speed per graph is shown, as these are very similar for the two similarly-positioned buoys.

Correlation coefficients are notably lower during the early phase of the buoy deployments, as expected from the previous analysis and discussion. Correlations are lower for the outermost buoys than for those further towards the consolidated pack ice, reflecting the poor performance of the ECMWF results in the outer zone and the influence of effects there which are largely unparameterised in that model. The finding renders the failure of the onboard compasses of the outermost buoys more unfortunate, reliable wind directions – and therefore components – are therefore lacking for the period of greatest interest.

2.5.2 Buoy transfer functions

The foregoing analysis established that both the buoy and model measurements of wind forcing are essentially reliable and self-consistent, excepting the directions from the outer buoys. We now move on to apply these fields to determine transfer coefficients for the various ice conditions encountered.

In order to isolate wind stress effects it is necessary to remove non-wind-based motions – such as inertial loops - from the timeseries. This would suggest a LP filter excluding periods of less than, say, 14 hours. The *in situ* wind record clearly shows strong variability at periods much shorter than this, however. We therefore compared results using the 14 hour filter with those using a cutoff designed to exclude only transient timescales of the ocean boundary layer (OBL). For thin Antarctic ice, steady state is achieved within an hour of any change in external forcing (Martinson and Wamser 1990) and a two-hour LPF is chosen here. Tests demonstrated that the effect on mean drift rates for this filter period is negligible.

Wind factor and turning angle were calculated using three methods:

- Linear regression
- Two/four-parameter matrix solution
- Constrained regression

Simple linear regression has problems, since it gives rise to non-zero intercepts (drift present in the absence of any wind forcing) which constitute residual currents and

integrate the unknown effects of non-wind-based factors, such as wave radiation pressure. The small number of points available during the unconsolidated phase of many buoys represents a challenge to the regression routine and may result in higher residuals – and consequently lower regression gradients – than would otherwise be the case.

The matrix approach finds a least-squares solution to the equation below (Vihma *et al.* 1996):

$$V_i = V_z \times \begin{pmatrix} a_{11} & a_{12} \\ a_{21} & a_{22} \end{pmatrix} + V_{res} \qquad \text{(Eq. 2.7)}$$

where V_i are the component velocities of the ice, V_z are the forcing velocities and V_{res} are the residual velocities. This four-parameter case can be simplified to a two-parameter system, constraining $a_{11} = a_{22} = b_1$ and $a_{12} = -a_{21} = b_2$. The wind factor is then constant, given by the root-sum-square of the coefficients, and the turning angle is $tan^{-1}(b_2/b_1)$. We also calculated the 'degree of explanation':

$$R^2 = 1 - \sigma_\varepsilon^2 \Big/ \sigma_0^2 \qquad \text{(Eq. 2.8)}$$

where σ_ε^2 is the variance of the residual current and σ_0^2 is the variance of the observed ice drift.

Though generally the most reliable approach, the two-parameter method is unable to resolve any parameters for *in situ* winds for the failed compass buoys, since derivation of the wind factor is no longer divorced from the turning angle. We therefore also present results from a third method, which uses fixed residuals applied *a posteriori* to constrain the regression gradient.

Results are shown in Figure 2.15, for one outer (DML8) and one inner (DML9) buoy. The wind factor, turning angle and residuals are plotted for the three schemes, for a ten-day running window across the first two months of deployment.

Simple regression using *in situ* winds for DML8 showed a downward trend in wind factors, from around 5% to 3% by mid June. Residuals were very high (12 cm s^{-1}) pre-consolidation, reducing gradually to 3 cm s^{-1} in two weeks – a value they remained close to from thereon. This value was therefore chosen for the constrained regression scheme. Other buoys had rather haphazard results with simple regression, reflecting the difficulties of the method with scattered data and a low number of samples. Constrained regression using *in situ* winds and 3 cm s^{-1} residuals for DML8 showed a clear reduction from around 6.8% in the pancake phase to 3.8% by mid-June. DML9, in contrast showed no clear trend in its constrained regression result with *in situ* winds, remaining around 4-5% throughout. Constrained regression with 10 m winds and DML8 showed a reduced but similar trend, dropping from 3.5% to 3.0% over the same period, with the inner buoy showing no clear trend and lower values (*c*. 2.6%). Two-parameter results were very similar to constrained regression results for 10 m winds. The two-parameter scheme showed little long-term trend with *in situ* winds for the inner buoy, with values remaining around 3% throughout.

For turning angle, simple and constrained regression gave very similar results for the valid (inner) buoys' *in situ* winds (*c*. –68^{o}). Two-parameter, 10 m, results were similar for all buoys, staying relatively constant between –10^{o} to –20^{o}. Regression schemes gave similar values to the two-parameter method where the simple regression residuals were low. When these residuals rose, however – due to the low windspeed points being removed and significantly reducing the number of samples available to the algorithms - turning angle was significantly reduced (became less negative). Two-parameter residuals tended to follow a similar form to the regression results, but did not perturb the turning angle, which remained relatively constant throughout.

Correlation coefficients for DML8's 10 m constrained regression rose from a minimum of *c*. 0.5 during the pancake phase to a relatively constant 0.85 once consolidation occurred. *In situ* winds fared rather better during the pancake phase, correlating at r_S^2 = 0.7, rising to 0.9 post-consolidation for the constrained regression scheme. Both coefficients for the inner buoy (DML9) remained around 0.85 throughout for *in situ* winds. For DML9's 10 m winds, both coefficients followed that of DML8 closely.

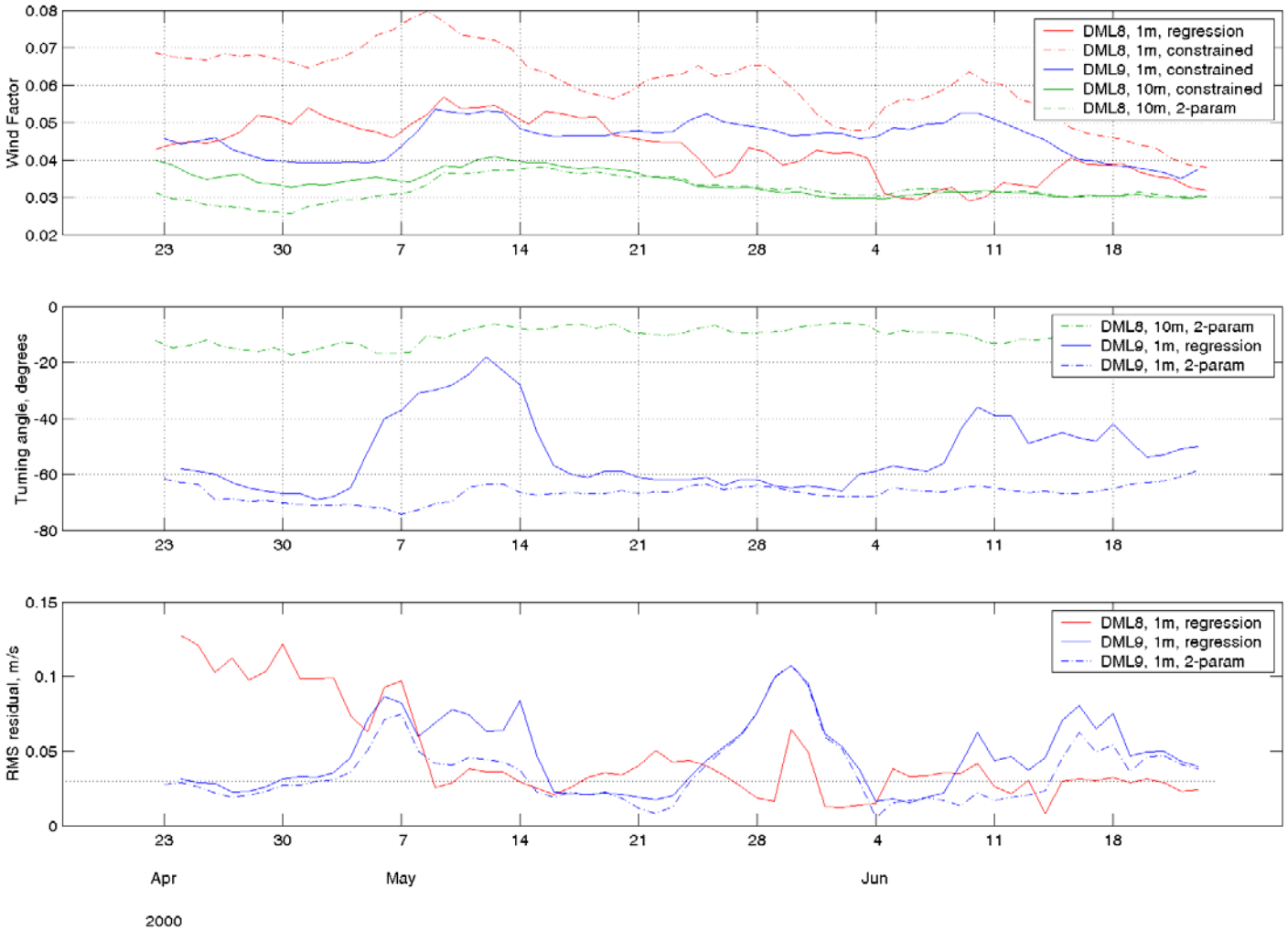

Figure 2.15: Wind factor (top), turning angle (middle) and residuals (bottom) for outer (DML8) and inner (DML9) array buoys, with the various schemes described in the text.

The success of the methods can be visualised by using the various coefficients to drive the buoys along simulated tracks. Figure 2.16 (a) shows the simulated drift for the lifetime of DML4, using its *in situ* winds to drive the simulations. Both regression and two-parameter techniques give a reasonable simulated track, reproducing all the major features of the motion, though in a slightly distorted manner. The two-parameter solution gives improved tracking of the rectangular portion of the track in its south-most location, however. Removing the residuals from the two-parameter solution shows the important role that these play in determining the motion, with the track becoming significantly displaced towards the southeast. The results of a fourth method – using median values of α and δ timeseries to give more stable results in the early deployment phase – are also shown, though, since the method also assumes zero residuals, its performance is similarly poor. Figure 2.16 (b) shows simulated tracks for the same buoy, using ECWMF 10 m winds. The lower temporal resolution of these winds is clear, with the simulated tracks lacking the detail of the actual buoy track. Major features are again well-reproduced, however, with a surprisingly accurate final position.

For the other, longer-lived buoys of the main array, simulations are presented (Figure 2.17) for the initial (pancake) phase and then for the remaining lifetime of each buoy. Only modelled (ECMWF) winds are shown, since three of these four buoys had faulty wind directions. As before, the two parameter technique consistently gives the best results and this success suggests that any momentum transfer parameters should be derived using this technique. Accordingly, values derived from valid *in situ* and ECMWF winds are presented in Table 2.5. Averaging results for the various buoys gives wind factors of 4.8% and 2.9% for 1 m and 10 m winds, respectively. Turning angles were 68º and 13º, for 1 m and 10 m winds, respectively. Residual component currents were rather low for *in situ* winds, at 0.6 cm s^{-1} and 1.6 cm s^{-1}, but significantly higher for modelled winds, at -4.5 cm s^{-1} and +2.3 cm s^{-1}. This is more likely to be a failing of the modelled winds than a real effect. Degree of explanation is high for *in situ* winds (0.83) and modelled winds post-consolidation (0.80), but lower for modelled winds in the pancake phase (0.58), as expected from the foregoing correlation analysis.

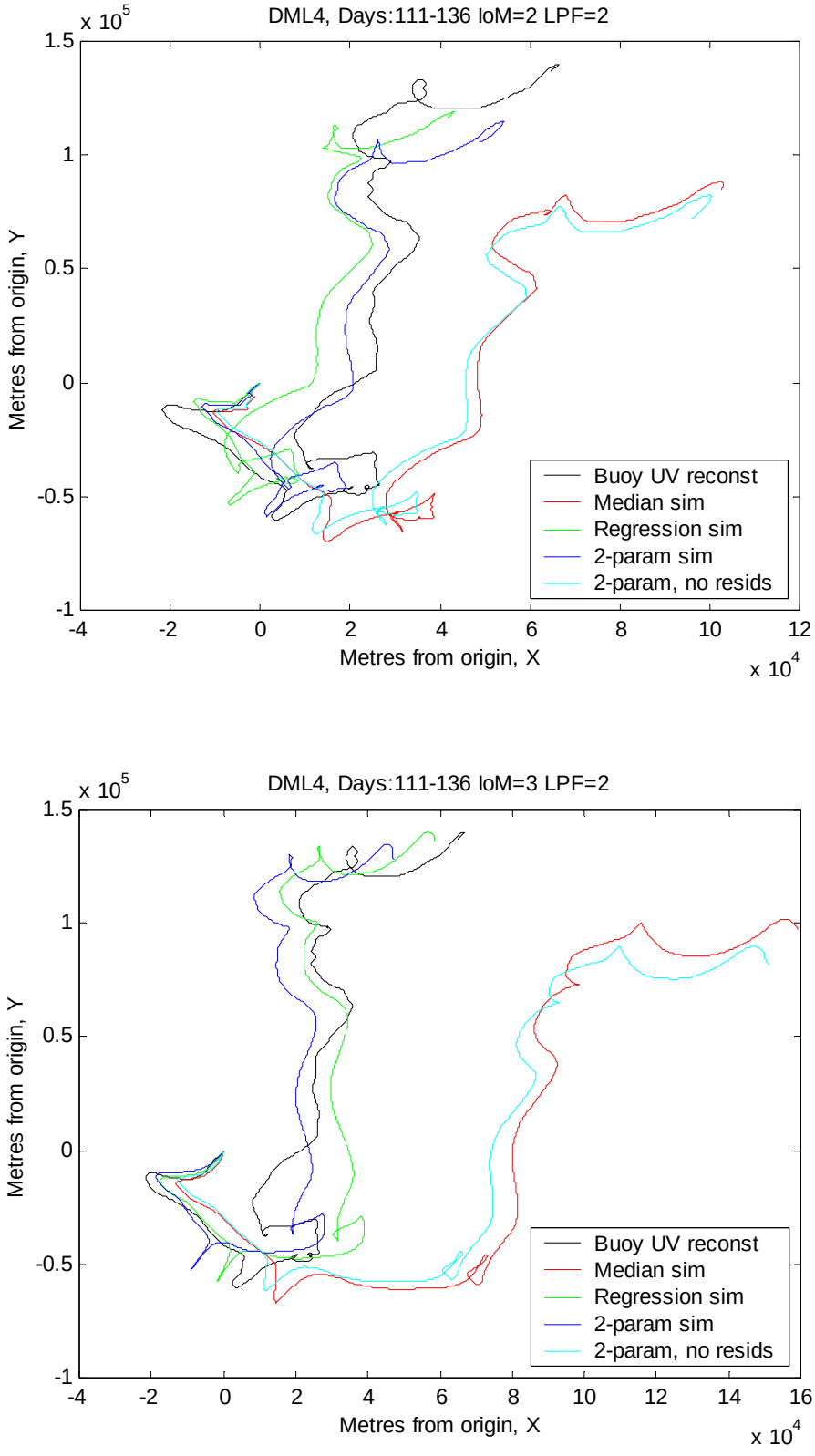

Figure 2.16: Simulated drift tracks of DML4 using (a - top) *in situ* and (b- bottom) ECMWF 10 m winds.

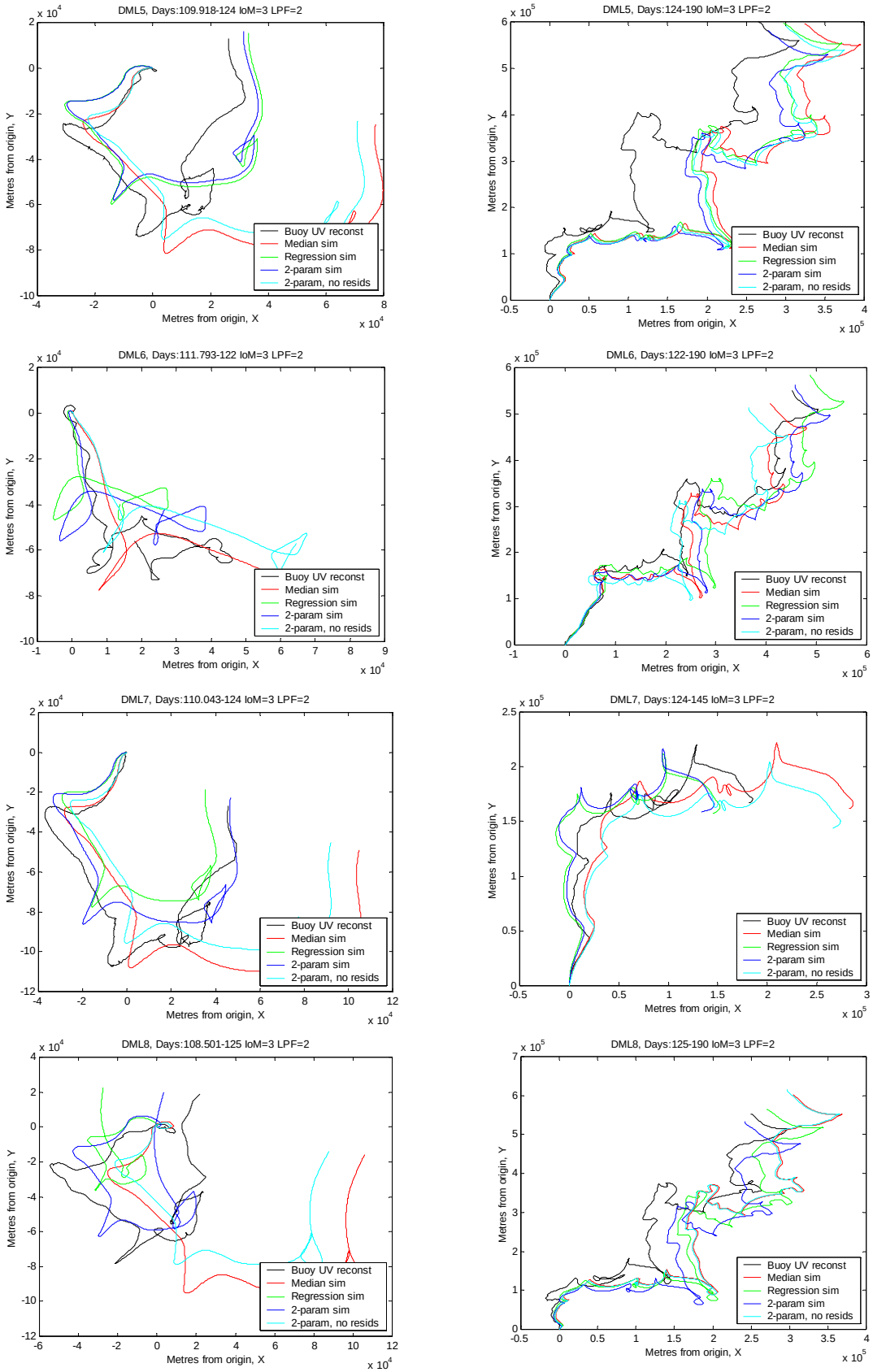

Figure 2.17 (a)-(h): Simulated drift tracks for pancake regime (LHS) and pack ice phase (RHS)

Table 2.5: Results from the two-parameter matrix solution, for (a) *in situ* winds, and (b) 10m model winds. Values are quoted during pancake/consolidated phases. DML4 and DML9 did not remain unconsolidated long enough to give meaningful figures. *In situ* results are omitted for the failed-compass buoys, since the nature of the solution does not allow any parameters to be calculated in the absence of valid wind directions. Timeseries have a two hour LPF applied before calculation, and points with wind speed <1m/s are omitted.

a) *in situ* winds

	α, %	δ, ^{o}	U_{res}, cm/s	V_{res}, cm/s	R^2	Comment
DML4	- / 4.2	- / -90	- / -2.7	- / 1.9	- / 0.85	To day 136
DML5	(4.9) / 5.4	(-83) / -66	(0.6) / 1.9	(1.6) / 1.8	(0.04) / 0.84	To day 190
DML9	- / 4.5	- / -64	- / 0.4	- / 1.3	- / 0.81	To day 190
2h mean	**- / 4.8**	**- / -68**	**- / 0.6**	**- / 1.6**	**- / 0.83**	
14h mean	**- / 4.9**	**- / -64**	**- / 0.5**	**- / 1.4**	**- / 0.89**	

b) 10m model winds

	α, %	δ, ^{o}	U_{res}, cm/s	V_{res}, cm/s	R^2	Comment
DML4	- / 2.4	- / -19	- / -4.8	- / 2.1	- / 0.70	To day 136
DML5	2.5 / 3.2	-16 / -13	-3.3 / -0.4	3.3 / -0.2	0.66 / 0.81	To day 190
DML6	2.8 / 3.1	-13 / -10	-4.4 / 1.6	1.7 / 0.8	0.70 / 0.87	To day 190
DML7	3.2 / 3.7	-9 / -9	-3.8 / -7.3	1.9 / 0.8	0.46 / 0.78	To day 145
DML8	2.9 / 3.3	-13 / -10	-5.9 / -1.0	2.4 / -1.5	0.57 / 0.84	To day 190
DML9	- / 2.7	- / -15	- / -2.3	- / 1.7	- / 0.75	To day 190
2h mean	**2.9 / 3.0**	**-13 / -13**	**-4.5 / -1.3**	**2.3 / 0.4**	**0.58 / 0.80**	
14h mean	**2.9 / 3.0**	**-13 / -12**	**-4.6 / -1.3**	**2.4/ 0.5**	**0.66 / 0.86**	

Literature values for pancake ice transfer coefficients are entirely lacking for the Antarctic and sparsely reported for the northern hemisphere. For the Odden region of the Greenland Sea, which consists of pancakes with no constraining boundary, *Wilkinson and Wadhams* (2003) reported a 10 m wind factor of 2.7% with a turning angle of 10°. These values were used by *Pederson and Coon* (2004) and are broadly consistent with the present study. Wind factor values for Antarctic pack ice are more common and are widely reported to vary, both seasonally and spatially. Authors variously quote 1.9% (August) to 2.7% (October) (Hoeber 1991); 3.4% in the MIZ to 2.4% in pack ice (Vihma and Launianen 1993); and 1.8% (Wamser and Martinson 1993). Differences are commonly ascribed to melting, which smoothes the underside of the floes and stabilises the oceanic boundary layer, decreasing momentum exchange and friction (McPhee 1987). Vihma and Launianen (1993) noted that the wind factor depended more on the location of the buoys with respect to the ice edge than seasonal influences, however.

2.6 Relative motion

Having examined the motion of individual buoys and the relation between wind forcing and ice movement, the next step is to investigate relative motions across the buoy array and pancake zone. It is relative motions which largely determine the final character of an ice region, since sustained convergence results in a highly deformed (and therefore thick) ice cover, criss-crossed by linear pressure ridges and less-defined rubble fields. The contribution of deformed ice to the mass balance of ice covered seas is currently a major topic of interest in the Arctic (*e.g.* the current Sea Ice: Dynamic Nature of the Arctic (SEDNA) experiment in the Beaufort Sea), since the contribution of deformed ice will significantly change the response of the Arctic pack ice to continuing global change. Deformed ice has been studied less in the Antarctic, primarily due to accessibility issues and the lack of military submarine voyages to the region, which otherwise would provide thousands of kilometres of upward-looking sonar data, as they have done in the Arctic (Rothrock *et al.* 1999; Wadhams and Davis 2000).

Conversely, sustained divergence (an increase in area) exposes open water to the cold air temperatures, allowing ice formation in an ice cover that may otherwise have reached its thermodynamic thickness limit. Alternating divergence-convergence cycles are most effective in driving ice formation, as the thin skim of ice is rapidly deformed to form thick ice before open water is again exposed for more growth.

The motions of the buoy array are therefore examined, particularly with regard to any divergence-convergence cycles which may occur at the higher frequencies whose examination is made possible by the 20-minute sampling interval of the buoys. Relative motions in an array are defined with respect to the centroid of the array. This is defined such that the sum of all distances in the array (x, y co-ordinates) from the centroid is zero. It can be visualised as the centre-of-gravity of a polygon with a buoy at each vertex.

2.6.1 Time domain

The behaviour of the array can be best visualised by splitting the buoys into two sub-arrays: the outer, more unconsolidated triangle of DML 5-7-8 and the inner triangle of DML 4-5-9. DML5 forms a common element in these two arrays. Figure 2.18 (a) and (b) plot the positions of the buoys in each array with respect to the array centroid with time, as a three-dimensional surface. It is clear that the outer array undergoes significantly more compression from its deployment, flattening to an almost linear form between Days 116 and 122. The array then re-establishes its shape under the influence of northerly winds from the passing low-pressure system. The inner array presents considerably more resistance to deformation, reflected by its more stable shape. Both arrays then diverge by similar amounts, reflecting the fact that sea ice is rather strong in compression but very weak in tension.

Relative motions between buoys were then studied quantitatively in terms of the standard differential kinematic parameters (DKPs) (Thorndike and Colony 1982; Crane and Wells 1994; Kottmeier *et al.* 1997; Geiger *et al.* 1998) which compute the deformation rates of the array using the spatial derivatives of the buoy velocities with

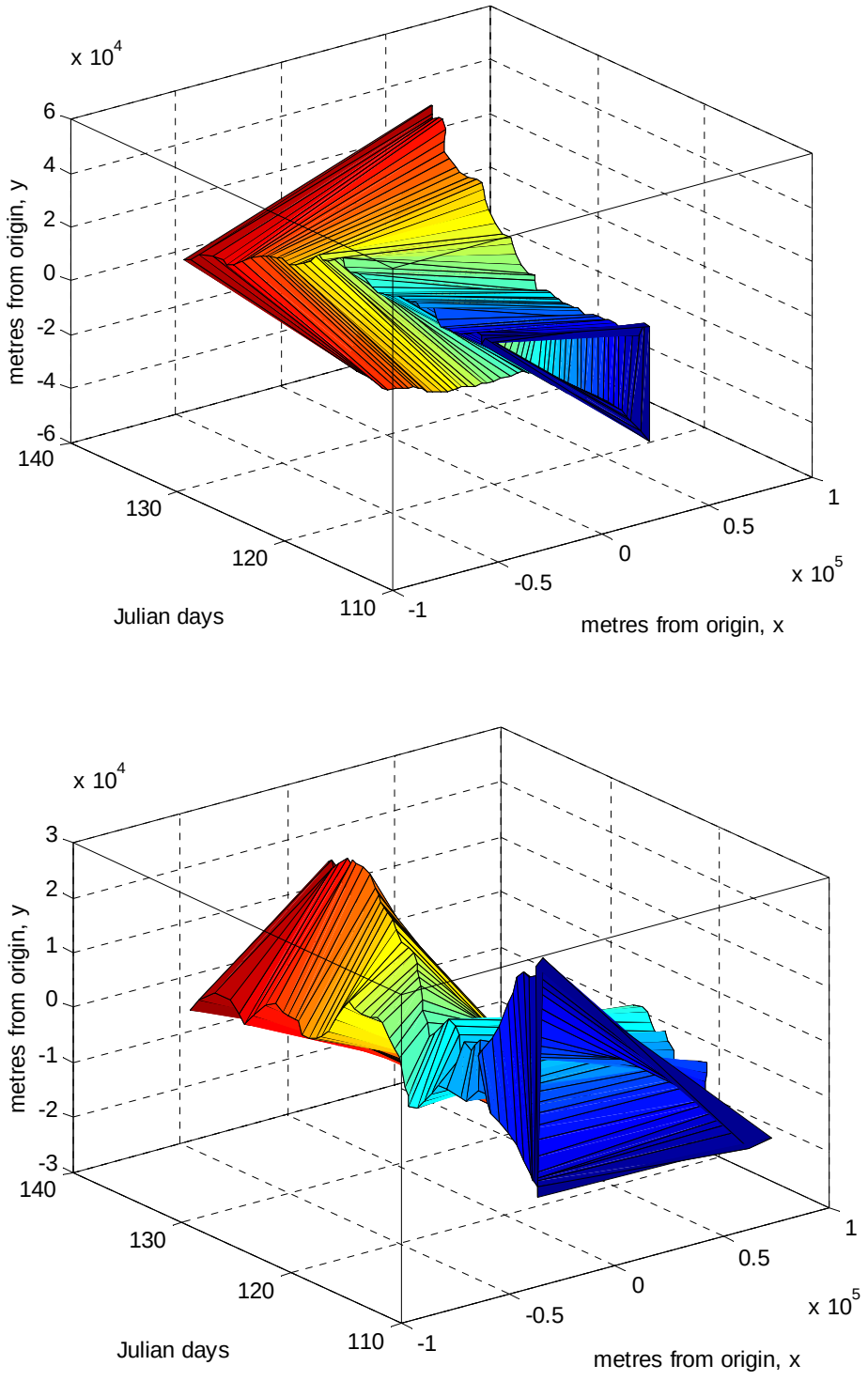

Figure 2.18: The relative positions of inner (top) and outer (bottom) arrays, plotted relative to the centroid of each array as a three-dimensional surface.

respect to the array centroid. We calculate the three invariant terms: divergence, vorticity and maximum shear and the two variants; shear and stretch. Divergence is the rate of change of area without change of orientation or shape; shearing is the rate of shape change produced by differential motion parallel to the sides of the area, without a change of that area; vorticity is the rate of rotation without area or shape change (no deformation). Invariant terms give results independent of the co-ordinate system chosen. Variant terms, dependent on the chosen co-ordinates, are useful when seeking information about the array with respect to external influences such as topography. The Cartesian co-ordinate system aligns with the ice edge in the current study and *x* is therefore taken parallel to longitude, while *y* is parallel to latitude.

DKPs were calculated by the line integral method detailed in *Lindsay* (2002), for all five buoys of the main array:

Invariant terms

$$Divergence = \frac{\partial u}{\partial x} + \frac{\partial v}{\partial y} \qquad \text{(Eq. 2.9)}$$

$$Vorticity = \frac{\partial v}{\partial x} - \frac{\partial u}{\partial y} \qquad \text{(Eq. 2.10)}$$

$$Max\ Shear = \left(\frac{\partial u}{\partial x} - \frac{\partial v}{\partial y}\right)^2 + \left(\frac{\partial u}{\partial y} + \frac{\partial v}{\partial x}\right)^2 \qquad \text{(Eq. 2.11)}$$

Variant terms

$$Shear = \frac{\partial v}{\partial x} + \frac{\partial u}{\partial y} \qquad \text{(Eq. 2.12)}$$

$$Stretch = \frac{\partial u}{\partial x} - \frac{\partial v}{\partial y} \qquad \text{(Eq. 2.13)}$$

The above quantities are calculated using the relation:

$$\frac{\partial u}{\partial x} = \frac{1}{2A}\sum_{i=1}^{n}\left(u_{i+1} + u_i\right)\left(y_{i+1} - y_i\right) \qquad \text{(Eq. 2.14)}$$

where (x_i, y_i) are the locations relative to the array centroid and (u_i, v_i) are the velocities with respect to the centroid. A is the area of the array, given by:

$$A = \frac{1}{2}\sum_{i=1}^{n}\left(x_i y_{i+1} - y_i x_{i+1}\right) \qquad \text{(Eq. 2.15)}$$

DKPs are presented for outer and inner arrays in Figure 2.19, plotting full-resolution parameters in light blue. The DKPs are also plotted with a two-hour LPF applied to highlight their oscillatory nature. Full-resolution DKPs show a high-amplitude, oscillatory character prior to consolidation in all cases. The parameters for the inner array have significantly less amplitude than those displayed for the outer buoys (the array DKPs are all plotted at the same scale). Actual translation of the array during these high magnitude differential events was small, with mean centroid velocities not exceeding 7 cm s^{-1}, directed towards the north-east. Secular divergence was largely negative until May 1st but became dominantly positive afterwards. The high frequency motion was not a function of the sign of the divergence, however – later prolonged convergent episodes (e.g. June 5th – 15th) elicited no such response from the array. Vorticity was dominantly negative (clockwise) until May 3rd, and then became oscillatory, with a clear semi-diurnal signal that was also evident in the post-consolidation divergence.

ECMWF 10 m winds were extracted at each buoy's position as well as at the array centroid and rotated by the turning angle calculated in the previous section prior to determination of their equivalent DKPs. These are largely uncorrelated during the pancake phase for the outer array, as expected from the model's poor performance there. Large amplitude excursions in max shear, shear and stretch at the consolidation boundary closely follow the wind forcing, however, and the sign of these DKPs matches thereafter. Correlation is better for the inner array, though divergence is poorly tracked. Shear and max shear match particularly well for this latter array.

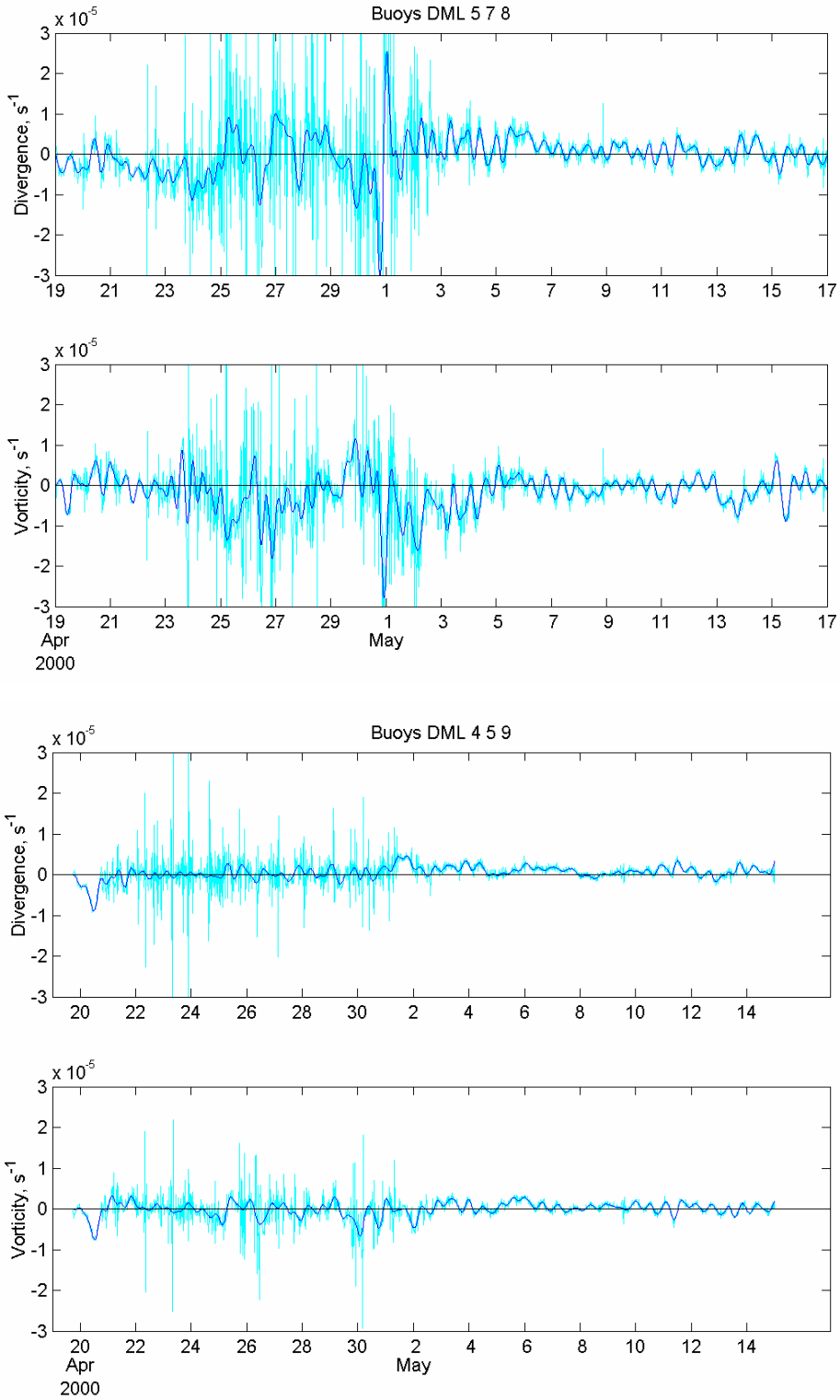

Figure 2.19: Divergence and vorticity plotted at 20-minute resolution (light blue) and with a two-hour LPF applied (dark blue). The top two graphs show the outer array (DML 5-7-8) while the bottom two graphs show the inner array (DML 4-5-9). RMS error in the divergence, due to "worst case" position/velocity errors of the individual buoys is 3.4×10^{-7} s^{-1}, two orders of magnitude below the plotted signal.

Results are summarised, along with results for the full array, in Table 2.6. The table shows full-resolution (20 minute) results for all derivatives and invariants, together with the scale of each array in terms of the median separation between buoys and the median area. Correlation coefficients compare like with like, applying a low pass filter to the drift results (12 hour) to match that implied by the six hour sampling interval of the ECMWF winds. The oscillatory character of the timeseries, around a near-zero mean resulted in standard deviation and RMS values being almost identical and hence only RMS values are quoted.

Table 2.6: RMS values for derivatives and invariants for full, inner (DML 4-5-9) and outer (5-7-8) arrays. Values for the drift derivatives and invariants are quoted at full resolution. The correlation coefficients between wind and drift invariants are quoted with the drift values low-pass filtered to match the 'native filter' applied by the wind's sampling interval (*i.e.* LPF=12 hours for ECMWF 10 m winds). Winds are rotated by the turning angle prior to calculation. The median area of the array over the period of interest (a divisor in calculating the invariants from derivatives) is also tabulated, together with the median spacing between buoys.

Array **Period**	**Full** **Pre**	**Full** **Post**	**Inner** **Pre**	**Inner** **Post**	**Outer** **Pre**	**Outer** **Post**
du/dx ($\times 10^{-6}$ s^{-1})	0.8	0.7	1.4	0.9	1.5	1.3
dv/dx ($\times 10^{-6}$ s^{-1})	0.9	0.8	2.1	1.1	1.6	1.3
du/dy ($\times 10^{-6}$ s^{-1})	2.7	1.2	3.0	1.0	10.0	4.2
dv/dy ($\times 10^{-6}$ s^{-1})	4.1	1.4	5.1	1.2	14.5	3.6
Median spacing (km)	82	132	48	80	33	54
Median area (km^2)	3390	8733	1186	3212	575	1457
Div ($\times 10^{-6}$ s^{-1})	4.1	1.7	5.1	1.5	14.5	4.0
Vort. ($\times 10^{-6}$ s^{-1})	3.0	1.5	4.1	1.4	10.5	4.5
Max Shear ($\times 10^{-6}$ s^{-1})	4.9	2.0	6.4	2.2	17.6	5.6
Div r_S^2 10 m	0.13	-0.23	0.04	-0.10	0.23	-0.21
Vort r_S^2 10 m	0.69	0.72	0.54	0.50	0.31	0.69
Max shear r_S^2 10 m	0.32	0.28	0.22	0.19	0.02	0.30

The dominant nature of the meridional derivatives is evident, with values for the outer array being three times that for the inner (or full) arrays during the unconsolidated phase. RMS values of the invariants drop by approximately three times across the consolidation boundary in all cases. Correlation coefficients with 10 m wind results are negligible for divergence in all cases (r_S^2 = 0.13 before consolidation, -0.23 afterwards) and pronounced for vorticity (r_S^2 = 0.69 before consolidation, 0.72 afterwards). Vorticity correlation for the outer array more than doubles after consolidation, from 0.31 to 0.69, while values are similar across inner and full arrays throughout. Max shear correlation is low and variable in all cases. Vorticity was also well correlated with the sea level pressure measured by the buoys (r_S^2 = 0.60). The effects of poor model winds during the unconsolidated phase were difficult to estimate, however, since the lack of *in situ* wind directions precluded any calculation of the 1 m wind DKPs for the array.

Major vorticity events have been shown to be present in the atmospheric pressure record with effectively zero lag (Crane and Wadhams 1996). In the current study, correlations with the atmospheric pressure record were better than 0.32, reaching 0.68 in older pack ice (DML 5-8-9, Days 140-160). An association with strong low-pressure events is clear from comparison of the timeseries, and is ascribed to the array position being at similar latitudes to the centre of these strong cyclonic events. Calculating the Laplacian of pressure improves the correlation further. The relation breaks down towards the end of the longest-duration array (Figure 2.20), as advection takes it northwards out of the major storm paths.

The real value of the post-SA/DGPS position values becomes apparent when comparing the significance level of these DKP signals with respect to their error variance. Previous studies have noted the high-frequency nature of deformation events (Geiger *et al.* 1998) and bemoaned the low signal-to-noise ratios that conventional Argos buoys implied. Error variance of the velocity derivatives is given by (Thorndike and Colony 1982):

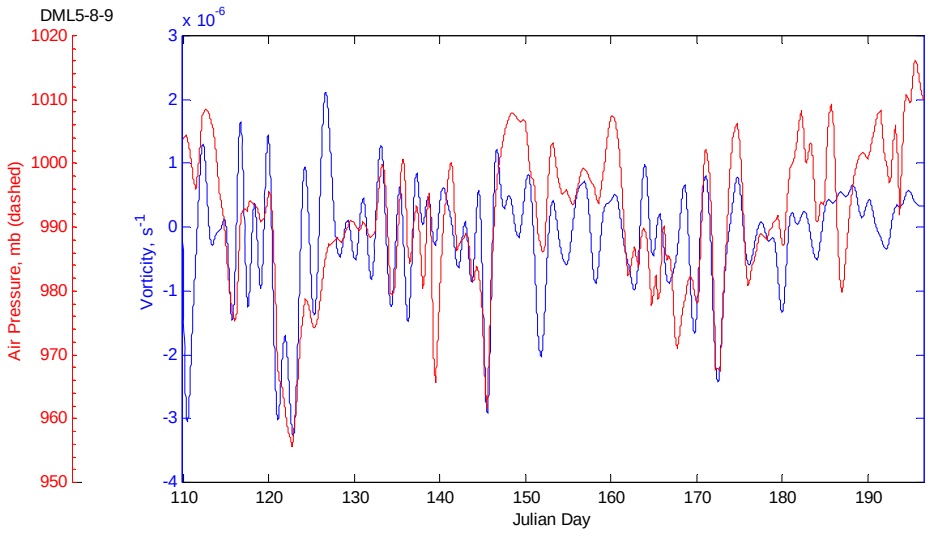

Figure 2.20: Atmospheric pressure at DML5 (red) plotted against 24-hour-filtered array vorticity (10 m winds). The association between strong low-pressure events and negative vorticity is clear in the early part of the record, though the relation breaks down towards the end.

$$\sigma_\varepsilon = \sqrt{\frac{4\sigma^2}{\Delta t^2 \Delta x^2}} \qquad \text{(Eq. 2.16)}$$

where σ^2 is the typical position error variance, Δx is the spacing of measurement points and Δt is the time interval of position fixes. Error variances for typical Argos buoys and the current buoys in 'worst-case' and 'best case' scenarios are shown in Table 2.7. Δx is taken as 200km in all cases. The post-SA position accuracy and the pre-SA differential position variances (20 m) give equivalent error variances to the three-hourly Argos fixes. Failed DGPS corrections during the SA-era increase this error significantly. Using two hour interval positions – broadly equivalent to most Argos studies – gives error standard deviations an order-of-magnitude better than achievable using Argos.

Table 2.7: Standard deviations of the velocity derivative error between typical Argos buoys and the current study, for various combinations of position error (σ) and sampling interval (Δt).

	σ (m)	Δt (sec)	σ_ε (s^{-1})
Argos	200	10,800	2×10^{-7}
STiMPI 'worst case': SA, DGPS failed	100	1,200	8×10^{-7}
STiMPI 'best case': post-SA or DGPS	20	1,200	2×10^{-7}
STiMPI 2hr LPF, post-SA or DGPS	20	7,200	3×10^{-8}

2.6.2 Frequency domain

Power spectral densities were calculated on either side of the consolidation boundary for the buoy invariants and are shown for the divergence of the inner array in Figure 2.21, together with equivalent spectra for their *in situ* winds. Results for vorticity were similar. The inner array is shown here, since all buoys had valid wind directions to enable this comparison to be performed. Figure 2.22 shows the divergence spectra for the full array. Drift divergence spectra had similar contrasts to those seen in the drift components themselves: power was higher in the unconsolidated phase and was especially elevated for periods less than six hours. Wind divergence spectra showed increased power pre-consolidation, in contrast to the wind speed spectra, which showed no actual increase in wind speeds across the consolidation boundary. Increased divergence in the absence of increased wind speeds suggest that the wind directions across the array were more disparate pre-consolidation than post-consolidation, consistent with the presence of the various mesoscale ice edge effects discussed previously. No evidence of elevated power at periods shorter than six hours is present in the wind data, though the one-hour sampling interval precludes examination below two-hours period. The oscillating 'tail' of the wind spectra below two hours in Figure 2.21 arises from interpolating the wind sampling interval to 20 minute intervals.

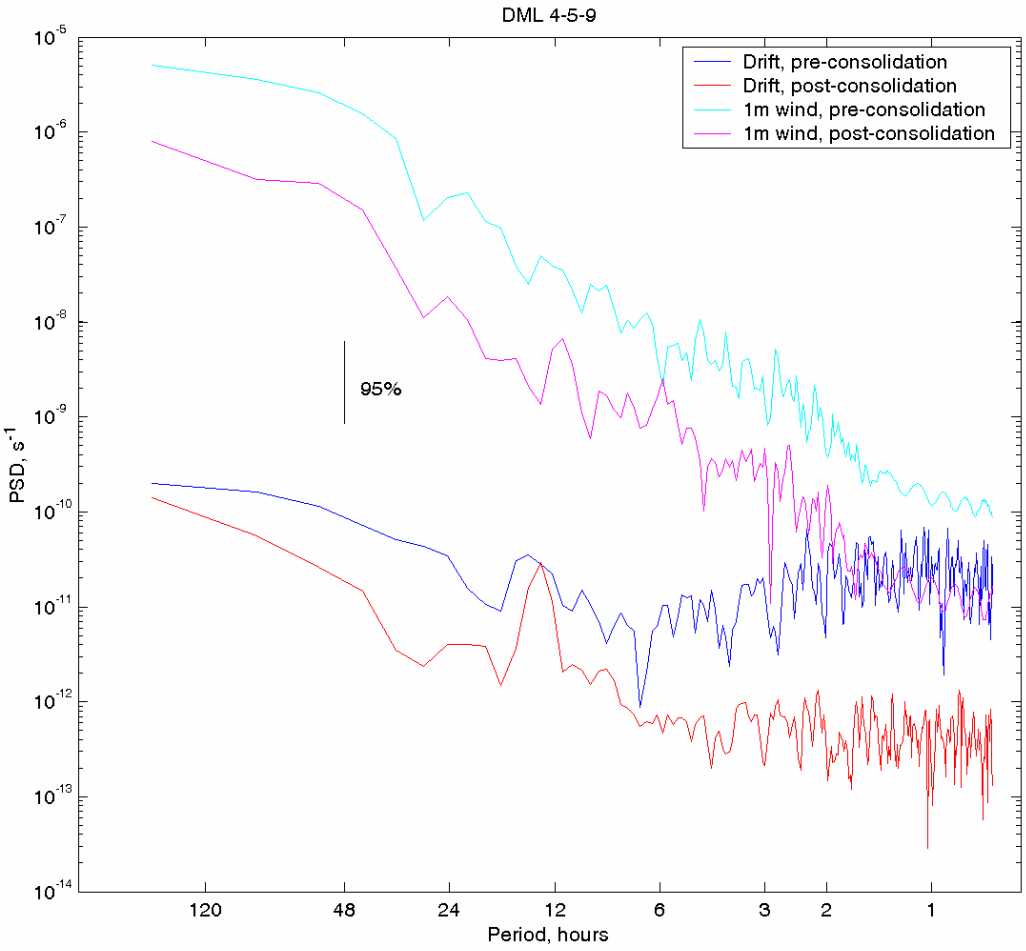

Figure 2.21: Divergence spectra for the inner, three-buoy, array, for similar-length periods before and after the consolidation. Equivalent spectra for the *in situ* wind measured by the buoys are also shown. Buoy divergence shows increased power at all frequencies pre-consolidation, but most markedly below 6 hours period. Wind divergence has higher power pre-consolidation, but HF power does not reflect the buoy results. The loss of resolution after two hours period is evident in the wind spectra; a consequence of the one hour sampling interval for these data (*c.f.* 20 minutes for buoy drift). The 95% confidence interval is marked.

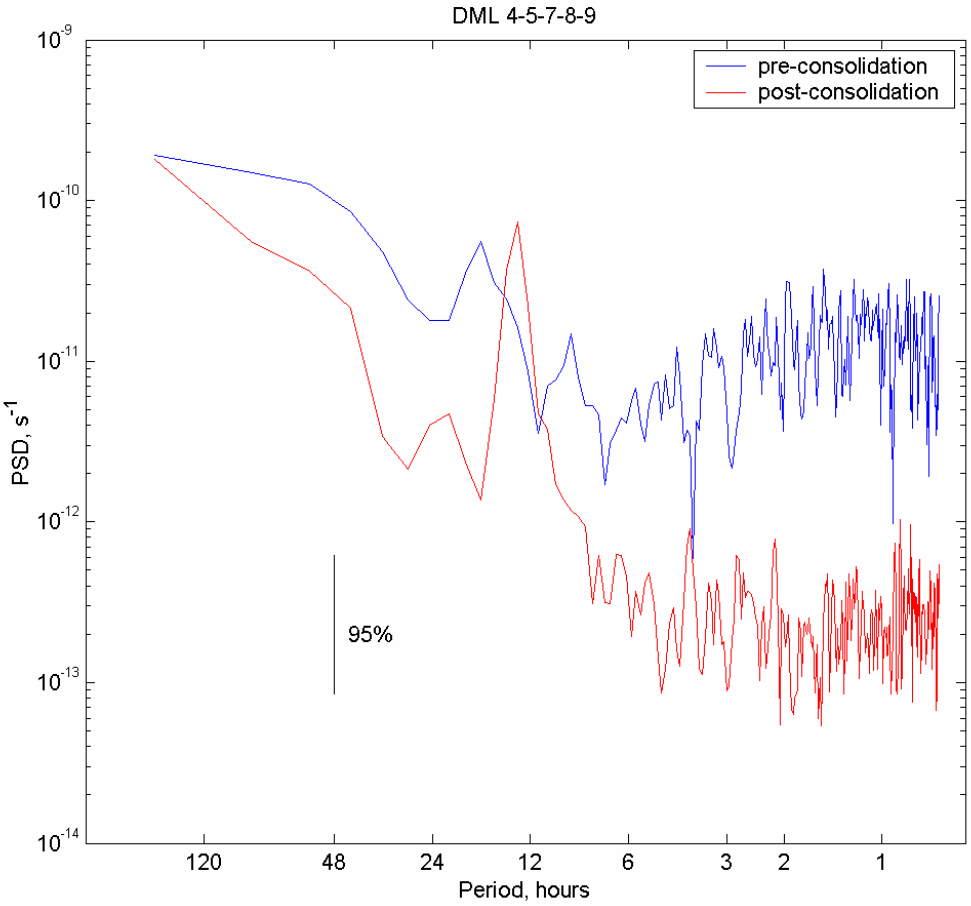

Figure 2.22: Divergence spectra for the full five-buoy array. The contrast between pre- and post-consolidation regimes is similarly dramatic, showing around two orders of magnitude increase at the highest frequencies. The development of the inertial peak post-consolidation is also particularly marked.

The evolution of the power in the DKP spectra was next investigated, as done for drift spectra in Section 2.3.2. The spectrum was divided into low-frequency (< 2 cpd) and high-frequency (2-36 cpd) portions. The integrated power in each frequency band was calculated for a ten-day running window, advancing in two day steps along the lifetime of the longest-lived array (DML 5-8-9) and plotted on a semi-logarithmic scale in Figure 2.23. The integrated power of the 10 m model wind DKPs is also plotted, calculated with the same running window, to a maximum frequency of 2 cpd.

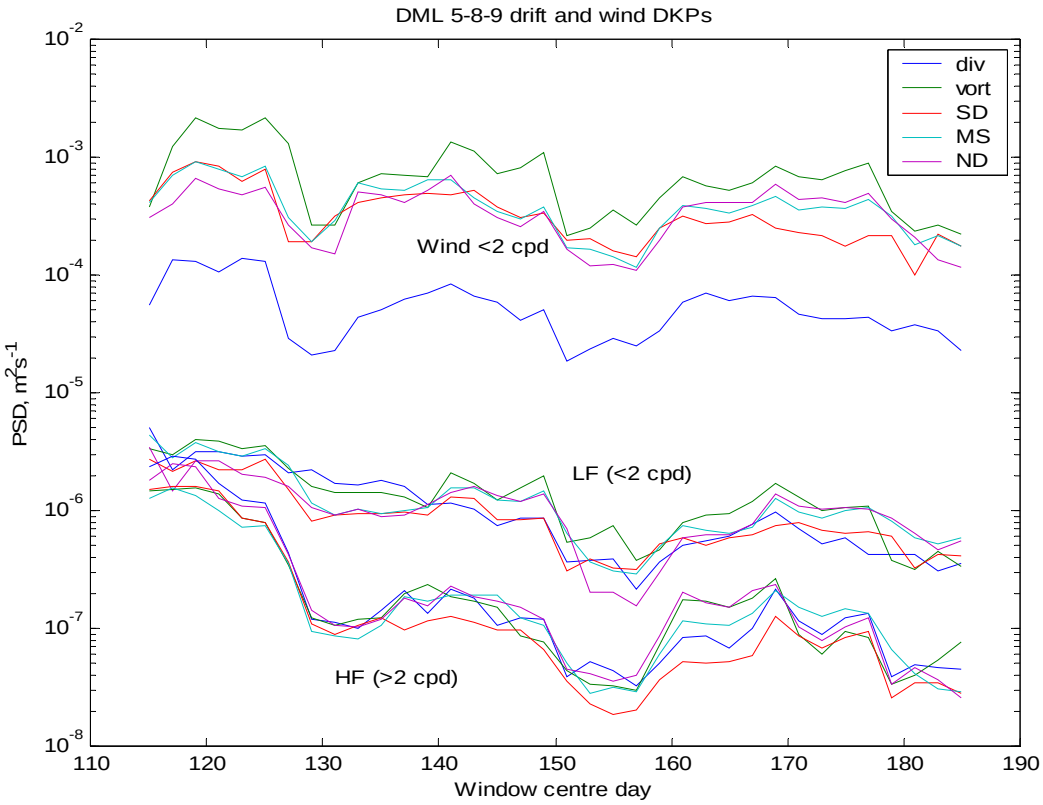

Figure 2.23: Integrated LF and HF drift DKP power and integrated wind DKP power plotted against the centre day of a ten-day window in which they were calculated. Spectra are not bandwidth-normalised.

For the drift DKPs, an exponential (log-linear) decay in both frequency bands is clear, with a minimum power around Day 150 and a less marked minimum at Day 130, matching similar features in the wind record. The decline in HF power is considerably steeper than for LF, as might be expected. Integrated wind DKPs show a similar decaying trend with a similar slope to the LF drift DKPs and it is clear that wind forcing is the dominant forcing at these low frequencies. Minima in the wind DKPs also correspond to features in the HF drift DKPs, implying that the wind forcing has a significant role in this higher frequency motion too, in contrast to the earlier analysis. Divergence of the wind is an order of magnitude less than the other wind DKPs which

are at least two orders of magnitude higher than for the buoy drift DKPs, in agreement with published results (Kottmeier *et al.* 1997).

RMS values of the DKPs showed marked variation with the period of low-pass filter applied and this prompted investigation of the dependence of the magnitude on sampling interval. This was done for all three arrays (inner, outer and full), calculating values for two periods, corresponding to the unconsolidated phase for the outer buoys and an equivalent period afterwards. Results are plotted for divergence in Figure 2.24.

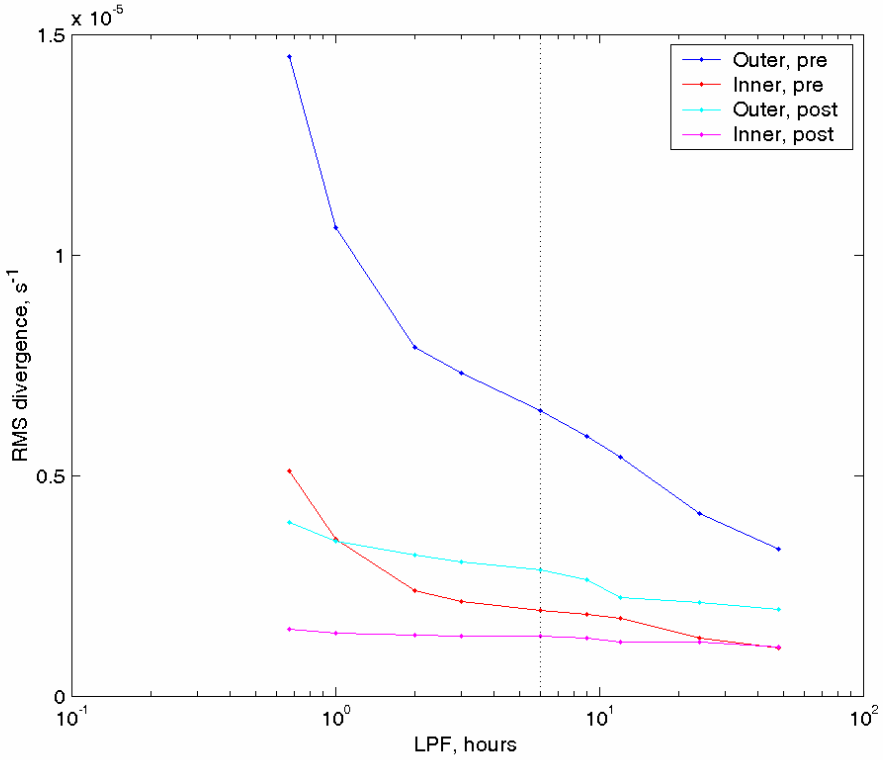

Figure 2.24: RMS divergence for the outer (DML 5-7-8) and inner (DML 4-5-9) arrays, plotted after the application of various low pass filters (LPFs). The 'native' low pass filter, imposed by the sampling interval, is 40 minutes period. The dotted line indicates the usual limit of Argos-based investigations, at a sampling interval of around three hours (LPF = 6 hours). A distinct break-point in the curve is seen at two hours.

The main feature of the graph is the steep decline in the magnitude of the outer array's pre-consolidation divergence with increasing filter length. A distinct break-point occurs at an LPF of two hours, after which reduction occurs at a lesser rate. The pre-consolidation period for the inner array has a similar form, though less exaggerated. A significant reduction in magnitude is seen between pre- and post-consolidation traces for both arrays, but particularly for the outer array, as might be expected. The post-consolidation outer array also shows a step at around 12 hours, following the removal of inertial motions not present in the pre-consolidation record. Results for vorticity were very similar and are not shown.

2.7 Discussion

The boundary between unconsolidated pancake ice and consolidated pack ice was clearly established with reference to wave parameters, buoy headings and drift dynamics. The high drift speeds encountered during the pancake phase fell gradually throughout the winter, only increasing when the ice neared its northern limit and began to break up and enter the Southern Ocean as individual floes. Scalar drift speeds during the pancake phase are higher than other studies (focussing on pack ice) have found in the region – e.g. 15 cm s^{-1} (Vihma and Launianen 1993; Vihma *et al.* 1996; Uotila *et al.* 2000), 17 cm s^{-1} (Massom 1992) and 11 cm s^{-1} (Geiger *et al.* 2000). The domination of the *v*-component reflects the approximately east-west alignment of the ice edge at the time of deployment and the consequent freedom in the north-south direction. Examination of the array shape showed strong variation in north-south separations as passing low pressure systems first compacted the unconsolidated ice with northerly winds, then rarefied the ice cover with southerlies. The pancake ice was unable to transmit the stress necessary to resist deformation, in contrast to the consolidated pack ice, and a buoy (or the ice) was thus free to move in response, giving rise to the high speeds observed. As buoys became consolidated, their freedom to respond to wind forcing was progressively reduced.

The most notable result of this work is the elucidation of high-amplitude, high-frequency divergence (and other invariants) for the unconsolidated ice. Drift spectra

showed significantly elevated spectral power at periods shorter than six hours in the pancake phase, approximately two orders of magnitude higher than previously seen for Weddell Sea pack ice (Kottmeier and Sellmann 1997). These high amplitude, oscillatory motions ceased overnight at the consolidation boundary. Though *in situ* winds showed increased power throughout the spectrum prior to consolidation, no comparable elevation of the HF spectrum was seen in those records.

The question naturally arises as to the forcing for these high frequency motions. Three candidates are suggested and these are examined in turn.

1. Surface gravity waves

The most evident form of higher-frequency motion is that caused by the passage of swell waves through the ice. While their primary role is preventing the pancake-frazil mixture freezing into a solid sheet – as discussed in Chapter 1 – swell waves cause the pancakes to move apart on each crest and move together in the troughs, as well as driving them in the down-wave direction.

The magnitude of the down-wave motion of pancakes is difficult to estimate. The usual mechanism – wave radiation pressure (Longuet-Higgins and Stewart 1964) – is applicable to objects whose dimensions are comparable with the wavelength of the driving waves. This is clearly not the case for pancakes, whose sub-metre diameters are around two orders of magnitude less than the wavelength of the shortest period waves impinging on them (*c*.150 m for a 10 s period wave). Accordingly, the energy reflection coefficient (Wadhams 1973) becomes vanishingly small and very little force is imparted to the pancake. An equivalent theory for the wave-induced motion of smaller elements was introduced by Ruhmer *et al*. (1979), who accounted for the ice elements sliding down a wave slope.

The approach was developed by Hopkins and Shen (2001), who added collisions to the model and simulated pancake drift numerically. Though an exact formulation for the real drift speed is hard to determine, and appears to be rather sensitive to wave amplitude, it is stated that the ice drift velocity approaches the water surface velocity at

low amplitudes. Taking a typical wave amplitude in the pancake zone as 1 m, with a 10 s period, their formulation gives an ice drift of around 18 cm s^{-1}. This gives 216 m motion between GPS fixes, which is of the same order as observed and suggests that no significant increase in the divergence signal would be observed if motions were sampled at higher frequency. It is unclear how surface waves would give rise to an oscillatory signal at the sampled interval, however.

Anomalous motion has been observed previously, during the MIZEX West experiments in the Bering Sea. Though never published, radar transponders mounted on small floes there were observed to circulate within ice edge bands. A complex interaction of short period waves within the band was postulated, though never developed.

Actual displacement through the surrounding frazil during the passage of swell waves appears to be minimal (pers. obs.), though the very large number of such events during a prolonged ice growth period suggests that even a small contribution-per-cycle may be important. Attempts to parameterise this mutual oscillation have encountered problems, with theoretical and measurement approaches giving inconsistent and contradictory results (Frankenstein 1996). Wave-tank experiments using polypropylene floes and urea ice in the CRREL outdoor tank found the results to depend on the initial conditions. The floe motions were quasi-periodic with outbreaks of chaotic behaviour and the theoretical treatment consistently under-predicted the collision frequency and duration, while over-predicting the oscillation amplitude (Frankenstein 1996). It is suggested that the inconsistent tank results may arise from the scaling problems referred to previously, *i.e*. that the frazil crystals are life-sized while the wave amplitudes and periods are not. It is not immediately clear how the required measurements could be made in the field, however. The very hostile environment encountered during pancake ice formation makes the observation and recording of centimetric pancake-to-pancake distances at sub-second intervals very difficult indeed, when the observation platform is heaving in a significant swell, high windspeeds and icing conditions.

2. Mesoscale wind and currents

The ice edge is an area of extreme contrasts in both thermal regime and surface roughness. Near the ice edge, in a strip of a width of a few baroclinic Rossby radii, the wind stress profiles are affected by several factors such as the roughness and compactness of the ice as well as by the stability of the atmospheric boundary layer (Guest and Davidson 1991). Such spatial variations of the wind stress give rise to divergences or convergences of the Ekman transport near the edge and thus generate up- or downwelling, and oceanic jets. Additionally, the surface temperature gradient across the MIZ generates a secondary circulation, or "ice breeze", causing atmospheric boundary layer convergence and deformation. This convergence effect is increased by the contrast in wind turning angles between water (relatively smooth) and MIZ ice (rough). Both effects favour the establishment of sharp, quasi-stationary temperature fronts, wind speed jets and strong vertical velocities near the ice edge. The effects are very sensitive to the balance between the ice breeze and geostrophic wind speeds and the exact angle of both relative to the ice edge (Guest *et al.* 1995), particularly in the case of winds parallel to the ice edge.

All of these factors suggest that the outer buoys will experience a significantly altered wind and/or current forcing to the inner buoys in the array. The *in situ* wind speed records, though showing differences between buoys, do not support a step change in high frequency wind forcing, however. It is also not clear how the forcing could be dominantly oscillatory. The role of water stress cannot be evaluated, since no current information was acquired, though it appears unlikely that ice edge currents would vary at the very high frequency observed, or, again, be oscillatory.

3. Internal waves

The observed motion might arise from coupling between internal waves and surface velocity. This was considered by Muench *et al*. (1983) in the formation of ice edge bands, though velocities in their shallow water case were insufficient to explain the observed motion. In the present case, CTD casts at each deployment station measured a density difference of 0.25 kg m^{-3} across the thermocline, which existed between depths of 60 and 110 m. This gives a Brunt-Väisälä frequency of 7×10^{-3} Hz, or a buoyancy

period of around 15 minutes. The maximum surface velocity that an internal wave of this frequency will produce is around $3\times10^{-2}A$, where A is the amplitude of the vertical displacement at the interface. This might be of order 10 m, giving a maximum horizontal velocity at the surface of 30 cm s^{-1}. The displacement integrated over one half period of the internal wave is therefore around 70 m, and internal waves thus appear to be a viable candidate for the observed motion.

Translation under wave action, whether surface or internal, may thus account for the elevated high frequency power observed. Clearly, the consolidation process either removes such forcing or prevents the ice from responding to it and can account for the contrast between results for the two ice types. Measuring buoy positions at still shorter sampling intervals would allow the mechanism to be established with more confidence.

The question then arises whether the accuracy of the GPS position fixes would make shorter sampling intervals feasible. Errors are difficult to estimate realistically, but if we assume a square array with buoys at each vertex, at mutual distance d, then an upper bound for the deformation error is (Lindsay 2002):

$$\varepsilon = \frac{e}{d\Delta t} \qquad \text{(Eq. 2.17)}$$

where e is the positional error (assumed independent) and Δt the fix interval. Positively correlated errors – as is likely if the buoys are calculating their positions from the same GPS satellites – can cancel, reducing uncertainty. This suggests that the fix interval could be significantly reduced without errors becoming significant. With SA-era accuracy, a timestep of five minutes would produce an error of 1×10^{-6} s^{-1} and post-SA, *i.e*. current, accuracy levels would allow this sampling interval to be reduced still further, to less than one minute for the same error.

It would be interesting to discover whether the upward trend in the RMS magnitude continues down to this level. If the driving factor in these oscillations is a mechanism such as translation by wave radiation pressure, then we would expect a positive result,

given the short period of the waves (7-8 seconds). Such a short interval would also resolve any oscillatory motion at internal wave periods.

The existence of the high-amplitude, high-frequency relative motions may have major implications for model rheologies of the region. Crushing thin ice during convergent events and exposing sea surface during divergence cycles is a particularly efficient ice growth process at high-frequencies (Padman and Kottmeier 2000; Koentopp *et al.* 2005) and the new values may therefore imply much increased ocean-atmosphere heat flux, ice growth and salt rejection to the ocean in the ice edge region. In order to estimate the contribution of these oscillatory events, we must combine the dynamics investigated in this chapter with an understanding of the thermodynamic growth of pancake ice and hence derive quantitative values for ice production rates in the pancake zone. This is done in the next chapter, using results from *in situ* ice sampling during the *Polarstern* cruise.

2.8 Summary

- The boundary between unconsolidated pancake ice and consolidated pack ice was established with reference to wave parameters measured by the buoys. The outermost buoys consolidated on May 2/3, after approximately two weeks deployment.
- Drift speeds were significantly higher during the unconsolidated phase and exhibited significantly elevated (an order of magnitude) spectral energies at periods shorter than six hours, compared to the immediately following consolidated motion. The difference was not reflected in the measured winds.
- The HF motion followed a cycle of constraint, having a maximum during the pancake phase, a mid-winter minimum and an increase towards break-out at the northern pack ice edge, during the following summer. Spectra at this latter maximum did not exhibit the elevated energies present in the pancake phase, however. The LF motion spectra maintained a more constant character throughout.

- It proved difficult to establish representative momentum transfer parameters for the pancake ice, due to the failure of the digital compasses in the outermost buoys and the resulting lack of reliable wind directions there. ECMWF winds were not reliable close to the ice edge, due to the many unparameterised mesoscale processes there. Best values were a wind factor of 2.9% and turning angle of 13° for the ECMWF 10 m winds, similar to that found in the Odden.
- Relative motions of the buoys, expressed by their differential kinematic parameters (DKPs) showed a striking contrast across the consolidation boundary. High amplitude, high frequency oscillations ceased almost overnight. RMS values were around two orders of magnitude higher than previously measured for Weddell Sea pack ice
- Power spectral densities of the DKPs exhibited elevated values at periods shorter than six hours, in the same manner as seen for the individual buoy drift components.
- RMS values of the divergence (and other invariants) showed a marked dependence on sampling interval, halving at two hours resolution compared to the full resolution data
- Possible forcing mechanisms were investigated and waves, either surface gravity or internal, were postulated as the source. It was noted that higher frequency measurements, coupled with relative water velocity measurements, would be required to investigate the mechanism further.

Results from this Chapter were published as *Doble and Wadhams* (2006) as part of a JGR Special Section titled "*Small scale kinematics and dynamics of sea ice: models and observations*". That paper is included as Appendix C to this thesis.

CHAPTER 3: THERMODYNAMICS

This chapter sets out *in situ* measurements performed in the pancake zone of the central Weddell Sea, aimed at elucidating initial ice formation processes and providing a first quantitative estimate of pancake ice growth rates.

Previously undescribed pancake morphologies are discussed and a new growth mechanism is introduced to account for these, supported by direct observations from ice tank experiments. Growth periods contributing to pancake building are identified and the rate of pancake formation compared to that which would have occurred by congelation ice growth and frazil ice production at a free surface, calculated using a kinematic-thermodynamic model.

In order to quantify the rate of ice growth during pancake formation, the ice properties – thickness, porosity, area concentration – must be determined and the meteorological forcing known. Intensive ice sampling was therefore carried out at each buoy deployment location: six sampling locations formed a trapezoidal area of dimensions 80 km perpendicular to the ice edge and 110 km parallel to the edge. A seventh location was sampled 310 km further west.

3.1 Overview of ice/ocean/atmosphere conditions

Helicopter reconnaissance flights were carried out prior to the sampling stations, in order to determine the best locations for buoy deployments and place the local conditions in a wider context. Tracks of the flights are shown in Figure 3.1, superimposed on the ship's cruise track, with sampling stations marked. The ship was steaming east to west.

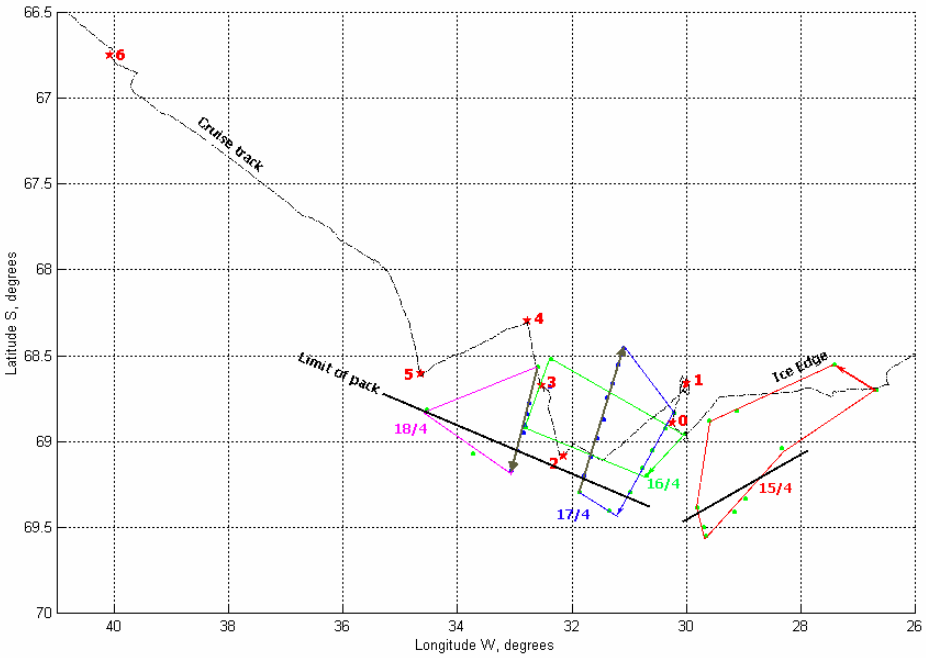

Figure 3.1: Helicopter reconnaissance and aerial photography flights (coloured polygons), superimposed on the ship's cruise track and the sampling (and buoy deployment) stations. No buoy was deployed at Station 0. Also indicated is the approximate limit of consolidated pack ice (solid black lines).

Vast fields of frazil ice were observed along the ice edge during the first flight (April 15th) for more than two degrees of longitude. The frazil fields consolidated overnight and were observed as young, wet pancakes during a helicopter flight the following day (April 16th). These young pancakes are shown in Figure 3.2, overleaf, which also shows the penetrating wave energy so important in their formation.

As well as basic reconnaissance, the helicopter flights were also used to fly downward-looking aerial photography transects across the pancake zone and into the consolidated pack ice. A Vinten 70 mm aerial camera was attached to the helicopter's skids and fired automatically every five seconds, to produce a continuous photo-transect during the flight. Figure 3.3 shows one example frame, over flying the ship to confirm dimensions on the photographic negative.

Figure 3.3: An example photograph taken by the downward looking 70 mm camera. The ship (length 118 m) was overflown at operational height (400 m) to provide verification of the frame geometry from known dimensions

Figure 3.2: (a), top: Pancakes near the ice edge, observed from the ship's helicopter at 3000 ft. The penetrating wave energy can be seen, propagating from top right to bottom left. Also visible are stratus clouds, typical of the ice edge region (b), bottom: A closer view of the same area showing the individual pancakes. The open water patches and ripple-like waves are caused by a surfacing pod of Minke whales, common in the area.

Areal coverage of each ice type was then determined from these transects. The 70 mm negatives were scanned and analysed using the freeware "Scion Image" programme. Ice type coverage at each station is shown in Table 3.1.

Table 3.1: Fractional area coverage of ice types at each sampling station. Ice types are classified as: pancakes f_p; frazil f_f; open water f_{ow} and thin congelation ice or older consolidated floe pieces f_{floe}. Inner/outer/middle refer to the stations' position with respect to the ice edge.

Station	f_p	f_f	f_{ow}	f_{floe}
0 (outer)	0.55	0.35	0	0.10
1 (outer)	0.60	0.35	0.05	0
2 (inner)	0.60	0	0.20	0.20
3 (middle)	0.55	0.30	0.05	0.10
4 (outer)	0.50	0.40	0.10	0
5 (inner)	0.65	0.30	0	0.05
6 (long scale)	0.45	0.40	0	0.15

The very young ice cover at the outer ice edge showed a very gradual reduction in frazil or young pancake concentration to the north. The term 'ice edge' is therefore rather subjective, and in this study was taken as the point at which the ice cover became so diffuse that damping of incident swell waves was considered negligible. The outer sampling stations (1 & 4) were performed within 15 km of this line. Mature pancakes upwards of 1 m diameter formed the remainder of the study area, from a penetration of approximately 54 km to 95 km from the 'edge'. The first inner station (2) was performed to the south of the new frazil formation zone (*c*. 94 km penetration), and no frazil was seen in this area. Consolidated pack ice was found at 10-15 km further penetration from the line joining the two inner stations.

The final station (6), to the west of the main area, took place within 4 km of the ice edge, though this was of an entirely different character since the cover had been compacted southward into a sharply defined edge by an approaching deep low pressure. This pressure system had not yet begun to influence the main area during the study, though subsequent rapid southerly movements of the drifting buoys confirmed that this occurred shortly after *Polarstern* left the region.

CTD profiles were also taken at each sampling location and showed a mixed layer salinity of 34.35 psu within 0.01 ^{o}C of its freezing point. Mixed layer depth was approximately 60 m, indicating that the maximum winter depth had not yet been achieved, as expected. Profiles at Station 3 (the middle buoy) are shown in Figure 3.4 and are typical of the array area.

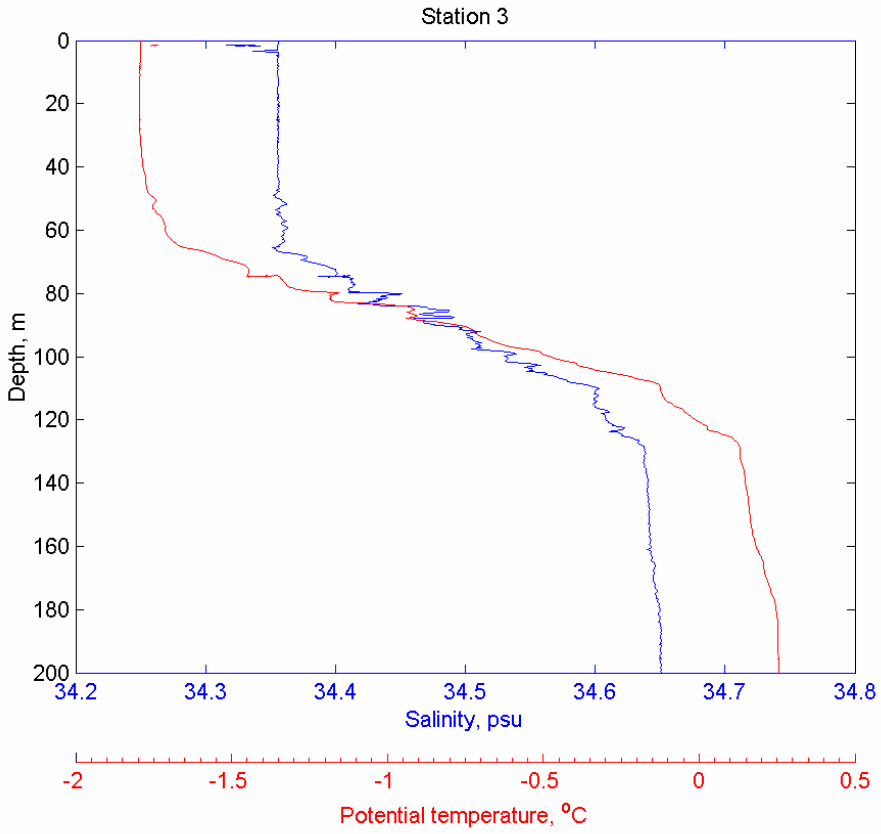

Figure 3.4: CTD profile at Station 3 (DML5), in the centre of the array.

Meteorological conditions were determined from *in situ* measurements while the ship and buoys were in the vicinity, and ECMWF re-analysis fields beforehand. An example of the gridded ECMWF sea level pressure and 10 m winds is shown in Figure 3.5, superimposed on ice concentration from the SSM/I instrument using the DTU algorithm.

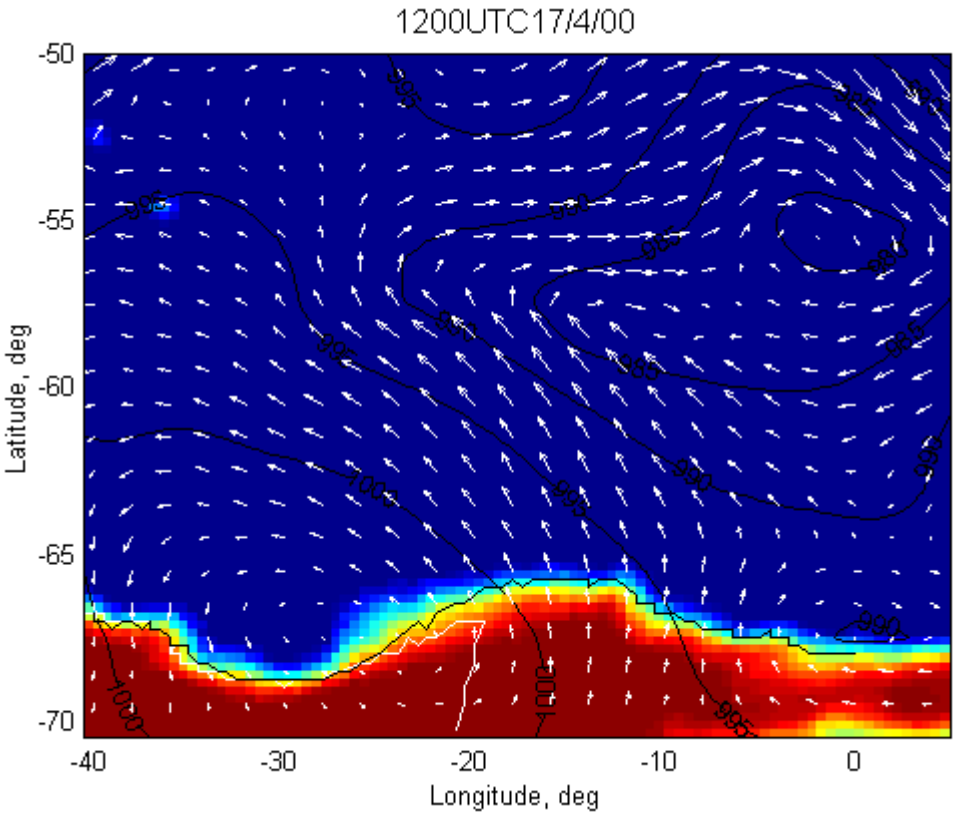

Figure 3.5: Example output from the ECMWF model of sea level pressure (black contours) and 10 m winds (white arrows, length proportional to windspeed). Data are superimposed on a background of passive-microwave-derived ice concentration, using the DTU algorithm (courtesy Leif Toudal, DTU). Dark blue represents open water, dark red is 100% ice concentration. The black line shows the 60% ice concentration limit. The continuous white line shows the ship's track as it approached the sampling area. The embayment into which the buoys were deployed can be seen, centred on 30°W.

Meteorological conditions during April 2000, derived from the European Centre for Medium-range Weather Forecasts (ECMWF) analyses (ECMWF 1997), show two

periods of low air temperature and high wind. These occurred from April 7th – 10th and again from April 15th – April 17th. They were separated by a period of calm and relatively high air temperatures (-3°C), which also occurred following the second low-temperature event, *i.e*. during buoy deployment and sampling operations.

Weather conditions were therefore extremely favourable as they represent two distinct ice formation events separated and followed by essentially 'steady state' periods during which ice neither melted nor grew significantly. The two ice growth periods are referred to as "Event 1" and "Event 2" from hereon. This allowed the date of frazil and pancake ice formation in the region to be determined with some degree of confidence, considerably simplifying the task of establishing ice growth rates.

3.2 Ice sampling

3.2.*1 Methods*

Pancake ice was lifted onto *Polarstern*'s working deck using a one metre square 'ice basket' and the aft crane. The basket retained seawater in its lower section to minimise brine drainage and temperature changes in the recovered pancake before sectioning. Once on deck and removed from the basket, the pancakes were immediately cut in two along one diameter. A vertical temperature profile was then taken down the centre of one half, using an electronic probe thermometer inserted to several centimetres depth from the exposed wall at 5 cm intervals. Ice samples were then quickly taken and bottled for later salinity analysis, as described in Wadhams *et al*. (1996). Samples were also taken from the top surface and rim if the pancake had not been submerged during the lifting process. All sampling was done as quickly as possible to minimise brine drainage during the sampling process, though it is accepted that some drainage is inevitable. A remotely-operated vehicle (ROV), carrying an upward-looking video and 35 mm still camera, was deployed at three stations (0, 3 & 6) to verify that the pancakes sampled were representative of the general pancake population. Figure 3.6 shows a view of the pancakes at Station 3, taken from the ROV.

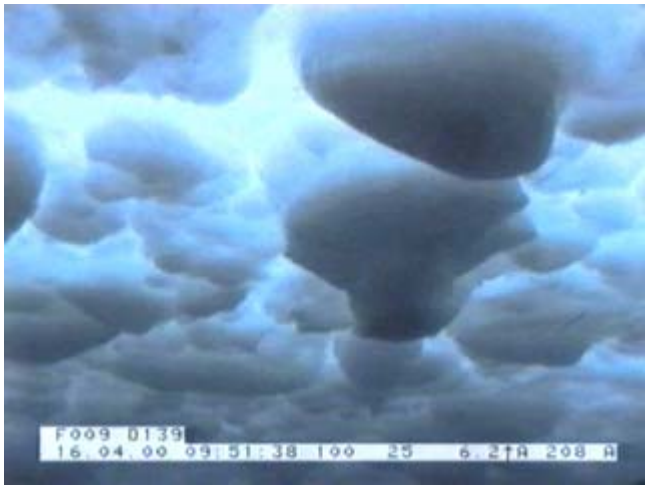

Figure 3.6: A view of the ice cover at Station 3, taken from the Sprint ROV. The ROV was operated by Andreas Starmans (AWI), who otherwise employed it largely for examination of seabed life during the cruise.

The frazil ice filling the interstices between pancakes was also sampled, using the ship's 'mummy chair' and aft crane. Sampling was done using a 30 cm length of polythene tubing, 8 cm in diameter, with slots cut in the side and open base covered by 300 μm plankton netting. The device was weighted to allow it to sink through thick frazil layers. Sampling was done by dropping the device down through the frazil, moving it to one side and pulling it up through the frazil slush. Water drained through the plankton mesh and the resulting frazil crystals were bottled, melted and analysed for salinity and melted volume. Figure 3.7 shows the author engaged in frazil sampling operations at Station 3: the "frazilometer" can be seen on the end of the rope.

Figure 3.7: The author and Oliver Peppe (Dunstaffnage Marine Laboratory) conducting frazil fishing operations at Station 3. Sampling was done from the 'mummy chair' to avoid biasing results due to compression of the frazil/pancake mixture observed close to the ship's side.

3.2.2 Results

A total of 36 pancakes were lifted at seven stations. The pancakes presented some unusual morphologies which have not previously been described in the literature. They were divided into six classes depending on their major features, and example photographs of each type are shown in Figure 3.8.

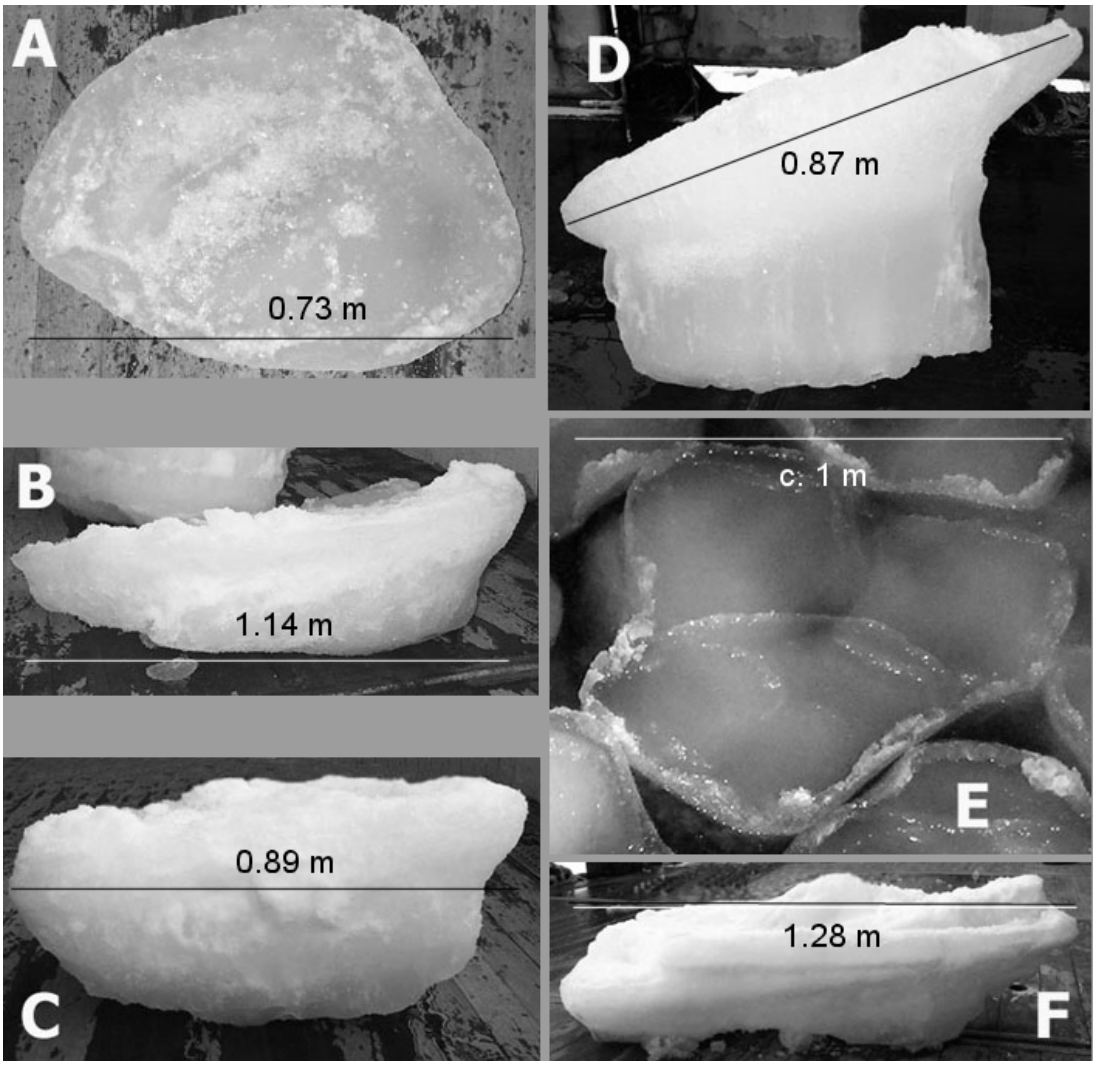

Figure 3.8: Photographs of pancakes divided into six types according to their features. The pictures show, from top left: *Type-A*: the classic pancake, formed from cyclic accretion of frazil ice; *Type-B*: a pancake having a highly porous lower layer, similar to the overlying layer; *Type-C*: a pancake with a low-porosity bottom layer, representing an older pancake on top of which the younger top layer has been formed; *Type-D*: a pancake with a columnar ice bottom layer; *Type-E*: a pancake formed from an agglomeration of two or more similar pancakes; *Type-F*: a pancake with rafted pancakes included.

Type-A describes the 'classic' pancake form – largely flat or saucer-shaped, with lesser or greater development of raised rims. Stations 1 & 4 (the outer ice-edge locations) consisted entirely of this type. *Type-B* pancakes had a characteristic two-layer structure, with the bottom layer formed from frazil ice retaining a high porosity similar to the overlying layer. Salinities of lower and upper layer were very similar for this type, though a clear 'step' between the two layers existed - the upper layer having a larger diameter than the lower. *Type-C* pancakes had a frazil-grown lower layer of significantly lower porosity than the overlying layer and were found exclusively at station 6. These layers displayed a lower salinity than the upper layer (e.g. 3.2 psu *vs.* 5.6 psu) and were also clearly stepped. *Type-D* pancakes had a bottom layer of columnar ice up to 44 cm thick, which often displayed open, rotted brine channels. Vertical temperature profiles throughout *type-D* pancakes were essentially isothermal, indicating that the columnar ice was not actively growing. A clear demarcation existed, both externally and in section, between the bottom and the overlying frazil-grown layer, with the now-familiar step being particularly marked. Salinities of the lower layers of this type were again much lower than their overlying layers (e.g. 3.7 psu *vs.* 6.3 psu). Examples were found at all stations other than the two ice-edge locations. Top layers of all two-layer types were commonly wedge-shaped, as can be seen in the photographs of Figure 3.8, with the top surface at a considerable angle to the bottom surface of the pancake. *Type-E* pancakes are formed as an agglomeration of smaller pancakes, and *type-F* pancakes are rafted. The ROV flights showed that the proportion of rafted pancakes was low in the experimental area, other than in the immediate area beside the ship where they had been pushed aside by the hull. It should be emphasised that no difference between *types A-D* could be discerned from visual examination of their top surfaces from the ship.

The properties of all 36 pancakes sampled are detailed in Table 3.2, which also classifies the pancakes according to the above scheme.

Table 3.2: Summary of measurements for the 36 sampled pancakes. *Type* refers to the classification given in Figure 3.8. Thickness *h* and salinity *S* are given for both pancake layers (top and bottom), where present, with *NA* (not applicable) entered for the lower layer measurements of single-layer pancake types. A dash indicates that no measurement was taken. Superscripts next to salinity measurements refer to the number of samples contributing to this figure (one, if not indicated). Question marks in the thickness columns indicate that the complicated pancake structure made attribution of the layers unreliable. Shaded cells serve to separate the stations. Outer-middle-inner refer to the position in relation to the ice edge.

Station	No.	Type	h_{top}, cm	h_{bottom}, cm	S_{top}, psu	S_{bottom}, psu
0 (outer)	1	B, E	15	10	12.9	12.5
0 (outer)	2	D	9	44	-	5.1
0 (outer)	3	D	22	22	7.6^{2}	3.7
0 (outer)	4	B	20	6	-	-
1 (outer)	5	A	5	NA	11.6	NA
1 (outer)	6	A	8	NA	11.8	NA
1 (outer)	7	A	7	NA	11.6	NA
1 (outer)	8	A	7	NA	12.8^{10}	NA
1 (outer)	9	A	5	NA	13.0	NA
2 (inner)	10	D	29	20	-	4.5
2 (inner)	11	D	25	25	6.3	2.4
2 (inner)	12	D	23	35	-	5.2
2 (inner)	13	D	27	17	10.9	4.8
2 (inner)	14	D	20	15	6.8^{14}	6.4^{5}
3 (middle)	15	D	19	33	-	-
3 (middle)	16	D	27	29	11.7	4.2^{3}
3 (middle)	17	B, F	?	?	-	-
3 (middle)	18	A	9	NA	-	NA
3 (middle)	19	B, F	12	6	-	-
3 (middle)	20	D, F	19	22	-	-
3 (middle)	21	D	15	26	-	-
4 (outer)	22	A	11	NA	-	NA
4 (outer)	23	A, E	10	NA	-	NA
4 (outer)	24	A	10	NA	11.1^{7}	NA
4 (outer)	25	A	11	NA	-	NA
4 (outer)	26	A	9	NA	-	NA
5 (inner)	27	B	14	6	-	-
5 (inner)	28	D	?	?	-	-
5 (inner)	29	B	20	10	-	-
5 (inner)	30	B, F	20	9	-	NA
5 (inner)	31	D	21	14	-	-
6 (long scale)	32	C	25	23	11.7	-
6 (long scale)	33	C	16	16	13.1	3.6^{2}
6 (long scale)	34	C	22	17	6.7	3.2
6 (long scale)	35	C	18	14	-	-
6 (long scale)	36	C	25	10	-	-

Samples taken from the very top surface of the pancakes were always markedly more saline than the body of the pancake itself, usually double the bulk value or greater (*e.g.* 15.2 psu *vs.* 6.4 psu). Rim salinities were comparable to the upper bulk layer (*e.g.* 6.0 psu *vs.* 5.6 psu). The bulk salinities of the pancake ice formed at each station rank with distance from the ice edge: the outer stations (0, 1 & 4) have the highest salinities at 11.0, 12.5 and 11.1 psu respectively, the middle station (3) has an intermediate salinity (8.2 psu) and the inner ice edge stations (2 & 5) have the lowest (6.4 and 5.4 psu).

A total of 59 frazil samples were taken and allowed to thoroughly drain before bottling the resulting crystals. Frazil salinities were invariably greater than that of pancakes recovered at the same location. The youngest pancakes, at stations 1 and 4, had salinities approximately 5 psu lower than the corresponding frazil. Frazil salinities ranged from 9.5 psu (station 6) to 18.9 psu (station 1). Frazil salinities were consistent within a station while displaying distinct differences between stations. This coherence at a particular station suggests that the sampling method was consistent. It is interesting to note that the mean frazil salinities at a station also tend to indicate its distance from the ice edge; with the outer stations most saline and intermediate stations (0, 3) also fitting the pattern. No frazil was present at the first inner station (2). The second inner station (5) is the only one not to fit the pattern, having a mean frazil salinity higher than that for the intermediate station 3 (14.2 psu *versus* 11.7 psu).

We also calculate the frazil slick 'solid ice equivalent' (SIE) thickness from the melted sample volumes. It has been shown that the salinity of any brine enveloping the drained mixture is very similar to that of the seawater surrounding it (Smedsrud and Skogseth 2006), therefore the seawater volume fraction in the melted sample (Vf_{sw}) is related to the salinity of the melted sample (S_m) by:

$$S_m = S_{sw} \,.\, Vf_{sw} \qquad \text{(Eq. 3.1)}$$

The original volume of frozen ice is then given by:

$$V_{ice} = \frac{V_{melt}}{0.92}\left(1 - \frac{S_m}{S_{sw}}\right) \qquad \text{(Eq. 3.2)}$$

Where V_{melt} is the volume of the melted sample and 0.92 is a volume correction factor based on the relative densities of fresh water (1000 kg m^{-3}) and pure ice (920 kg m^{-3}). The SIE thickness of the frazil slick is then given simply by:

$$h_{SIE} = V_{ice} / \pi r^2 \qquad \text{(Eq. 3.3)}$$

where r is the radius of the sampling device (4 cm). Note that the method requires no assumptions about the volume fraction of ice in either the frazil slick or the drained sample. The change in density between the seawater at its freezing point and at the melted sample temperature (15°C) is ignored, since the effect is small (0.2%) compared with sampling inaccuracies, as indicated by the spread of results at each station. Volume, salinity and the derived SIE slick thickness for each frazil sample are detailed in Table 3.3.

3.2.3 Discussion

The greater salinity of the current study's upper pancake layers compared to their lower (observed in all cases) contrasts with previous pancake measurements, performed in the Odden region of the Greenland Sea during winter cruises in 1993, 1997 and 2000 (Wadhams *et al.* 1996; Wadhams and Wilkinson 1999). Those pancakes displayed increasing salinity with distance from the top surface, consistent with the classic bottom accretion process. The salinity of the pancake falls rapidly after formation since its highly porous structure allows unimpeded gravity-driven brine drainage (Tison and Verbeke 2001). The underside remains the most saline, however, since the enveloping layer of brine around those frazil crystals has had less time to drain. Melt- and rainwater flushing also occurs in the Odden region (Wadhams and Wilkinson 1999), due to air temperatures frequently rising above 0^oC, and reinforces the characteristic profile. Odden pancakes were apparently all single-layer types (excluding simple rafted examples). The unusual structure of the Weddell Sea pancakes in relation to this

Table 3.3: Frazil sample details. Volume refers to the melted volume and h_{SIE} is the solid ice equivalent thickness of the frazil slick, calculated according to Equations 3.1-3.3. Shading serves to delimit measurements at each station. Inner/outer/middle refer to the stations' location with respect to the ice edge.

Station No.	**Vol cm^3**	**Salinity psu**	**h_{SIE} cm**
0 (outer)	366	16.5	4.1
0 (outer)	482	14.4	6.1
0 (outer)	362	14.1	4.6
0 (outer)	55	17.4	0.6
1 (outer)	84	18.9	0.8
1 (outer)	164	16.3	1.9
1 (outer)	90	16.9	1.0
1 (outer)	138	16.0	1.6
1 (outer)	80	14.2	1.0
1 (outer)	50	15.8	0.6
3 (middle)	218	12.0	3.1
3 (middle)	220	10.4	3.3
3 (middle)	289	12.3	4.0
3 (middle)	440	11.2	6.4
3 (middle)	448	11.8	6.4
3 (middle)	444	12.3	6.2
3 (middle)	424	11.6	6.1
3 (middle)	157	11.5	2.3
3 (middle)	310	11.7	4.4
3 (middle)	304	11.3	4.4
3 (middle)	122	13.6	1.6
3 (middle)	400	11.1	5.9
4 (outer)	238	16.7	2.6
4 (outer)	100	17.1	1.1
4 (outer)	273	16.7	3.0
4 (outer)	194	17.7	2.0
4 (outer)	202	14.0	2.6
4 (outer)	338	15.9	3.9
4 (outer)	142	16.6	1.6
4 (outer)	126	16.2	1.4

Station No.	**Vol cm^3**	**Salinity psu**	**h_{SIE} cm**
4 (outer)	196	16.6	2.2
4 (outer)	144	17.2	1.6
4 (outer)	376	17.9	3.9
4 (outer)	140	18.5	1.4
4 (outer)	135	16.5	1.5
5 (inner)	-	13.6	-
5 (inner)	273	13.0	3.7
5 (inner)	180	15.1	2.2
5 (inner)	230	12.9	3.1
5 (inner)	268	12.0	3.8
5 (inner)	136	15.3	1.6
5 (inner)	266	13.3	3.5
5 (inner)	124	14.6	1.5
5 (inner)	209	18.3	2.1
5 (inner)	142	14.2	1.8
5 (inner)	-	13.6	-
6 (long scale)	126	12.0	1.8
6 (long scale)	475	9.8	7.3
6 (long scale)	468	9.4	7.4
6 (long scale)	476	8.5	7.8
6 (long scale)	590	9.0	9.4
6 (long scale)	528	8.7	8.5
6 (long scale)	285	10.0	4.4
6 (long scale)	350	8.4	5.7
6 (long scale)	290	10.5	4.4
6 (long scale)	382	10.3	5.8
6 (long scale)	254	9.4	4.0
6 (long scale)	395	8.4	6.5
6 (long scale)	576	8.4	9.4

familiar morphology therefore brings into question the bottom accretion process as the sole formation method.

The higher salinity of the upper layer is not unusual for consolidated Weddell Sea pack ice; *Eicken* (1992) found this to be the most common salinity profile, and arises since the salinity of congelation ice is closely related to its growth velocity (Cox and Weeks 1988). The initial, fastest, growth therefore results in the highest salinity ice. Top layer salinity enhancement can also occur by upward brine expulsion and impeded brine drainage from later top-layer accretions such as snow ice formation, which is common in the Weddell Sea (Lange *et al.* 1990). The post-consolidation evolution of the ice tends to blur any salinity contrasts within the original layers, giving similar profiles for largely frazil-grown (granular) ice or dominantly congelation ice cores. These top-layer salinity enhancement processes do not occur in unconsolidated, growing pancakes, however. Individual frazil crystals reject most of their brine in their buoyant ascent to the bottom surface of the slick (Ushio and Wakatsuchi 1993) and the pancake is thus built from relatively constant salinity material. No significant snow deposit was observed on the pancakes and no barrier exists to brine drainage through the pancake, except perhaps in the case of *type-D* pancakes.

The *type-D* pancakes are particularly striking, since no mechanism exists whereby 44 cm of congelation ice can form beneath a frazil-grown layer whose salinity and porosity suggest it is only a few days old at most. The relative layer porosities observed in *type-C* pancakes are also reversed from the expected bottom accreted types, which typically have a “slushy” bottom surface and hard top surface (Shen *et al.* 2001). We therefore postulate that existing pieces of ice act as platforms for the accretion of a younger top layer. That platform can variously be an existing, much older pancake (resulting in a *type-C* composite) or a thin columnar ice piece (giving a *type-D* pancake). *Type-B* pancakes represent a midpoint between *type-A* and *type-C*, since frazil rafting can commence as soon as a *type-A* pancake has grown to sufficient strength to act as a rigid platform without breaking. This explains the lack of contrast between the porosities of bottom and top layers seen in *type-B* pancakes, since the age difference between the layers is small. The mechanism is conceptually similar to the more familiar rafting

process, though in this case the over-riding ice is unconsolidated frazil rather than a solid ice piece. The top growth mechanism thus gives rise to a coherent 'family' of pancakes. The bottom accretion mechanism is inconsistent with the salinity and temperature profiles and cannot account for the observed morphologies.

Top layer growth of pancakes has been directly observed by the author under laboratory conditions in ice-tank experiments at the HSVA "Arctelab" facility in Hamburg, Germany, as part of the INTERICE program (Thomas and Wilkinson 2001). Congelation ice pieces, formed overnight in the still tank, were placed in the wave-influenced area during the next day's pancake ice growth. Frazil ice accretion occurred rapidly on top of these platforms, forming *type-D* pancakes. This top layer was considerably thicker than the conventional (*type-A*) pancake growth which occurred alongside over the same period (thickness 2 cm versus 0.5 cm for the *type-A*s). Salinity of the two *type-D* layers showed similar contrast to those in the field, at 15 psu upper *versus* 11.9 psu lower. *Type-B/C* pancakes were also commonly observed in the tank and Figure 3.9 illustrates one such example, clearly showing the more open, porous, top layer.

The top surface of pancakes observed in the ice tank was invariably wet, indicating a constant supply of water – and hence frazil – to the top surface. The alternative explanation of this wet surface - melting due to elevated salinity - is discounted, since it would have required a surface salinity of over 150 psu in the *c*. -10^{o}C air temperatures present in the tank; an order of magnitude greater than measured.

Derived frazil slick thicknesses (Table 3.3) are low, with a mean of 2.9 cm and standard deviation of 1.7 cm, excluding the long-scale station (6) which was not representative of the main array area. This equates to a physical slick thickness (dividing by the volume fraction) of 7.2 ±2.4 cm. Though the physical slick thickness was never measured directly, observations from the ROV suggest that this value is reasonable, since the pancakes were always observed to have considerably more draft that the surrounding frazil crystals.

Figure 3.9: A *type-C* pancake formed in the HSVA wave-tank. The line indicates the division between layers of markedly different porosity.

Frazil salinities are rather low compared with field measurements of actively forming grease ice (generally more than 20 psu) made in Størfjorden (Smedsrud and Skogseth 2006). This is consistent with the timing of formation, based on ECMWF temperature and wind fields, if it is assumed that a frazil suspension ages (reduces in salinity with time) in the same manner as pancakes. Though a frazil slick cannot 'reject' brine in the same way as pancakes – it is after all simply a suspension of pure ice in seawater – it is presumed that the slick becomes gradually more compact (in volume terms) as the buoyancy of the individual crystals continues to reduce the seawater-filled pore space in the absence of turbulence. The proportion of seawater is therefore reduced, together with the bulk salinity. This supposition is bolstered by the relatively high volume concentrations observed in the slicks (*c*. 0.4) compared to other field and laboratory observations, which suggest values closer to 0.2 or 0.3 (Voropayev *et al.* 1995; Winsor and Björk 2000; Smedsrud 2001; Smedsrud and Skogseth 2006). Such an observation also suggests that the frazil volume concentration should vary across the stations in the same manner as salinity, though this was not systematically studied at the time.

3.3 Modelling layered pancake growth

The two-layer structure observed complicates the establishment of growth rates for pancake ice, since it is likely that upper and lower layers grow at differing rates, given the distinct mechanisms involved. We expect the overtopping process to allow faster accretion since the frazil crystals are directly exposed to the cold air temperatures. To establish these rates, the formation of the layers was examined with reference to a kinematic-thermodynamic ice model. The two-layer structures are reproduced by identifying distinct growth events from the meteorological record and growing ice layers accordingly.

3.3.1 Methods

The model is divided into kinematic and thermodynamic parts. The kinematic model begins from a known observation time and position (such as an ice station) and calculates the backwards trajectory, using wind factors and turning angles derived in the previous chapter, until the beginning of a formation event. Forcing data is extracted along this track. The thermodynamic model then grows ice forwards from this event time, using the extracted data to force a simple, one-dimensional, energy balance model. Full details of the energy balance model are given in Appendix B. Six-hourly time-steps are used to grow:

(i) A congelation ice cover, as would occur in the absence of any oceanic turbulence.

(ii) Frazil ice. It is assumed that the presence of the frazil slick does not modify the ocean-atmosphere heat flux and that the whole ‘open water’ heat flux is used for ice production. This represents the maximum possible ice production rate for a given forcing, as used in previous studies (Bauer and Martin 1983; Alam and Curry 1998).

We expect the rate of ice production for upper and lower layer pancake growth to lie between these limits and compare the observed rates with the modelled bounds.

3.3.1.1 Data Assimilation

Forcing fields were taken from merged *in situ* and model data: *Polarstern* meteorological data, transferred to the standard levels from sensor heights following Smith (1988), are used while the ship occupied the main study area (days 106.5-110.0); ECMWF analysis data are used at other times. Parameters used are sea-level atmospheric pressure, wind at 10 m height, 2 m air temperature, 2 m dewpoint temperature (when using model data), relative humidity (when using ship data) and cloud cover fraction. When *in situ* data are used, these are taken as representative of the entire (relatively small) survey area. Though not ideal, the errors resulting from this approach are considerably smaller than the discrepancy between ECMWF and *in situ* measurements during this period, discussed below.

Comparisons of *in situ* and model data show that the ECMWF data significantly under-represent the severity of low air temperature events – a tendency also seen in previous comparisons (Markus *et al.* 1998; Vihma *et al.* 2002) and attributed to over-estimation of the cloud cover fraction (Vihma *et al.* 2002). This is unfortunate, since thermodynamic growth models are particularly sensitive to air temperature variations. To increase the validity of the ice growth model during purely model-forced periods, we therefore calculate a T_{model} to $T_{in\ situ}$ relation, shown as a scatter plot in Figure 3.10.

Scatter between the two data sets is large, principally due to the effect of varying ECMWF wind directions, which do not account for mesoscale effects near the ice edge. When ECMWF and in situ wind directions are aligned – whether 'off ice' or from the ocean to the north – offset and scatter are reduced. The absence of reliable *in situ* wind direction measurements from the outer buoys (discussed in Section 2.5) makes it difficult to establish a systematic correction for this factor, however. Considerable scatter also arises when comparing values in the relatively coarse ECMWF grid (1.125° × 1.125°) to the point measurements from the buoy. An empirical approach is therefore taken to matching the two datasets: *In situ* air temperatures above –5°C are generally higher than modelled, while temperatures lower than –8°C are fitted with a considerable offset. Modelled values between –8°C and –5°C bear little consistent relation to *in situ*

measurements, and we fit these values using a line of continuity between the two outer ranges.

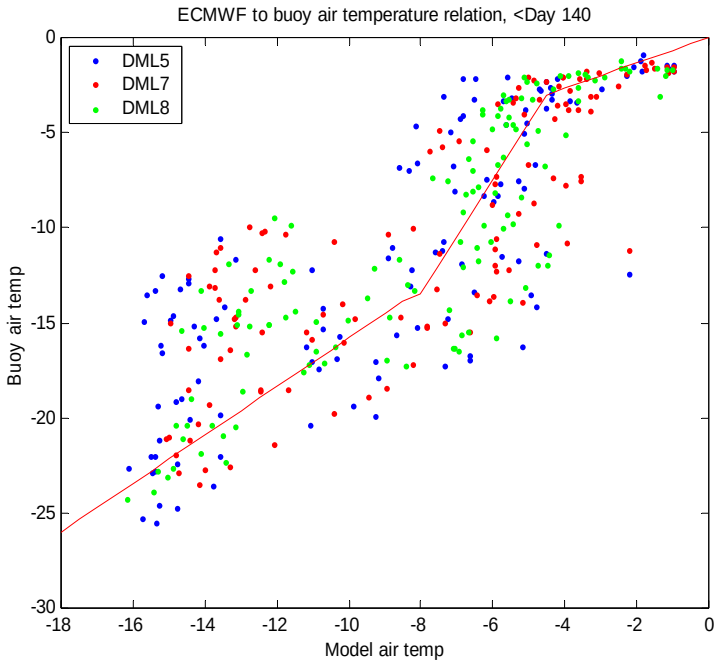

Figure 3.10: *In situ* air temperatures plotted against ECMWF 2 m temperature analysis, from day 111 (April 20th) to day 140 (May 19th). Symbols indicate results taken from three outer ice edge buoys - released at stations 0, 1 & 4 - with the ECMWF forcing extracted along their track. The three-piece line indicated was used to relate the two temperatures. The dotted line indicates the ideal correspondence between the two parameters.

The equations relating modelled and *in situ* temperatures are:

$$T_{model} > -5^{o}C: \quad T = 0.47\,T_{model} - 1.08 \qquad \text{(Eq. 3.4)}$$

$$-8^{o}C \le T_{model} \le -5^{o}C: \quad T = 2.83\,T_{model} + 10.94 \qquad \text{(Eq. 3.5)}$$

$$T_{model} < -8^{o}C: \quad T = 1.08\,T_{model} - 3.07 \qquad \text{(Eq. 3.6)}$$

The effect of the correction on the ECMWF 2 m temperature timeseries is illustrated in Figure 3.11(a). High temperatures between the ice growth events are slightly elevated and the severity of the low temperature events is greatly enhanced. The ship data during event 2 are far more closely tracked by the corrected forcing. Buoy data, from day 111 (April 20th), are also better followed though with variable success. The increased variability of the buoy data - swinging rapidly between extremes of temperature as the wind direction changes from an off-ocean to an off-ice direction – is clearly demonstrated and is poorly tracked by the model. The corrected forcing is taken in preference to the 'raw' model data, though we are aware of the empirical nature of this correction and continue to cite uncorrected forcing results throughout, in addition to the corrected figures. The dotted line (close to 0°C) shows the temperature (actually – 0.6°C) at which we consider the surface of the pancakes to undergo melt. Air temperatures – either modelled or corrected – only exceed this value early in the period shown, around Day 85. No surface melt occurs during our periods of interest, indicated by the two arrows in the diagram.

Figure 3.11 (b) plots ECMWF "total cloud cover", T_{cc}, and relative humidity, *Rh*, taken from shipboard measurements or calculated from the ECMWF 2 m dewpoint temperature fields (Rogers and Yau 1989), as appropriate. The cloudy nature of the ice edge is clearly indicated by the T_{cc} plot, which rarely deviates from unity. The relative humidity oscillates within a fairly narrow range of values, being mostly around 90%.

Wind speed - Figure 3.11 (c) – and direction – Figure 3.11 (d) - are plotted for ECMWF output and *in situ* measurements. The model output shows the familiar properties, discussed in the previous chapter, of being relatively poor while the buoys were close to the ice edge (days 111 – 120) but reliable once they became embedded in the pack ice. Ship and buoy air pressure measurements were transmitted to the global telecommunication system (GTS) and used by the ECMWF model. Modelled winds are therefore not independent of the *in situ* measurements.

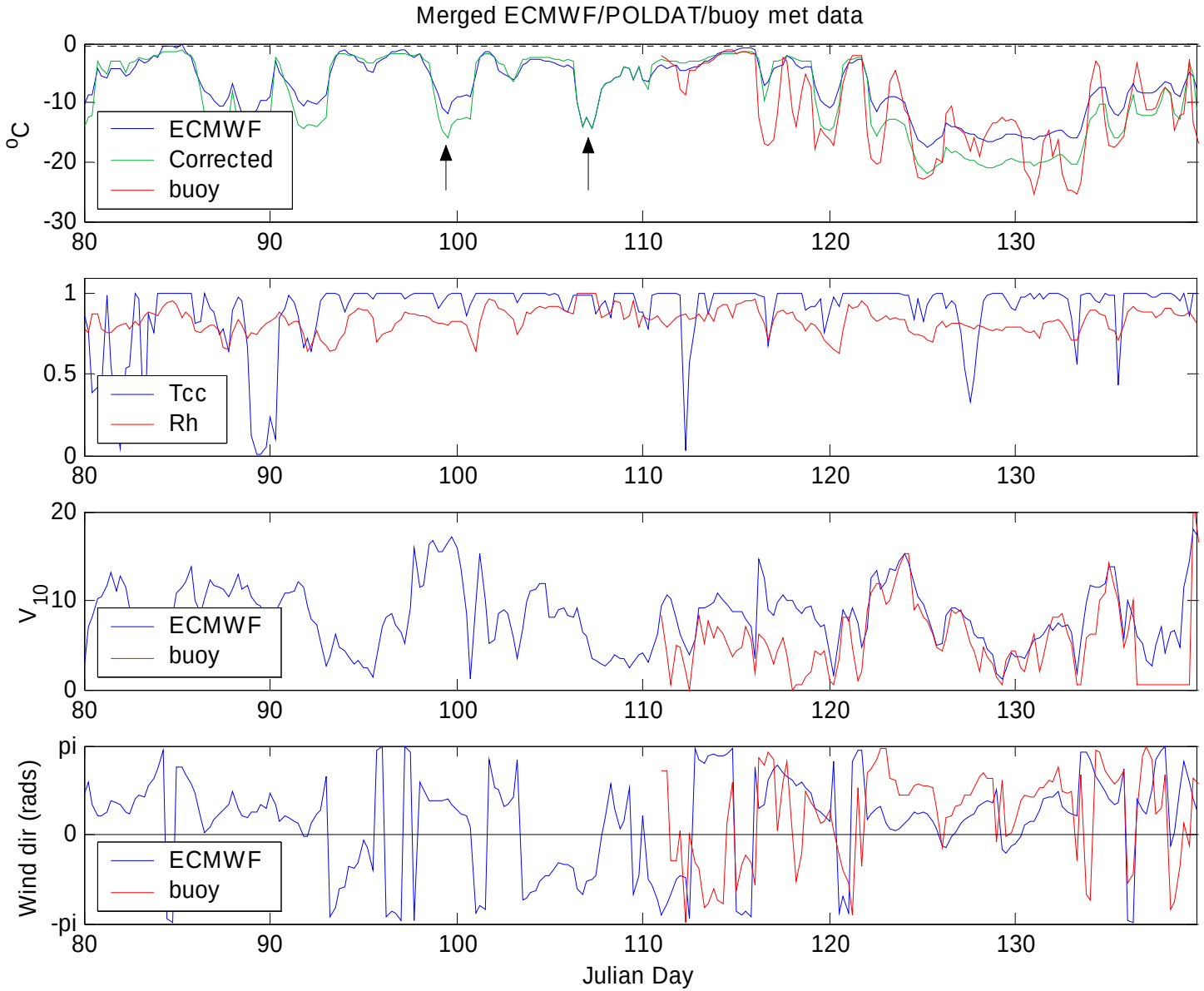

Figure 3.11: ECMWF parameters compared to *in situ* measurements. Top graph shows ECMWF 2 m air temperature (blue), buoy (DML5) 1 m air temperature (red) and the model forcing corrected according to Eq. 3.4-3.6 (green). The ice formation events of interest are indicated by arrows. The second panel plots total cloud cover (Tcc), from ECMWF output and relative humidity (merged ECMWF and ship's data). Bottom two panels show wind speed and direction, for ECMWF and DML5. Buoy data have been scaled and rotated by factors derived in the previous chapter's analysis. The buoy anemometer displays a short freeze-up event at the end of its record.

3.3.1.2 Kinematic model

Momentum transfer parameters were derived from the analysis in the previous chapter, using the two-parameter regression method (Vihma *et al.* 1996). Values used were:

Wind factor = 0.029

Turning angle = 13^{o} (to the left)

Residual current, *u*-component = -0.045 ms^{-1}

Residual current, *v*-component = +0.023 ms^{-1}

3.3.1.3 Thermodynamic model

The thermodynamic model used here is a simple, one-dimensional, flux balance model. Full details of the model are given in Appendix B, with an overview presented here. The model is run twice for each case study – once to determine the sheet ice thickness that would have grown in the absence of turbulence (congelation ice) and once for frazil ice (the maximum possible ice production).

Congelation ice

The thin, young ice considered in the congelation model makes it unnecessary to use complex, snow-covered, multi-layer ice models (Rudels *et al.* 1999). The snow-free assumption is reasonable since no significant snow layer was observed in the area during the experiment. We assume the ice can be approximated by a homogeneous conducting slab; though non-linear profiles have been observed in Weddell Sea ice, these are ascribed to “drastic air temperature excursions” (Eicken 1992) and are a transient feature for ice less than *c*.0.8 m thickness (Maykut 1978), as here.

At the top surface of the ice, the ice temperature depends on the balance of the various fluxes impinging upon it. We first solve for terms that do not depend on that surface temperature, then iteratively solve the balance equation to achieve a zero net flux. If balance cannot be achieved, then the top surface of the ice is melting. The surface temperature is then set to its melting point (around -0.6°C at the observed salinity of 11 psu) and the flux imbalance used to melt ice at the surface. In fact, top melt never

occurred during the study period, with any thickness reductions resulting from bottom melt, at the ice-ocean interface.

At this bottom surface of the ice, growth or melt depends on the balance between the ocean-ice heat flux and the conductive heat flux from the ocean to the ice. This latter term depends on the ice surface temperature, calculated in the previous step. The net heat flux then grows or melts ice depending on its sign. The bottom surface of the ice is assumed to be at the freezing temperature of seawater (T_f = -1.89^{o}C) for the measured mixed-layer salinity (34.35 psu, held constant).

Frazil ice

Frazil ice growth is accomplished using a similar scheme, omitting the conduction terms and setting the surface temperature to the freezing temperature of seawater, since there is no sheet of ice to develop a temperature gradient across. The net ocean-atmosphere flux is used to grow ice, taking the latent heat of fusion given by Markus *et al*. (1998) for ice crystals forming in freezing seawater (234.14 kJ kg^{-1}). This is considerably less than used for congelation ice formation (295.8 kJ kg^{-1}).

For both ice types, the resulting ice growth rate (dh/dt) is multiplied by the time step and added to the existing ice thickness. The model then repeats the process for all time steps until the end of the period of interest. For direct comparison with the model, observed ice thicknesses are converted to their solid ice equivalents. The experiment determined that approximately 30% of the pancake volume was porous space, and observed pancake layer thicknesses are reduced accordingly - multiplying by the volume concentration of ice (V_p = 0.7). Volume concentration of the frazil slicks (V_f) was observed to be 0.4 (Doble *et al.* 2000). Total equivalent ice production must also account for the area fraction of each ice type (f_p, f_f) to conserve ice volume. The final observed solid ice thickness per unit area sea surface is therefore:

$$H_{obs} = h_p V_p f_p + h_f V_f f_f \qquad \text{(Eq. 3.7)}$$

where h_p and h_f are the observed pancake and frazil slick thicknesses, respectively.

The ice thickness is constrained to a minimum value of $1x10^{-5}$ m in order to avoid a "divide by zero" error in the calculation of the conductive heat fluxes. Negative values of ice thickness are similarly avoided by the use of this constraint, though the heat input to the mixed layer that this process would imply is disregarded. The treatment is justified, since the ice formed during our period of interest never melts back to this minimum thickness once growth begins.

3.3.1.4 Validation

The model was first tested against periods of known buoy drift and *in situ* data (*i.e.* after Day 110.0). Layered growth is not considered in this first instance. Buoy motion was well tracked, though the ECMWF forcing significantly under-estimated the amount of ice produced compared to the buoy meteorological data. The empirical correction factor improved results considerably, but since it was devised for this period, we cannot be confident that similar improvements will hold for other times. A summary of the results is given in Table 3.4, below, and example output plots are shown in Figure 3.12.

Table 3.4: Ice thicknesses (cm) from runs of the model particle-tracking and ice growth, using known trajectories and *in situ* data from drifting buoys, for congelation (cong) and frazil ice growth. Thicknesses are given in terms of 'solid ice equivalents' and errors refer to the difference between results using buoy forcing and that extracted from the ECMWF fields, calculated according to Equation 3.7.

Buoy ID	'Raw' ECMWF ice thickness, cm			'Corrected' ECMWF ice thickness, cm			*In situ* forcing ice thickness		Position error, m
	Cong	Frazil	Error	Cong	Frazil	Error	Cong	Frazil	RMS
DML5	7.0	21.3	-38%	9.9	24.8	+6%	9.7	23.9	2150
DML7	6.2	18.1	-82%	8.7	19.9	-30%	11.3	29.1	2687
DML8	6.1	19.1	-67%	7.6	20.9	-34%	10.2	28.8	2327

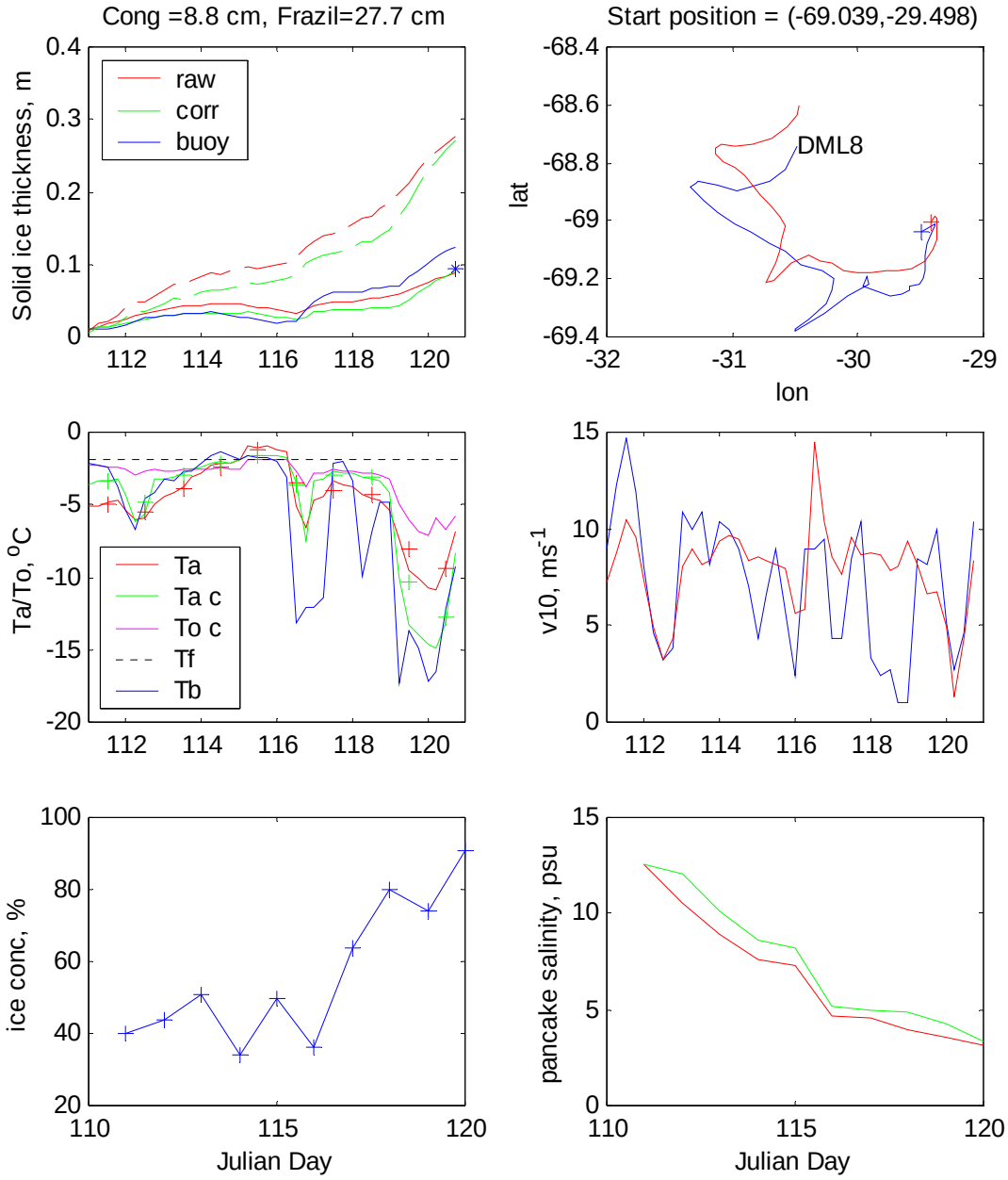

Figure 3.12: Model output, comparing buoy (blue), ECMWF (red) and 'corrected' ECMWF forcing (green). The top left graph shows the evolution of ice thickness for congelation ice (solid) and frazil ice (dashed). Solid ice equivalents are plotted in all cases. Also marked (blue star) is the simple degree-day figure for congelation ice. Real versus backwards-modelled tracks are shown top right. Middle left shows air temperatures at the buoy location from buoy, ECMWF and corrected ECMWF forcing. Also shown are the calculated ice surface temperature (magenta) and the freezing temperature of seawater (black, dashed). Middle right shows 10 m windspeeds from ECMWF and buoy (scaled using the 1m – 10m relation derived in the previous chapter). Also displayed are the ice concentration at the buoy location, derived from DTU SSM/I images, and the evolving pancake salinity, according to the scheme in Wilkinson & Wadhams (2003).

Over a 10 day timescale the buoy tracks gave RMS position errors (between actual buoy and backwards-modelled tracks at the end of the simulation) of approximately 2.5 km. Modelled advection over the period of interest displaced the ice position by only *c*. 40 km. This is of the same order as an ECMWF model grid cell ($1.125^o \times 1.125^o$ or 125×41 km at this latitude) and gives confidence in the forcing extracted along the track.

The calculated congelation ice thickness was also compared with that from a simple degree-day relation (Lebedev 1938), as an external check on the model validity:

$$h = 1.33\left[\sum\left(-T_a - 1.8\right)\right]^{0.58} \qquad \text{(Eq. 3.8)}$$

where T_a is air temperature and the coefficients of 1.33 and 0.58 are derived empirically.

3.3.2 Results

3.3.2.1 Determination of layer growth periods

Modelled fluxes for congelation and frazil ice growth over the period encompassing the two growth events discussed are shown in Figure 3.13. Layered growth is not considered for the moment; graphs are shown simply for homogenous ice at the back-tracked location of station 5 and use the corrected ECMWF forcing data. Turbulent fluxes dominate the energy balance for both types of ice growth, with the sensible heat flux (Q_H) being approximately double the latent heat (Q_E) contribution. The conductive heat flux through the top surface of the congelation ice (Q_C), though larger in magnitude than the turbulent flux (up to 290 Wm^{-2}), is balanced by an almost equal and opposite sign flux across the ocean-ice interface (not shown). Net longwave (Q_{Bnet}) and shortwave (Q_{Snet}) fluxes are small in comparison. The onset of these events is essentially coincident for all six main area stations.

Modelled frazil production indicates positive net fluxes (Q_{net}) corresponding to ice melt only for brief periods around noon between the events. These occur in phase with the downwelling SW radiation (Q_S) when the relatively high air temperatures and low winds result in very small heat loss by the ocean. The conductive heat flux from the ocean to the ice (Q_{CB}) is only slightly negative (*c*.-10 Wm^{-2}) between events and is smaller in magnitude than the oceanic heat flux F_w. Melt therefore occurs on the bottom surface of the modelled congelation ice growth, reducing ice thickness by *c*.1 cm between growth events.

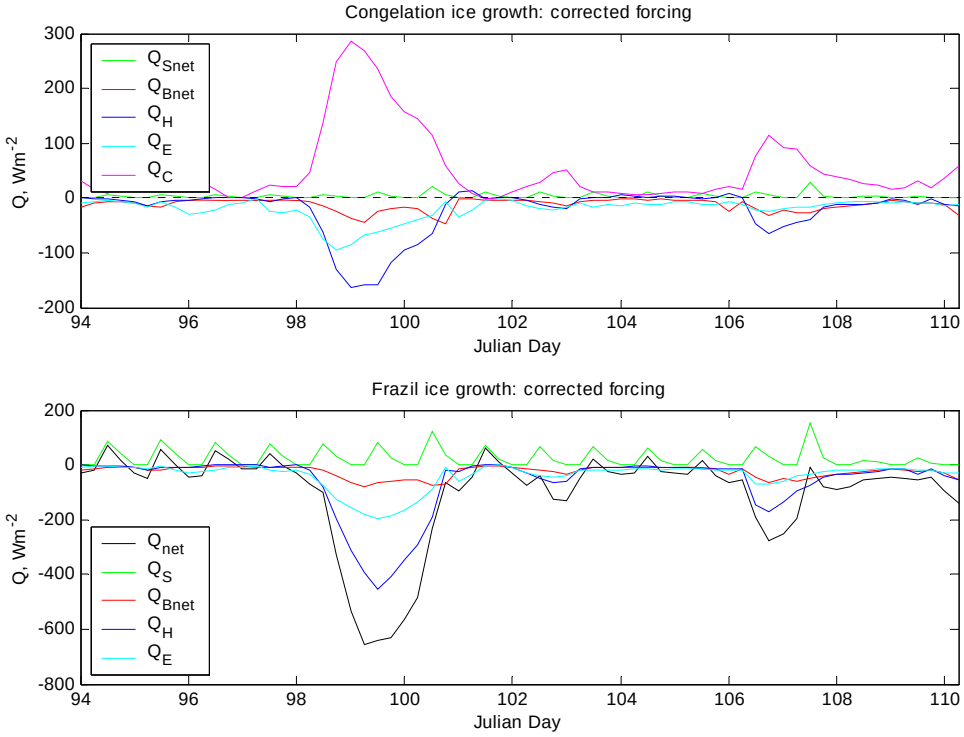

Figure 3.13: Modelled heat fluxes using corrected ECMWF forcing. Fluxes for (a) congelation ice growth and for (b) free-surface frazil growth are shown, both at the back-tracked location of station 5. The distinct ice growth events are clearly shown, with turbulent heat fluxes dominating.

Evolution of ice thickness at the back-tracked location of Station 5 is shown in Figure 3.14.

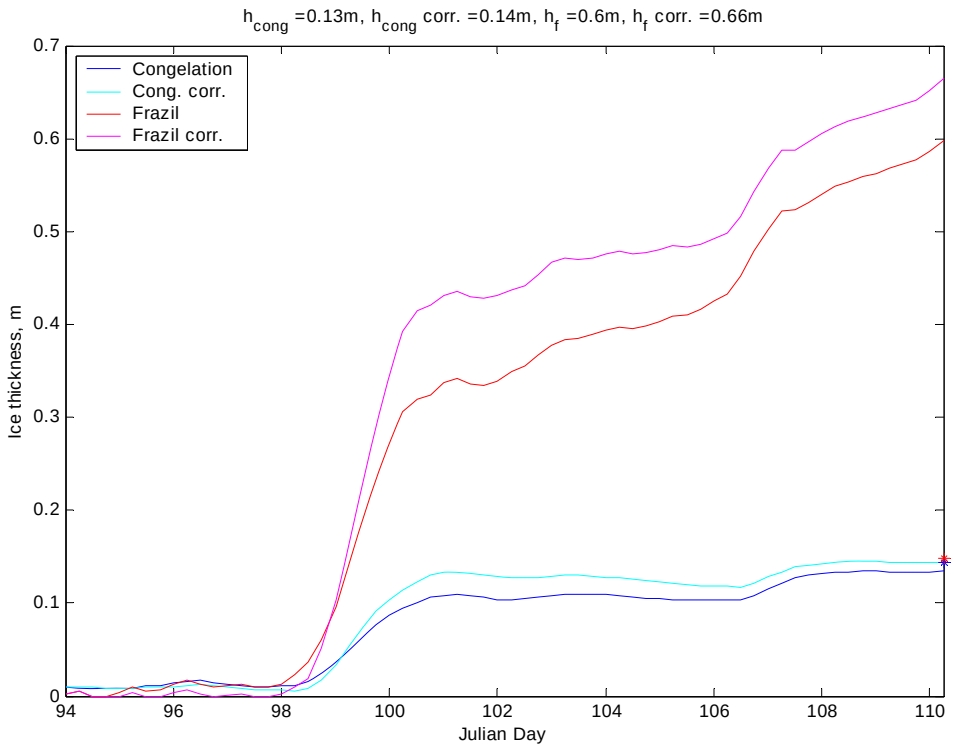

Figure 3.14: Equivalent solid ice thicknesses for congelation (blue: ECMWF forcing, cyan: corrected forcing) and frazil ice (red: ECMWF, magenta: corrected forcing), across the two ice formation events. A slight melting of the congelation ice between events can be seen, which occurs as bottom melt. The red star indicates the value calculated from the degree-day relation, demonstrating just how well tuned this early, empirical model, actually is.

The model is next used to determine the ice growth during each separate "event", or ice growth period, to compare the observed layer thicknesses with the two limiting modelled results (congelation and frazil).

Each "event" is taken to have resulted in the growth of one pancake layer. *Type-A* pancakes were observed to have grown entirely during event 2. Modelled growth of these was therefore begun at the start of Event 2 (day 106) and stopped at the observation time. We assume that the top layers of two-layer types also formed during this latter event. Growth of this layer was begun at the end of Event 1 (day 101.5), however, since a platform for its growth already existed at this time and the presence of

type-B pancakes suggested that top layer growth proceeded soon after the platforms were grown. Bottom layers are taken to have formed during Event 1, and all bottom layer growth was therefore begun at the start of Event 1 and halted at the end of that event, on day 101.5. This was done since the top layer of frazil-grown ice is porous to seawater, resulting in the upper and lower surfaces of the submerged platform being at the same temperature. We have seen that the greatest heat fluxes for congelation ice growth are conductive and sensible and both of these will be zero for the submerged ice platform. Duration of modelled growth periods is shown in Figure 3.15 for clarity.

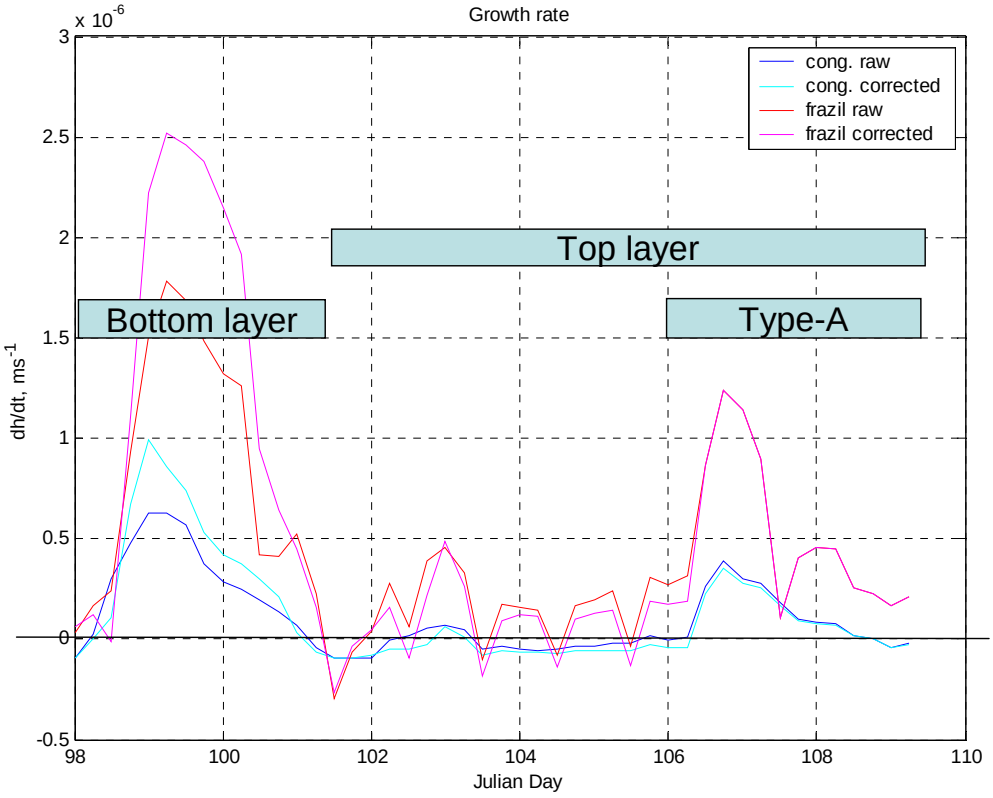

Figure 3.15: Duration of modelled growth periods overlaid on the calculated ice formation rates (dh/dt, m s^{-1}).

3.3.2.2 Event 2

The simulation was first run for the most recent growth period, for all main-area stations. The long-scale station 6 was omitted from these calculations since a third frazil formation event was underway there before observations were taken. Figure 3.16 shows

the modelled solid ice equivalent thickness for congelation and frazil growth, with the observed mean layer thicknesses at each station marked. Observed thicknesses are corrected for volume concentration and area according to equation (3.7). Error bars indicate the standard deviation of observed ice cover thickness. Corrected modelled thickness is less than the 'raw' figure due to the five days of relatively high air temperatures after Event 1, and the resulting positive temperature correction.

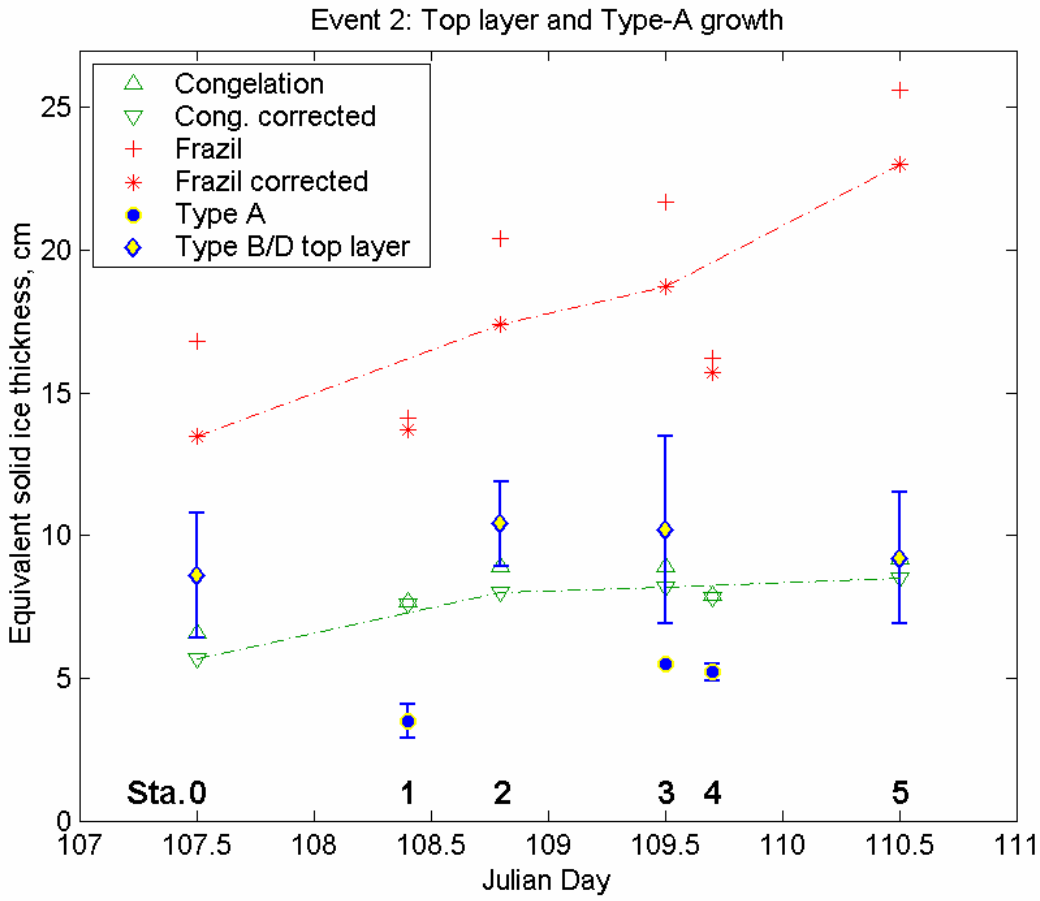

Figure 3.16: Modelled and observed ice thickness for Event 2 (i.e. single layer pancakes and top layers). Observed ice thickness at each ice station is plotted together with the corresponding modelled thickness for congelation and frazil ice growth at that observation time. Mean equivalent layer thicknesses are plotted, with error bars indicating their standard deviation. The modelled congelation and frazil ice growth which would have occurred under the same forcing is indicated both for 'raw' and corrected forcing. Corrected forcing results are also linked by dash-dotted lines. Station numbers (*Sta.*) corresponding to each observation are shown above the *x*-axis.

The ice cover observed at the three '*type-A*' stations (1, 3 & 4: *Type-A* pancakes plus frazil) has equivalent solid ice thicknesses (3.5±0.6 cm, 5.5 cm, 5.2±0.3 cm respectively) significantly less than even the congelation ice growth value. Mean thicknesses of the top layers lie significantly above the congelation ice equivalent, however, with the upper range of observed values reaching approximately double the congelation ice figure or half the maximum physically-possible value.

3.3.2.3 Event 1

Results for bottom-layer growth are shown in Figure 3.17. Corrected modelled growth in this case is higher than the uncorrected results, due to significantly colder corrected air temperatures during the formation event. The area fraction for pancakes grown during this event is assumed equal to that seen at the end of Event 2, neglecting *type-A* pancake formation in the interstices and the slightly larger diameter of the top layers. We do not include any contribution from the frazil ice remaining in the interstices between pancakes since it could not be directly measured. Thickness for *type-D* bottom layers is not adjusted for porosity (since they are columnar, not granular ice) or area, since they formed in large areas of calm water identical to that considered for the modelled congelation ice growth.

Observed thickness of *type-D* platforms is much higher than modelled growth, implying that these were formed earlier and advected into the area. It would actually require 250 degree-days to grow the mean 33 cm columnar ice layer observed at station 0: both events combined constitute only 44 degree-days, equivalent to 12 cm ice growth.

The *type-B* lower layers grown during this event are analogous to the *type-A* pancakes seen after Event 2. They demonstrate similar low growth rates, with their equivalent solid ice thickness plotting well below that of the modelled congelation ice at stations 0, 3 and 5, and support the surprisingly slow *type-A* growth seen during Event 2.

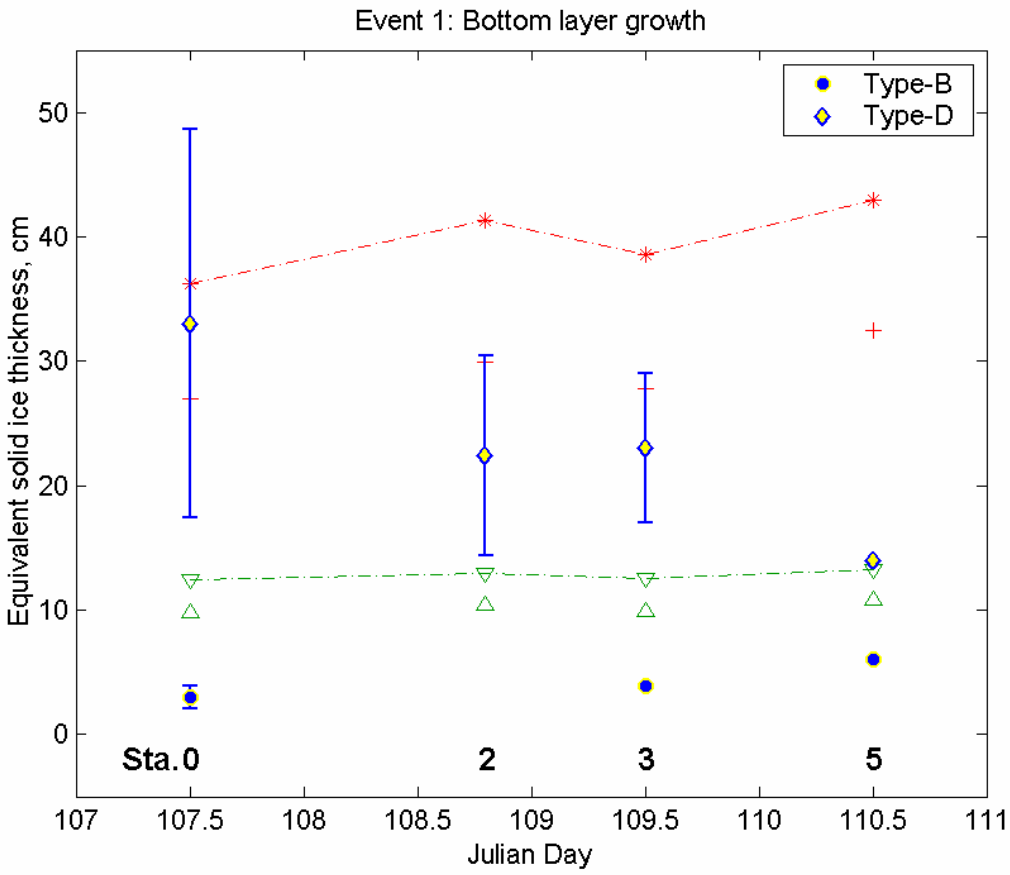

Figure 3.17: Modelled and observed ice thickness for Event 1 (bottom layer growth)

3.3.2.4 Combined growth

The disparate rates of formation ascribed to the two processes combine to produce a two-layer pancake whose overall rate of thickness increase must lie between that of each layer. This 'overall growth rate' is perhaps the most important parameter, since it is the overall thickness of the pancake which determines the fluxes across the ocean-air interface and the mass of salt rejected to the mixed layer.

We therefore model growth beginning at the start of Event 1 and continuing to the observation time. Results are presented in Figure 3.18. Equivalent thicknesses are presented only for *type-B* pancakes, since they are the only two-layer, frazil-grown pancakes considered here. Results match the congelation ice equivalents closely, though

actual pancake thickness (*i.e.* not corrected for volume or area) is approximately double the congelation equivalent.

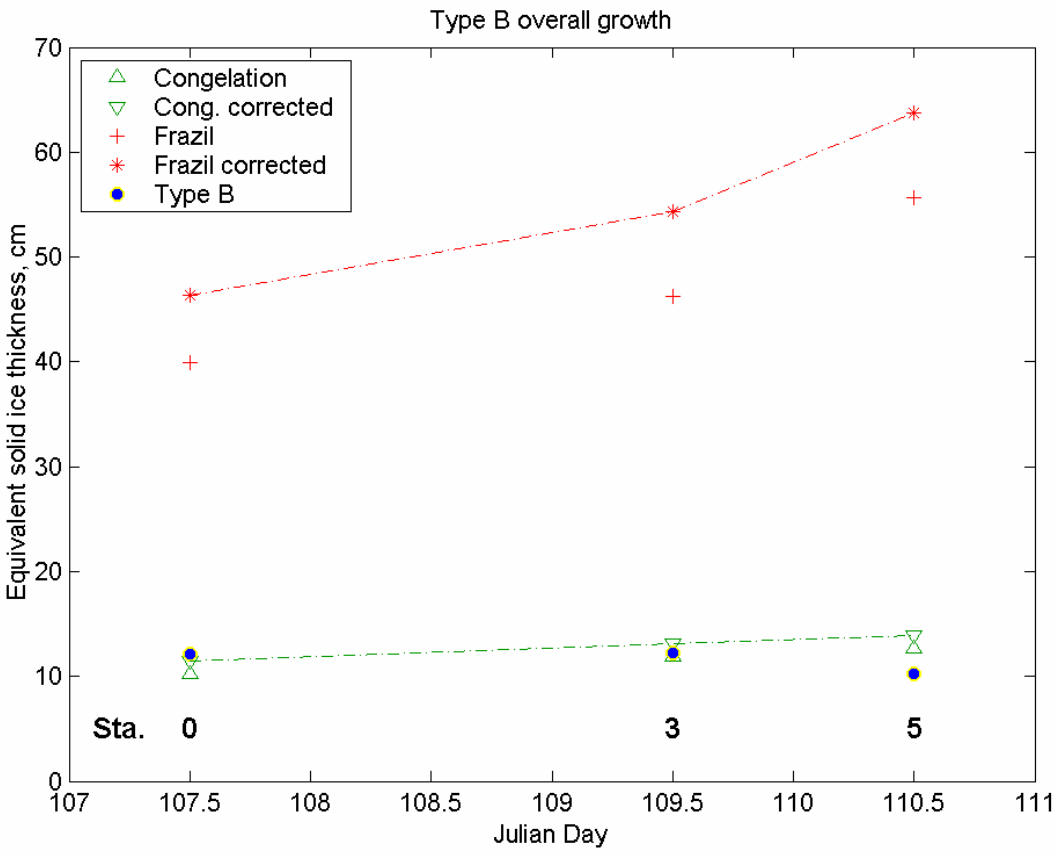

Figure 3.18: Modelled and observed ice thickness for Type-B pancakes (two frazil layers) formed across both events.

3.3.2.5 Sensitivity tests

The model's response to variations in forcing parameters was tested. Results are summarised in Table 3.5. The table shows modelled growth at the back-tracked location of station 3, beginning at the start of Event 1 and continuing until the observation time. Oceanic heat flux influences ice production by approximately half the proportion of the change in that parameter (e.g. a reduction of 60% in F_w increases congelation ice

thickness by 30%). A fixed cloud cover fraction shows the model to be relatively insensitive to this parameter, since cloud has two opposing effects; cutting down incident solar radiation but increasing downwelling longwave radiation through increased effective emissivity of the air. Given the relatively advanced season and short daylight hours, it is the longwave effect which dominates, increasing ice growth with reduced cloud cover. Relative humidity affects the latent heat flux, which has a small contribution to the overall flux balance and is reflected in the minor response of the model.

Table 3.5: Sensitivity of the model to changes in forcing parameters. Figures in the 'variation' column show the minimum-normal-maximum values through which the parameter was varied, if held constant, or the offset from the varying value. Changes are expressed as percentages of the final uncorrected ice thickness for congelation ice (h_c) and frazil ice (h_f) growth modes. Growth was modelled at the back-tracked location of station 3, beginning at the start of event 1 and continuing to the observation time.

Parameter	Variation	h_c error, %	h_f error, %
Cloud fraction, T_{cc}	0.6 – var - 1	+24 / -3	+31 / -3
Relative humidity, Rh	80 – var - 95	+3 / -1	+5 / - 8
Oceanic heat flux, F_w	10 – 25 - 40	+30 / -26	-
Air temperature, T_a	±1°C	-21 / +19	-25 / +25
Wind speed, v_{10}	±2 ms^{-1}	+7 / -12	+19 / -20

The model is considerably more sensitive to changes in air temperature and windspeed, however, with the magnitude of the response being broadly equivalent to the percentage change in the parameter. The parameters dominate the equations for the turbulent fluxes, which themselves dominate heat exchange across the ocean-ice-atmosphere boundaries. ECMWF windspeeds have been found to be accurate (Section 2.5.1), but

the disparity between ECMWF and *in situ* air temperatures is more marked. Application of the empirical correction factors has been found to increase the accuracy of the ECMWF results significantly, however, though calculated ice thickness can still be under-estimated by up to 30% (see Table 3.4).

The final thickness that a congelation ice cover can achieve (the equilibrium thickness) was also investigated, varying the oceanic heat flux and downwelling shortwave radiation. Results are shown in Figure 3.19, plotted as the change in ice thickness in a given time step for various starting ice thicknesses.

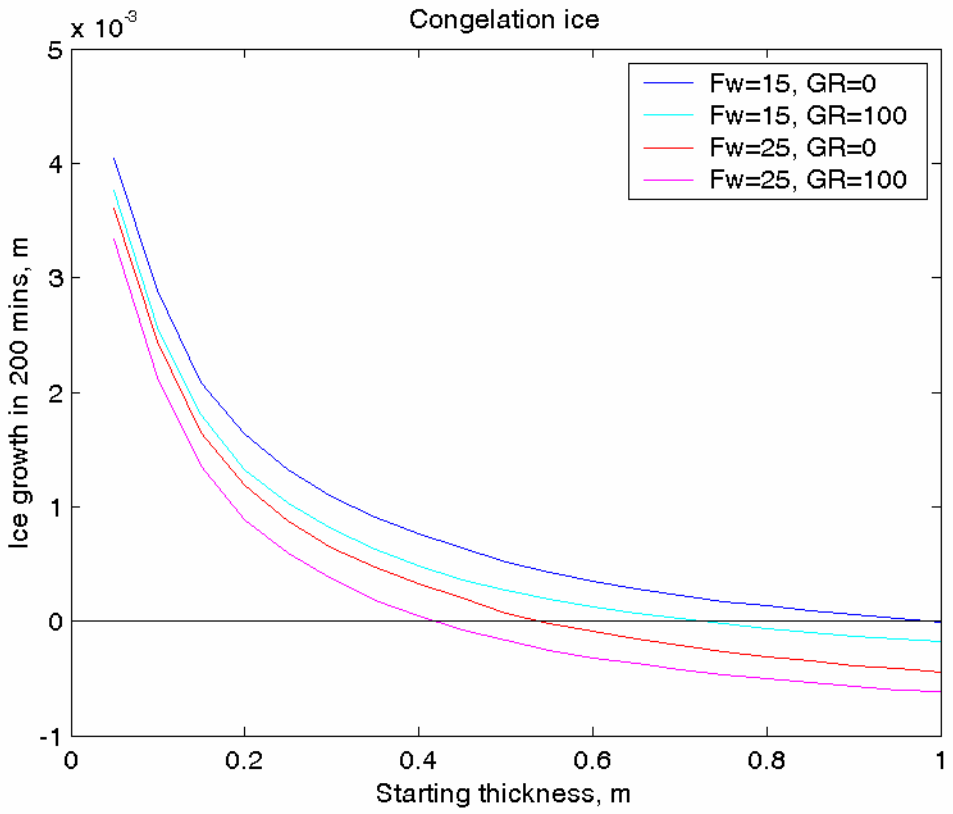

Figure 3.19: The effect of varying oceanic heat flux (F_w, W m^{-2}) and downwelling shortwave variation (GR, W m^{-2}) on the equilibrium thickness of a congelation ice sheet. Thickness increase in a given time step (here, 200 minutes) is plotted against starting ice thickness in the simulation. A negative growth rate indicates that the ice sheet has exceeded its thermodynamic limit for those conditions.

A negative growth indicates that the ice sheet is thicker than its thermodynamic limit for the given conditions. Varying the oceanic heat flux from 15 – 25 W m^{-2} changes the equilibrium thickness from 72 cm to 40 cm for a fixed downwelling shortwave flux of 100 W m^{-2}. With Austral winter conditions (24 hour darkness), the same change in oceanic heat flux changes equilibrium thickness from 1 m to 55 cm. While not directly applicable to the above simulations, which never achieve solid ice equivalent thicknesses of this level, the exercise does serve to indicate the pivotal role of oceanic heat flux in controlling the overall ice thickness in the Weddell Sea.

3.3.2.6 Growth Rates

Published work on frazil ice growth usually quotes the growth rate in terms of kilograms of ice per square metre of sea surface per hour (or second). This implies a constant forcing over the period of interest, in terms of the net heat flux and turbulence levels which together control ice production in this regime. While often valid for laboratory experiments, this constant flux assumption is clearly not valid in the field. The relative ice production for congelation, frazil and observed cases can be examined in terms of this rate, however, and it is interesting to do so, in order to allow comparison with previous work.

Ice production is therefore re-calculated as rates for the two events and combined ice growth, in an equivalent manner as for Sections 3.3.2.2-4. Figure 3.20 reproduces the ice thicknesses originally plotted in Figure 3.16, converted to solid ice production rates according to the formula:

$$Rate = h.\rho_i / \Delta t \qquad \text{(Eq. 3.9)}$$

Where h is the relevant ice thickness (SIE, m), ρ_i is the pure ice density (920 kg m^{-3}) and Δt is the duration of the event (seconds). Event 2 is considered to last from day 106.0 to 108.0: Δt is thus 172,800 s for all points except Station 0, which was measured

before the end of the event and whose Δt is adjusted accordingly. The lines plotted represent the least-squares fit to each mechanism's rates.

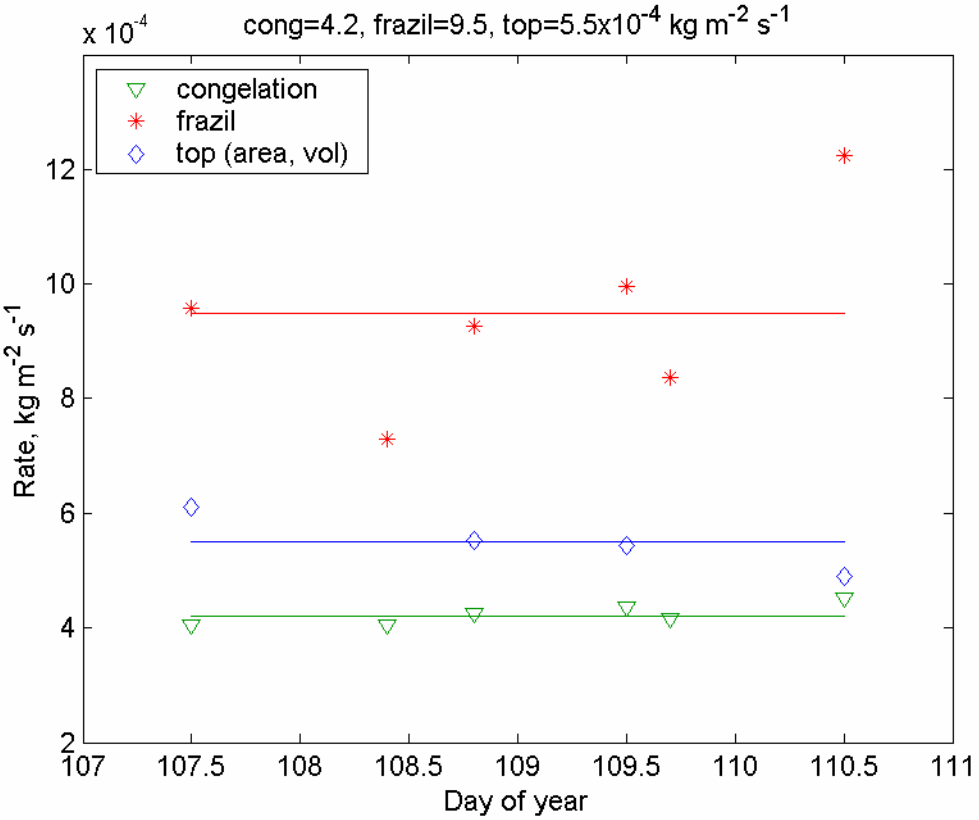

Figure 3.20: Pancake top layer (SIE) growth rates at the four stations where these types were found, compared to modelled frazil and congelation ice growth rates during Event 2. Lines indicate the least-squares fit. Top layer rates are plotted correcting for volume and area fraction at each station.

Growth rates for both events and for the overall (combined) growth are summarised in Table 3.6 and the top layer growth rate once again stands out as being significantly greater than bottom layer (accretion) growth, at 5.5×10^{-4} kg m^{-2} s^{-1}.

Table 3.6: Ice growth rates (SIE) calculated according to Equation 3.8, for modelled congelation and frazil growth in the two events, and for the observed ice production (pancakes + frazil, corrected for volume fractions and area fractions).

$\times 10^{-4}$ kg m^{-2} s^{-1}		Modelled Congelation	Modelled Frazil	Observed
Event 1	Bottom	3.9	12.0	2.0
Event 2	Top	4.2	9.5	5.5
	Bottom			2.5
Combined	Both	2.2	9.7	2.0

3.3.3 Discussion

The solid ice equivalent thickness of the *type-A* and lower layer *type-B* pancakes is unexpectedly low, given previous conjecture about pancake formation rates (Wadhams *et al.* 1987; Hopkins and Shen 2001). A clear disparity in ice growth rates exists between *type-A* pancakes and the *type-B*/*D* top layers, however. The consistency of rates for a given mechanism (accretion or scavenging) and the disparity between these mechanisms gives confidence that separate and disparate processes are occurring as stated, however.

The disparity becomes more marked if we consider that top layer growth occurred with the existing platforms (from Event 1) significantly reducing the area of sea surface available for ice production during the second event. These bottom layers must have occupied a similar area fraction at the beginning of Event 2 to that seen at its end, implying that only *c*.40% of the total area was available for frazil production during this event.

An opposing consideration is the fate of the frazil fraction remaining at the end of Event 1. The transient nature of the positive heat flux episodes indicates that significant melt did not occur and the lack of granular ice underneath the *type-D* congelation ice

suggests that the frazil did not accrete below the platforms in the five days between events. The frazil layer was also never observed to extend deeper than the pancakes during ROV flights, though these were conducted in conditions of low turbulence. It must therefore either have remained as frazil ice (increasing the thickness of the frazil slick observed at the end of Event 2) or have accreted to the top surface of the platforms, adding to the perceived top layer production during Event 2. Either process would contribute additional volume to the ice formed during Event 2 and require a downward correction in the equivalent solid ice thickness due to that event.

The balance of these opposing corrections is unknown in the absence of comprehensive field or ice tank observations over similar periods. It is probable that an upwards correction in rate due to the pancakes occupying their existing areal fraction will dominate, since the contribution from remaining frazil is reduced by $V_f = 0.4$ and the smaller area fraction of this ice type. The true equivalent top layer thickness is therefore likely to be higher than Figure 3.16 indicates. Consideration of the overall growth removes the need for the effective area and Event 1 frazil corrections and gives a more reliable comparison to congelation and frazil equivalent thickness.

It seems unlikely that classical (accretion) pancake growth proceeds at a rate below that of congelation ice (2.0 *versus* 2.2×10^{-4} kg m^{-2} s^{-1}), however, and this unexpectedly-low rate may arise from errors induced by the many assumptions required.

Foremost amongst these is the assumption that the sea surface was ‘ready to freeze’ at the onset of Event 1. If this was not the case, then a considerable fraction of the Event 1 cooling may have been required before frazil formation could begin and formation rates of classical pancakes would then increase significantly. Supporting the assumption, it is noted that the ECMWF data show an extended period of low temperatures (-15°C) five days prior to the onset of Event 1. It is suggested that this period pre-conditioned the surface water for frazil formation, since temperatures did not rise to above the freezing point of water in the intervening period. The frazil formed during Event 1 was observed to be relatively new (as demonstrated by the lack of pancakes and its salinity),

confirming that frazil/pancake formation from this previous event did not occur: a situation which would otherwise cause a downward revision in the Event 1 rates.

The period between events, when ocean-atmosphere fluxes are almost zero and the oceanic heat flux becomes significant, is another possible source of this error. Higher air temperatures than the ECMWF temperature data suggest, or higher values of oceanic heat flux than assumed, might lead to significant melting of the frazil or pancake ice during this finely-balanced period. If melt occurs, ice production during the first event would be significantly under-represented. The sea surface temperature would also become elevated to the north of the ice edge, requiring the re-establishment of a freezing surface layer before frazil and pancake production could begin during the second event. The same error in forcing would thus lead to a consistent error in pancake growth rates for the classical mechanism, as seen. A similar effect would also apply to upper layer growth, however, since frazil production during this process will also be delayed until an appropriate sea surface temperature is regained. The disparity between the formation rates arising from the two mechanisms therefore remains a robust conclusion.

It should also be borne in mind that the new pancakes studied are rather thin in comparison with a typical final pancake thickness of *c*.50 cm. Further thickness increases will be dominated by the top growth process, increasing the overall rate towards that of the faster mechanism. Equivalent congelation ice growth is also greatly reduced once the ice cover begins to thicken to these levels, thus pancake and congelation ice growth rates can be expected to diverge more significantly in the latter stages of the pancakes' evolution.

We note that the *type-A* pancakes sampled here were strong compared with those seen in the Odden in 1997 – none were broken during removal from the lifter, even when they were only 5 cm thick. This arises due to the lower air temperature events here compared to the Odden area, and suggests that only a short time need elapse before frazil-rafting can begin. The overtopping mechanism may therefore be extremely common in the Antarctic, though the absence of the obvious *type-D* pancakes has

allowed the two layer types to remain undetected until now. *Type-D* pancakes may be unusual and confined to an 'oscillating' ice edge, which allows the juxtaposition of low freeboard congelation ice and frazil growth. The disparity in growth rates between the two mechanisms (5.5 *versus* 2.2×10^{-4} kg m^{-2} s^{-1}) suggests that top layer growth will dominate pancake ice accretion where it occurs.

The lack of two layer pancakes seen in the Odden may be due to the surface melt conditions common in that region. Surface melt flushing would tend to remove the signature of top layer growth in pancakes which have experienced higher air temperatures for any length of time. A cruise to the region in March 2001 encountered pancakes which had not experienced a melt flushing event, however (Doble, unpublished data). These consistently displayed similar salinity profiles to the Weddell Sea pancakes, suggesting that the top growth process may dominate there too.

The modelled frazil ice production is a theoretical maximum and assumes that the presence of frazil ice crystals at the sea surface does not reduce the ocean-atmosphere heat flux. This assumption is based on the low volume concentration of the frazil slick ($\leq$0.4) which may be effectively 'transparent' to heat exchange. Tank measurements suggest that the rate may be reduced, however: Smedsrud (2001) obtained a rate of 3×10^{-4} kg m^{-2} s^{-1} during experiments at the Hamburg HSVA facility where the net heat flux to the atmosphere was estimated as 257 W m^{-2}. This compares with the modelled frazil production rate here of 9.5×10^{-4} kg m^{-2} s^{-1} during Event 2, with a similar net heat flux.

The two rates may not be directly comparable, however, since the growth of frazil ice is limited by heat transfer away from the growing crystal, specifically by a parameter termed the Nusselt number (*Nu*), which is the ratio between the actual (turbulent) heat transfer and that which would occur by conduction alone (Holland *et al.* 2007). Estimation of *Nu* is far from straightforward, requiring knowledge of micro-scale parameters such as the turbulent dissipation rate and the turbulence intensity of the fluid, as expressed by the Prandtl number and the Kolmogorov length scale. Indeed, a series of papers have appeared which mis-parameterise the choice of *Nu*, following an

initial mistake by Hammar and Shen (1995) and frazil production was subsequently over-estimated by factors typically 10-100 (Holland *et al.* 2007). Turbulence levels in the HSVA tank are rather low in comparison with real field conditions. Frazil ice formation there proceeds to form an almost 100% ice cover consisting of rectilinear pancakes, which extend across the whole width of the tank and directly abut one-another in an articulated fashion (pers. obs.), as shown in Figure 3.21. This is rather unlike the outcome in the field and demonstrates the relatively low level of turbulence generated.

Other rate estimates include those for a 500 m wide polynya (Bauer and Martin 1983), at 8.6×10^{-4} kg m^{-2} s^{-1} for a net heat flux of 290 W m^{-2} (10m/s wind at –10^{o}C), to 58×10^{-4} kg m^{-2} s^{-1} with a net heat flux of 1950 W m^{-2} (30m/s at –40^{o}C).

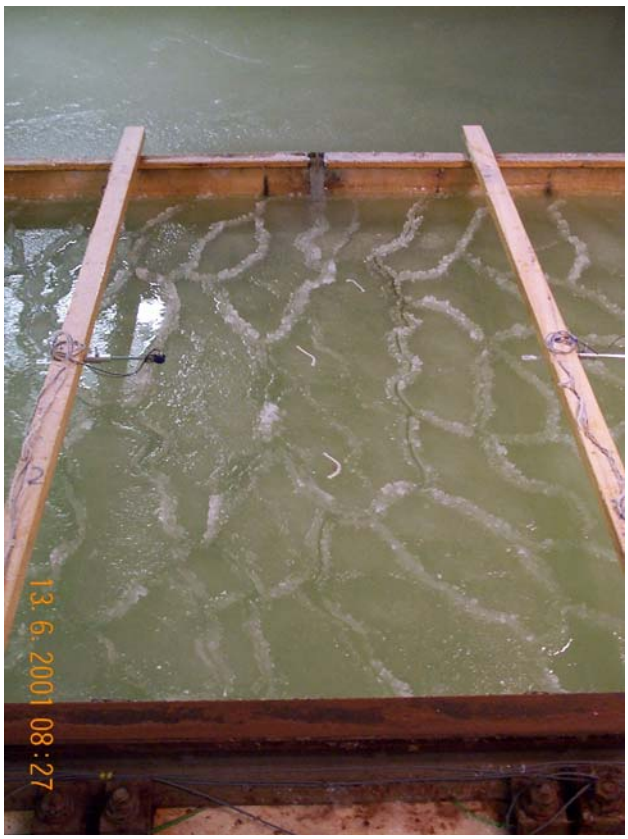

Figure 3.21: 'Pancake' ice cover generated in the HSVA wave tank during the INTERICE III experiment, demonstrating the relatively low levels of turbulence encountered there compared to the field.

Ultimately the absolute rate of frazil production in a free surface situation serves to give a comparison (and upper limit) with the observed ice production during pancake growth, and inaccuracies in its value do not impact the absolute rate calculated for the observed ice cover. The frazil-relative rate does provide a more robust quantification than the congelation-relative rate, however, since this latter figure will vary as the congelation ice growth rate slows with increasing ice thickness. Field measurements to determine the effect of a significant frazil slick thickness on ocean-atmosphere heat exchange are required to better constrain the frazil ice production. This is far from being an easy measurement to make practically, however, given the high wind and wave states implied and the concomitant sampling difficulties. Tank measurements cannot provide realistic wave periods or amplitudes to ensure the frazil-seawater mixing processes are correctly simulated, however, since the frazil crystals are life-sized while the waves are not. Discrete numerical simulations perhaps offer the best way forward in this respect.

Results from this chapter were published as Doble *et al.* (2003). The paper is included as Appendix D to this thesis.

3.4 Summary

The chapter describes *in situ* measurements of pancake and frazil ice at seven stations across the experimental area. Ice area fraction, thickness, salinity, porosity (volume fraction) and morphology are discussed.

Two layers, with disparate salinities and porosities are identified in all the mature pancakes examined and the pancakes are classified into six types accordingly. Growth of bottom layers is attributed to classical accretion of the frazil slick, while it is suggested that top layers are dominantly grown by rafting of frazil crystals onto the top surface of existing pancakes or congelation ice fragments. Salinity and porosity data are used to support this hypothesis, together with direct observations in the HSVA ice tank.

The time period when each layer was formed is identified with reference to two distinct cold air outbreaks in the meteorological record. The backwards trajectory of the observed ice is established with reference to the wind factor and turning angle calculated in the previous chapter, and the meteorological forcing extracted along this track.

The forcing is then used as input to a one-dimensional flux balance model, to simulate ice growth during the formation of the two layers. Observed ice thickness is compared to that which would have occurred under calm conditions (a minimum figure) and to the ice production for frazil ice growth alone. This latter case provides a maximum figure, since it assumes that the presence of a frazil slick does not reduce the ocean-atmosphere heat flux.

Calculated growth rates were markedly different for bottom and top layer growth, reflecting the disparate mechanisms at work. Ice production during the accretion of classical pancakes was found to be similar to that of thin congelation ice. The ice production during top layer formation was approximately double the bottom layer value and half the maximum simulated figure from frazil growth.

CHAPTER 4: THE CONTRIBUTION OF HF MOTION TO ICE GROWTH

Growth rates of pancake ice have been examined and it has been determined that high-frequency motion plays a significant role in the pancakes' movement. These findings are next combined to determine the influence of that high-frequency motion on ice formation in the pancake zone: does the observed high-frequency motion have a significant impact on ice production? How the particular characteristics of the pancake/frazil mixture influence the volume of ice produced is examined, by comparing ice production to that of a congelation ice cover undergoing the same differential motion.

4.1 Introduction

Oscillating divergence-convergence events (the "ice accordion") are known to play a significant role in increasing ice production as part of congelation ice growth. The thin skim of ice formed in open water patches is deformed to a significant thickness during convergence, re-exposing open water during the divergent part of the cycle. Figure 4.1 illustrates the effect for fixed meteorological forcing (T_a = -10°C, v_{10} = 5 ms^{-1}). The blue curve shows the evolving ice thickness for an undisturbed ice sheet, where the increasing ice thickness progressively insulates the ocean from the cold atmosphere, gradually slowing ice growth. The red line applies the open-water growth rate (dh/dt) at all timesteps, simulating the removal of the thin skim of ice by convergent crushing before the open water area is re-established by the ensuing divergence. Over the two days illustrated, the latter case produces nearly twice as much ice as the undisturbed ice sheet.

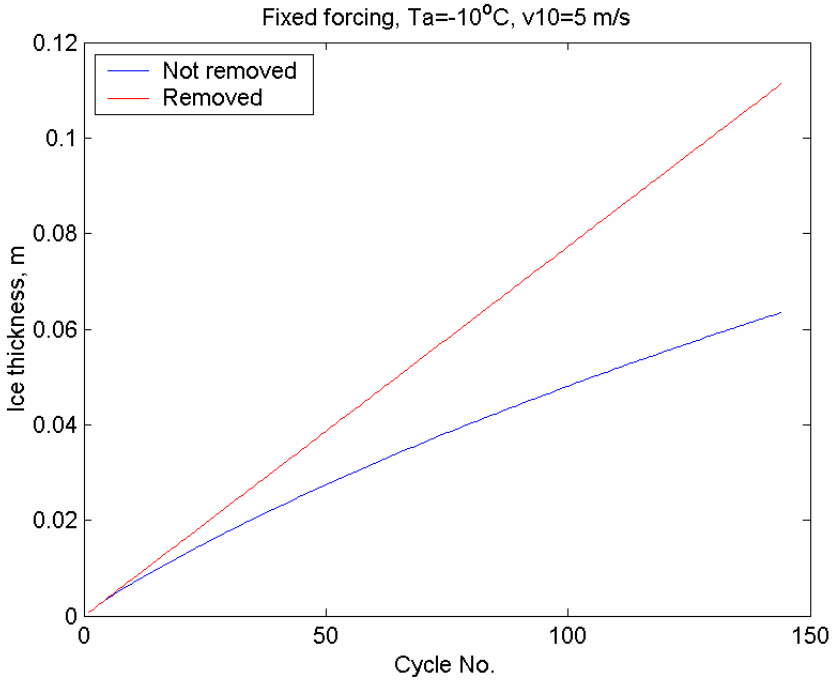

Figure 4.1: Congelation ice growth with fixed meteorological forcing, illustrating the effect of the *ice accordion*. The blue curve shows the thickness evolution of undisturbed ice, which slows as the ice cover thickens, while the red curve maintains the open-water growth rate throughout. The graph shows 144 cycles, equating to two days.

The role of convergence-divergence is less clear for a frazil-pancake mixture, however, where the frazil area produces ice at close to the open water value in any case. In the absence of platforms which the frazil can overtop (and hence remove frazil from the slick), oscillating divergent-convergent cycles would serve only to temporarily thin and thicken the frazil slick, since a frazil ice suspension of any significant thickness would relax to occupy the positively divergent area.

It was seen in the previous chapter that the presence of pancakes, in their role as accretion platforms for the frazil, play an important role in removing frazil from the slick and building the pancake thickness towards its final (consolidation) value. Without this continual removal of frazil crystals, the slick would eventually become so thick that the buoyancy of the submerged crystals would lift the surface crystals out of the water, severely limiting heat fluxes across the ocean-atmosphere interface. This was not observed in the Weddell Sea, even at the inner stations where consolidation occurred very quickly afterwards. It does occur in the Greenland Sea, however: Figure 4.2 shows such a frazil slick in the Odden in March 2001. It is suggested that this only occurs in the Odden, since the ice tongue there never becomes sufficiently wide to damp out the considerable wave energy of the winter Greenland Sea. Rather than the ice tongue growing laterally, pancakes are instead advected southwards to melt in the warmer waters south of Jan Mayen island (Wilkinson and Wadhams 2003) . Frazil production thus continues in the Odden without consolidation occurring. In the Weddell Sea, however, the freezing surface continues to advance northwards, widening the frazil-pancake zone and damping wave energy sufficiently to allow consolidation to occur long before frazil production of this magnitude has taken place.

The formation of pancakes does not appear to increase overall ice production, since the area of the sea surface that they occupy is no longer available for frazil ice formation. The role of the pancakes in controlling overall ice volume production is a balance between removing frazil crystals from the slick, continuing the very strong heat exchange between the ocean and the atmosphere (positive, termed ‘scavenging’ from hereon), and occupying otherwise frazil-producing area through their lateral growth (negative).

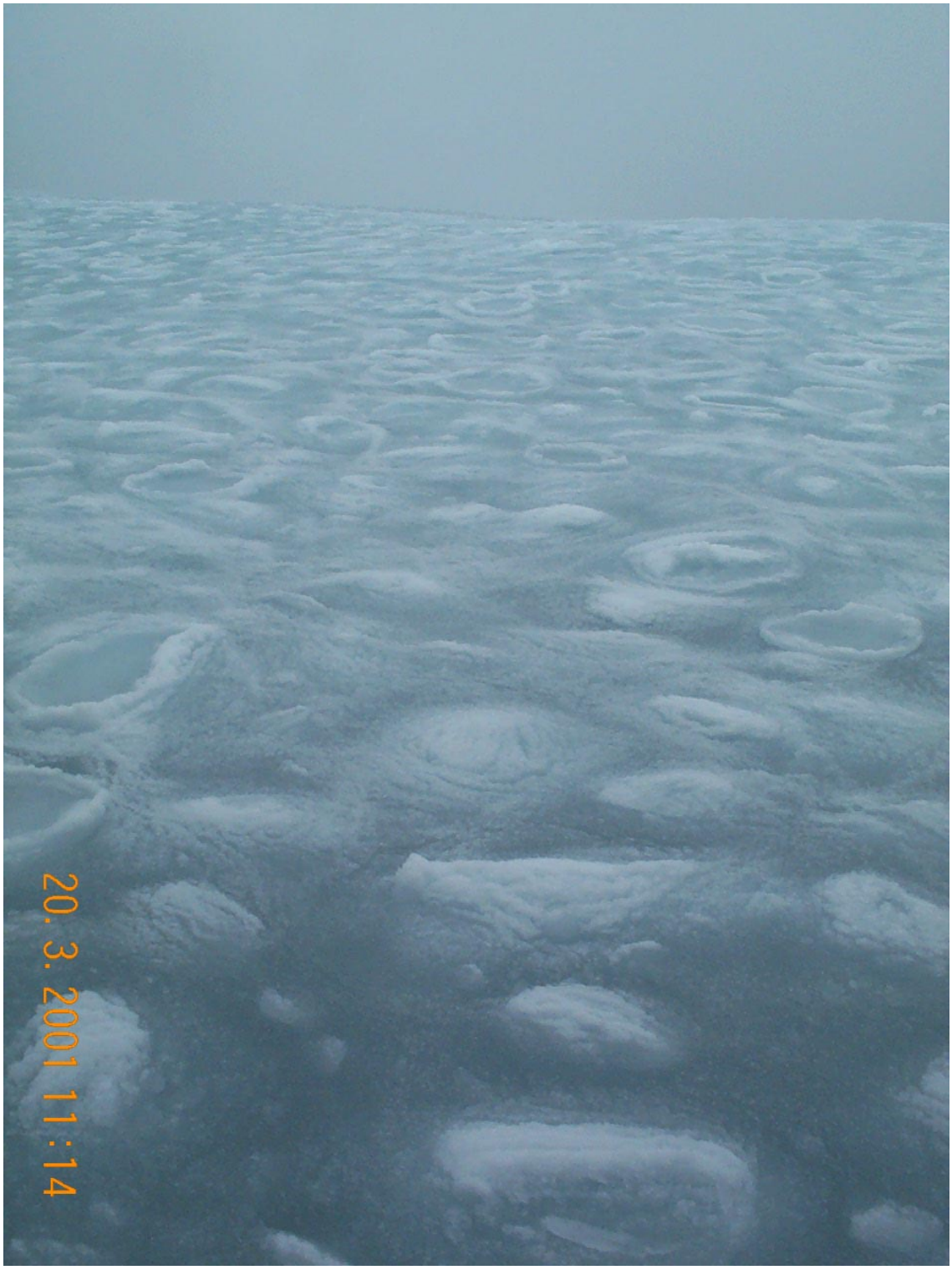

Figure 4.2: A very dense frazil slick observed in the Odden (Greenland Sea) during a cruise aboard *R/V Jan Mayen* by the author as part of the CONVECTION project. The frazil slick has become so thick that the topmost crystals have been lifted out of the water, draining to appear white in the image. The large pancakes in this image are approximately 2 m diameter. Large amplitude swell waves (6 m) can be seen propagating through the mixture (see horizon).

The role of this former, frazil scavenging, process is examined using the observed pancake top layer growth, observed buoy motions and modelled frazil ice production. Only top layer growth is considered, since the previous chapter's analysis showed that its rate was significantly greater than the lower layer accretion process and this is expected to begin immediately after the creation of initial platforms, dominating subsequent ice production in the pancake cycle. The simple conceptual framework used in this chapter makes the following assumptions:

1. *The thickening of the pancakes' top layers only occurs by frazil scavenging due to their translation through the frazil slick.* In fact it is expected that frazil scavenging also occurs as the pancakes tip in the wavefield and scoop frazil onto their top surfaces, but this does not present an objection given the phenomenological nature of the parameterisation
2. *Pancakes actually 'travel through' the frazil ice surrounding them during their displacement, rather than the whole frazil-pancake matrix translating together*. Observations suggest this is only partly true and this also contributes to the phenomenological nature of the parameterisation
3. *The area occupied by the pancakes does not contribute to ice production*. This consideration was irrelevant when examining the relative growth rates in the previous chapter, but is central to the model here in that ice production only occurs in the interstitial frazil slick
4. Concomitantly, *lateral growth of the pancakes, and hence reduction of area available for frazil production, is ignored*. Observations suggest that this assumption is robust, since the area fraction of pancakes does not grow as they mature: pancake area fractions were similar at all stations and did not appear to be a function of pancake diameter, thickness or proximity to the consolidation boundary (see Table 3.1)
5. *The 20 minute interval data captures all the pancake movement and no higher-frequency motions exist*. This is a necessary assumption, since no higher frequency data exist, but is unlikely to be the case in the presence of waves. Any higher frequency motion is parameterised in the empirical value of the tuning parameters developed.

The frazil scavenging process is first examined with a simple model domain and a phenomenological parameterisation of the process is derived. The empirically-derived parameter is then used in a full dynamic-thermodynamic model which combines the findings of the two previous chapters to examine the amount of ice production in the frazil/pancake process compared to that which would occur under the same meteorological and dynamic forcing for a congelation ice cover. The role of HF motion in ice production for both cases is examined, and the effect on the balance between frazil and pancake ice remaining at the end of the simulation is discussed.

4.2 Convergence induced thickening

The movement of the outer array during Event 2 is considered, as this was previously identified as the source of the pancake top layers, grown by frazil scavenging. During Event 2, the thermodynamic model used in Chapter 3 grows an average of 1 mm of frazil solid ice equivalent (SIE) per 20 minute timestep (a rate of 8×10^{-4} kg m^{-2} s^{-1}) in the area fraction of frazil ice (0.35, averaging the values at the outer array buoy locations, Stations 1, 3 and 4 – see Table 3.1).

The volume of ice transferred from frazil to pancakes by the scavenging process is given by:

$$V = div.\Delta t.a_t.h_f\varepsilon \qquad \text{(Eq. 4.1)}$$

where div is the array divergence calculated in Chapter 2, a_t is the area of the array, h_f is the frazil slick thickness (SIE) and ε is the scavenging efficiency, expressed as the fraction of frazil volume traversed that goes to thicken the pancakes through scavenging. If a 100% scavenging efficiency is assumed for the moment – *i.e.* all the newly-formed frazil ice traversed by pancakes during the compression is scooped onto the surface of those pancakes – then a volume of 6.4×10^{4} m^3 of ice is scavenged during each cycle. Distributed over the area fraction of pancakes (0.65), this thickens the pancakes by 2.8×10^{-5} m during every cycle. We assume that area percentages remain constant despite the thickening pancakes. The duration of Event 2 (two days) represents 144 cycles of 20 minute compression-rarifaction. Thickening of the pancakes due to

compressive frazil scavenging is then 144 x 2.8×10^{-5} = 4 mm SIE. This is clearly much less than the 5 cm SIE observed in the field and initially suggests that frazil scavenging is not, in fact, an effective mechanism to build pancakes.

This figure does not allow for the pre-existing thickness of the frazil slick however: the pancakes are in fact pushed through a frazil layer considerably thicker than 1 mm during each compression cycle. It was established in Chapter 3 that the existing frazil slick formed at the end of Event 1 did not undergo significant melt in the intervening time until Event 2. The thickness of that slick is unknown, but the model runs (Figure 3.17) give a figure of 40 cm SIE (corrected ECMWF forcing). This was partially transformed into the lower layers of the observed pancakes with 7 cm SIE thickness, requiring 13 cm of frazil SIE, taking account of the area fractions. This suggests that the frazil slick available for building top layers had an SIE thickness of approximately 27 cm at the beginning of Event 2.

Taking this thickness into Equation 4.1, the compressive scavenging now equates to a pancake thickening-per-cycle of 7.5 mm SIE. Over the 144 cycles of Event 2, this produces a total pancake thickening of 108 cm, which is an order of magnitude more than observed. A simple estimate of the scavenging efficiency, ε, is thus 5/108 = 5%. This appears to be rather high, given the author's observations, but is a phenomonological value, subject to all the assumptions set out previously.

4.3 Establishment of an ice cover

The foregoing sections have established that the frazil scavenging which takes place during the high frequency motions of the pancakes may be highly significant in building pancake thickness, though may not influence the overall ice production to the same extent. To examine the effect of these high-frequency dynamics on ice production, the thermodynamic model discussed in Chapter 3 is coupled to an ice redistribution model, driven by the dynamics (specifically the divergence DKP) calculated in Chapter 2. The redistribution model deforms the ice cover in response to convergent or divergent dynamics and modifies its thickness and area accordingly. Ice volume is conserved during deformation events. The thermodynamic model then grows or melts ice on the

resulting ice cover at each time step. The model deals with both congelation and frazil/pancake ice within the area enclosed by the array. It is assumed that no ice volume exchange occurs with the area surrounding the array: ice cannot be pushed outside the area enclosed by the array. Application of this hybrid model allows the following questions to be examined:

- How does HF motion, as expressed by frazil scavenging, influence ice production in the frazil/pancake process?
- What are the contributions of the various processes (scavenging, deformation, thermodynamics) to the final thickness of a frazil-pancake ice cover?
- What is the ice production in a congelation ice cover undergoing the same motion? Hence, does the frazil-pancake cycle produce significantly more ice for the same forcing?
- Does the scavenging parameterisation result in a final (consolidation) thickness for the pancakes which is similar to observations?
- How does this final thickness compare with the rate-based approach developed in Chapter 3?

The intention is to establish whether the findings of the previous chapters have a significant impact on the amount and timing of ice production during the frazil-pancake cycle, and hence whether they need to be taken into account in larger-scale models concerned with ice formation or water mass modification.

4.3.1 Congelation redistribution model

The behaviour of a congelation ice cover is considered first, since this is the simpler of the two cases. The framework follows that of Thorndike *et al* (1975) in that the initial thickness and area fraction of an arbitrary number of ice classes are specified. Ice is grown or melted on each ice class for the duration of the timestep, according to the thermodynamic model described in the previous chapter. The ice cover is then deformed, using the change in area determined from the buoy positions. Open water is created during divergent events and the thinnest ice class present is crushed during

convergent events. If that ice class is exhausted before the convergence ends, the remaining convergence is carried forward to the next ice class. The area and mean thickness of each class are then recalculated accordingly. The type of deformation (ridging or rafting) is not considered, since the new class area defines the mean thickness for that class, without reference to its probability distribution function. Energetics (*e.g*. Hopkins (1998)) is not considered: the ice cover is taken to be infinitely weak. Spatial information about the structure of the ice is not considered. Ice volume is conserved during deformation events and the resulting ice cover re-classified before the next timestep. For comparison with the thickening of pancake ice at Station 1, initial conditions were set as shown in Table 4.1, equivalent to the 0.35 fraction of frazil ice and 0.65 fraction of 10 cm thick (7 cm SIE) pancakes, considered earlier. There is no predictable thickness to guide the choice of ice classes, as is commonly done for pack ice models (Haapala and Leppäranta 1996; Leppäranta 1998) other than open water (Class 1).

Table 4.1: Initial values for the redistribution model in congelation ice mode. Open water makes up Ice Class 1, with a limiting thickness to avoid divide-by-zeros in the growth model. Other ice classes are shown, defined by their limiting thickness.

Ice Class	**1**	**2**	**3**	**4**	**5**	**6**
Limit, cm	1	10	20	30	40	9999
Area fraction	0.35	0.65	0	0	0	0
Initial thickness, cm	$1x10^{-5}$	7	0	0	0	0

The model outputs thicknesses and areas of each ice class, together with the net ice production (m^3) and the 'equivalent thickness', *H*:

$$H = \frac{\sum_{i=1}^{n} a(i).h(i)}{a_{total}} \qquad \text{(Eq. 4.2)}$$

where $a(i)$, $h(i)$ are the areas and thicknesses of each ice class (1:n) and a_{total} is the area enclosed by the array. The dynamic resolution can be varied from the maximum, 20 minute, value to any chosen interval. The reduction in dynamic resolution is imposed as a low-pass filter (LPF) on the buoy motions. The filtered change-in-area is then applied at 20 minute intervals, regardless of the dynamic resolution chosen. Meteorological forcing is also applied at 20 minute intervals regardless of the LPF chosen, using cubic spline interpolation from the one hour native interval. This scheme ensures that only differences in the fine-scale motion of the buoys are contrasted: no difference in meteorological forcing is applied.

Model runs were then performed at 20 minute, 2 hour and 6 hour resolutions to examine the effect on modelled ice production. An example of model output for a congelation ice run (20 minute resolution) is shown in Figure 4.3. Starting area of the array was 1.8×10^9 m^2, reducing to 5.1×10^8 m^2 at consolidation – a reduction of 72% in area. Convergence thus plays a dominant role in the ice dynamics, with the array only beginning to diverge significantly towards the end, after Day 122. Relatively cold air temperatures quickly grow ice on this open water and the final array area is evenly divided between very thin (5.6 cm) new ice and the much thicker ice (59.7 cm) resulting from the long convergence. Elevated air temperatures at the beginning of the run (days 113 -116) melt a significant amount of ice before the cold air outbreaks begin once more. Total ice production over this period was 6.72×10^7 m^3, representing an 81% increase from the initial volume. Average ice thickness over the area of the array was 29.8 cm at the end of the simulation, compared to 4.6 cm at the beginning. Ice growth was responsible for 13.3 cm of the increase, with deformation accounting for the remaining 11.9 cm. The model was then run with reduced resolution forcing and the results for ice production and equivalent thickness are shown in Table 4.2.

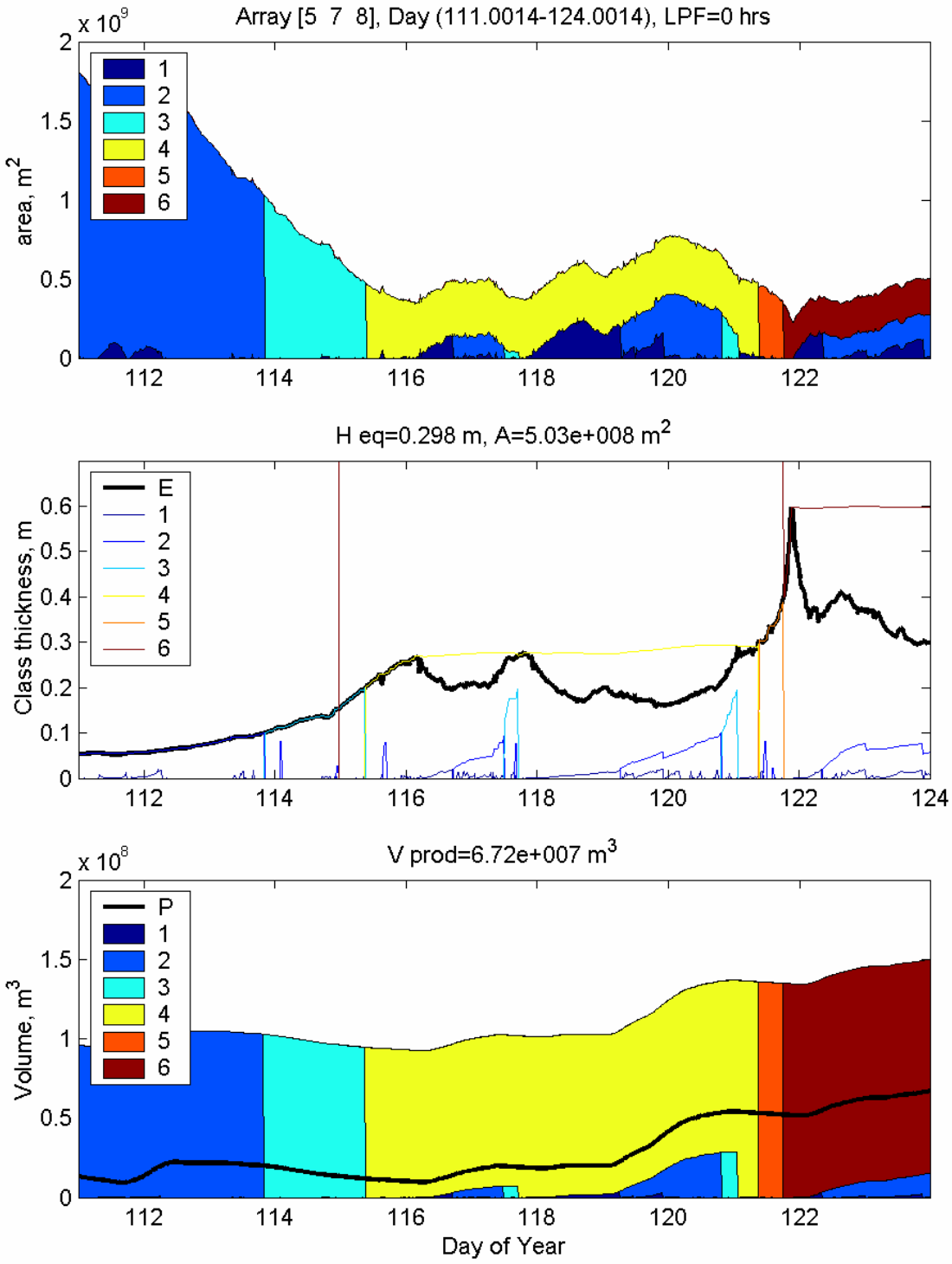

Figure 4.3: Redistribution model output for congelation ice. The top graph shows the array area (outline curve) and the contributions to it from the various ice classes, indicated in the legend. The period is dominantly convergent, reducing to nearly a quarter of its original area in the first five days. Thicker ice is formed during the convergence, indicated by the progressive increase in ice class. Middle graph shows the equivalent ice thickness over the array area (E: thick black curve) and for each ice class. Bottom graph shows the contribution of each ice class to overall array volume. Also shown is the net ice production (P: thick black curve). Though Class 6 covers less than half the final array area, it is the dominant contribution to total final volume, at just under 60 cm thickness.

Table 4.2: Results for the congelation redistribution model runs for various time steps. The table shows the cumulative percentage convergence (*Σ conv*) and divergence (*Σ div*) over the model run (days 111-124), calculated from the buoys' positions, the equivalent thickness *H* (from Equation 4.2) and total ice production (*V prod*). The last column calculates the change in ice volume production from the six-hour run.

Step	**Σ conv, %**	**Σ div, %**	***H*, cm**	**V prod, x10^7 m^3**	**% 6 hr change**
20 mins	201	129	29.8	6.72	8
2 hours	144	72	29.1	6.41	3
6 hours	131	59	28.9	6.23	0

The effect of the high frequency motion on the ice production within the array is in fact rather small, only increasing by 8% over the six-hour filtered result, though the cumulative convergence (sum of all convergent events, with respect to the original area of the array) increases from 131% to 201% and the cumulative divergence from 59% to 129%.

This surprising result was examined by plotting the difference in ice production between the 20 minute and six-hour runs, together with the air temperature time series from buoy DML8 (Figure 4.4). The high frequency (20 minute interval) ice production curve increases with respect to the six-hour filtered results dominantly during divergent periods with low air temperatures, where more open water areas for rapid ice growth are created. These open water areas have a large contrast in heat flux compared to the compact, converged ice. The low-temperature event centred on Day 120 does not give rise to increased production in the 20 minute resolution run since sustained secular convergence occurs and the amplitude of the high-frequency oscillatory divergence drops sharply over this period (see Figure 2.19a).

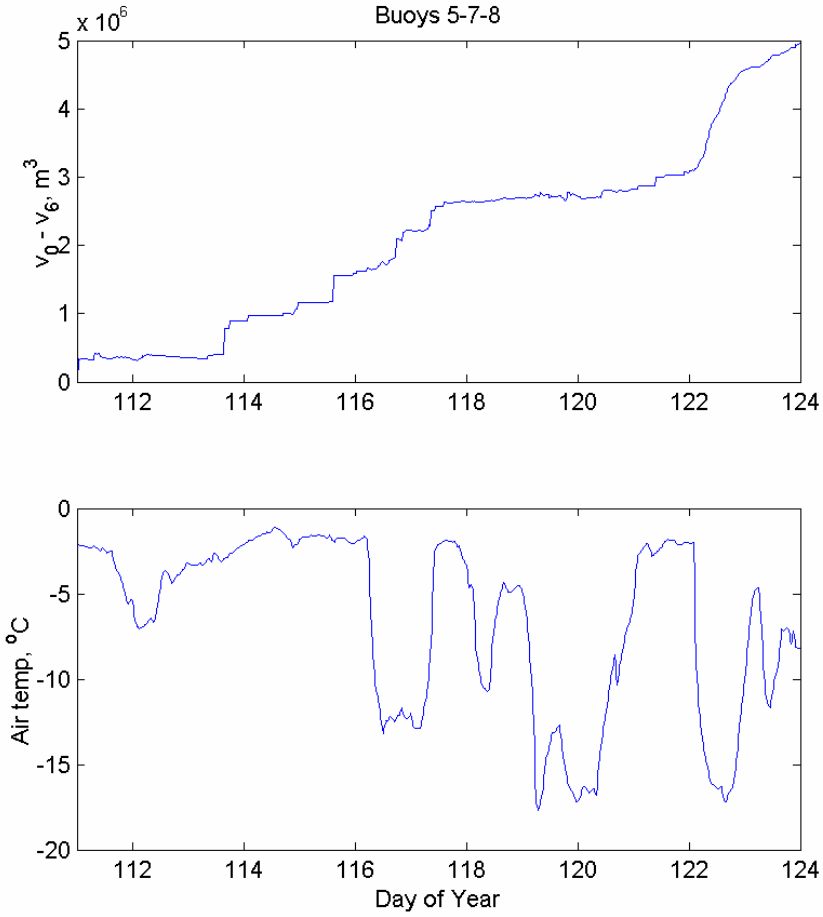

Figure 4.4: (top) the difference in ice production volume between the 20 minute model run and the six-hour filtered run. (bottom) air temperature from buoy DML8.

Ultimately the difference in ice production is not large because the area involved in the high-frequency oscillations is small compared to overall area of the array. A typical divergence of 1.5×10^{-5} s^{-1} implies that an area of around 9×10^{6} m^2 is involved in each convergent-divergent oscillation, which represents less than 2% of even the final, reduced, array area. If an open water area is re-established with every second timestep (*i.e.* the ice grown in the previous timestep is removed to allow maximum congelation ice growth rate each time), the ice grown on this area will have a thickness of approximately 37 cm, using the buoy meteorological forcing. This gives a total ice volume production in the oscillating area of 3×10^{6} m^3, which represents around 5% of the total volume production over the array. The area involved in the oscillation is

therefore significantly more productive than the array area as a whole (producing 5% of the ice volume in less than 2% of the area), but cannot significantly influence the overall ice production due to its small area fraction.

Of course, the analysis of Chapter 2 established that a consolidated ice cover would not undergo such high-frequency motions. The purpose of the exercise is to establish a comparative figure to that which would arise under the same forcing and deformation as the frazil-pancake model. Accordingly, we note that the equivalent thickness over the area of the array was 29.8 cm at the end of the simulation, compared to 4.6 cm at the beginning. The increase is evenly divided between thermodynamic growth (13.4 cm) and convergence (11.8 cm).

4.3.2 Frazil/pancake redistribution model

For the frazil/pancake calculation, only two ice classes – frazil ice and pancake ice – exist. The five assumptions detailed in Section 4.1 are maintained, and the model parameterises the following processes:

- Frazil ice is scavenged, thickening the pancakes, during convergent events, according to Equation 4.3, overleaf
- Convergence reduces frazil area and thickens the frazil slick (and *vice versa*)
- A minimum frazil area of 10% is maintained, dictated by the maximum hexagonal close packing of the (assumed) circular pancakes
- Further convergence induces rafting of the pancakes. Though this is a discrete process – an individual pancake's thickness can only increase by multiples of the pancake thickness – the number of pancakes taking part in the rafting is variable, and this is indistinguishable in the model domain from fractional thickening.

While sufficient frazil area exists, pancakes scavenge frazil ice according to the following equation:

$$h_p^{'} = h_p + \frac{\Delta A_f h_f \varepsilon}{A_p} \qquad \text{(Eq. 4.3)}$$

Where h_p is the pancake thickness, ΔA_f is the reduction in frazil area due to convergence, h_f is the frazil slick thickness, ε is the scavenging efficiency and A_p is the area of pancake ice. The numerator expression represents the volume of scavenged frazil ice, equivalent to that given in Equation 4.1.

Two additional processes are parameterised in the model, following initial trials.

If the frazil area is small and compression continues, then the frazil slick thickness between the pancakes will increase to very large values. Such a slick would greatly exceed the draft of the surrounding pancakes and in fact spread out underneath the pancakes to occupy their area as well. This is therefore allowed to occur in the model. The frazil area is split into 'frazil-with-a-free-surface' and 'frazil-under-pancakes'. The partitions are tracked separately, with the frazil retreating from underneath the pancakes once the slick thickness drops below the pancake draft once more. Volume fractions are accounted for when determining whether the frazil can under-ride the pancakes. Ice production only occurs in the frazil-with-free-surface fraction. Reduction in the volume concentration of the frazil slick with depth is not parameterised, since no reliable field measurements exist.

During prolonged divergent events, the model created large area fractions of frazil ice, which subsequently produced large ice volumes and resulted in unrealistically-high frazil slick thicknesses. The model was therefore refined to mimic the transformation of frazil ice into pancakes seen in the field. Transformation only occurs if the frazil area exceeds 35% of the array area. This value was commonly observed in the field and it is assumed that smaller areas of frazil are disrupted by the existing pancakes travelling through them during the scavenging process and are thus unable to consolidate into pancakes. Larger area fractions of frazil are required to 'age' (in accordance with helicopter observations at the ice edge) before transformation into pancakes takes place, and hence the age of each positive increment in frazil area is tracked. Once an area of

greater than 35% has exceeded the age threshold (24 hours, in accordance with field observations), 65% of that area is transformed into new pancakes of the observed 5 cm solid ice equivalent thickness, having regard to volume fractions. If insufficient frazil volume is available (*i.e.* the slick is too thin), then the transformation still occurs but the new pancake thickness is adjusted accordingly. Transformation may not in itself reduce frazil area to less than 35%, though this may occur during subsequent convergence. Total frazil and pancake volume is conserved during the transformations, with the partition between free frazil and under-pancake frazil adjusted before thermodynamic growth occurs in the timestep.

Model output is shown, with settings equivalent to the congelation model, in Figure 4.5. The array area follows the same form as before, this time divided between only frazil and pancake ice. Compression quickly takes up the initial 35% frazil area, reducing it to the minimum 0.1 fraction specified. No initial frazil conversion to pancakes takes place, since the frazil fraction has dropped below the 0.35 threshold before it has aged sufficiently. Divergence restores sufficient fraction to convert after day 116, increasing the pancake area fraction in stages from thereon.

Pancake thickness rises quickly once the initial frazil compression is complete, through a combination of rafting and frazil scavenging. It should be noted that the thicknesses plotted in the middle graph are averaged over the area occupied by the pancakes. Average thickness therefore drops when thin, new, pancakes are added to that area following conversion from frazil ice. Equivalent thickness over the whole array area is 44 cm.

Total ice volume produced in this scenario is 1.32×10^8 m^3, representing an increase of over 96% on the congelation equivalent presented in the previous section. This growth, which occurs purely in the interstitial frazil fraction, is partitioned between the final frazil slick (8.1×10^7 m^3), frazil scavenged onto the pancakes (3.5×10^7 m^3) and frazil transformed into new pancakes (1.6×10^7 m^3). Final pancake thickness is around 40 cm SIE, or 57 cm actual thickness. Scavenging only contributes 10.6 cm of this SIE

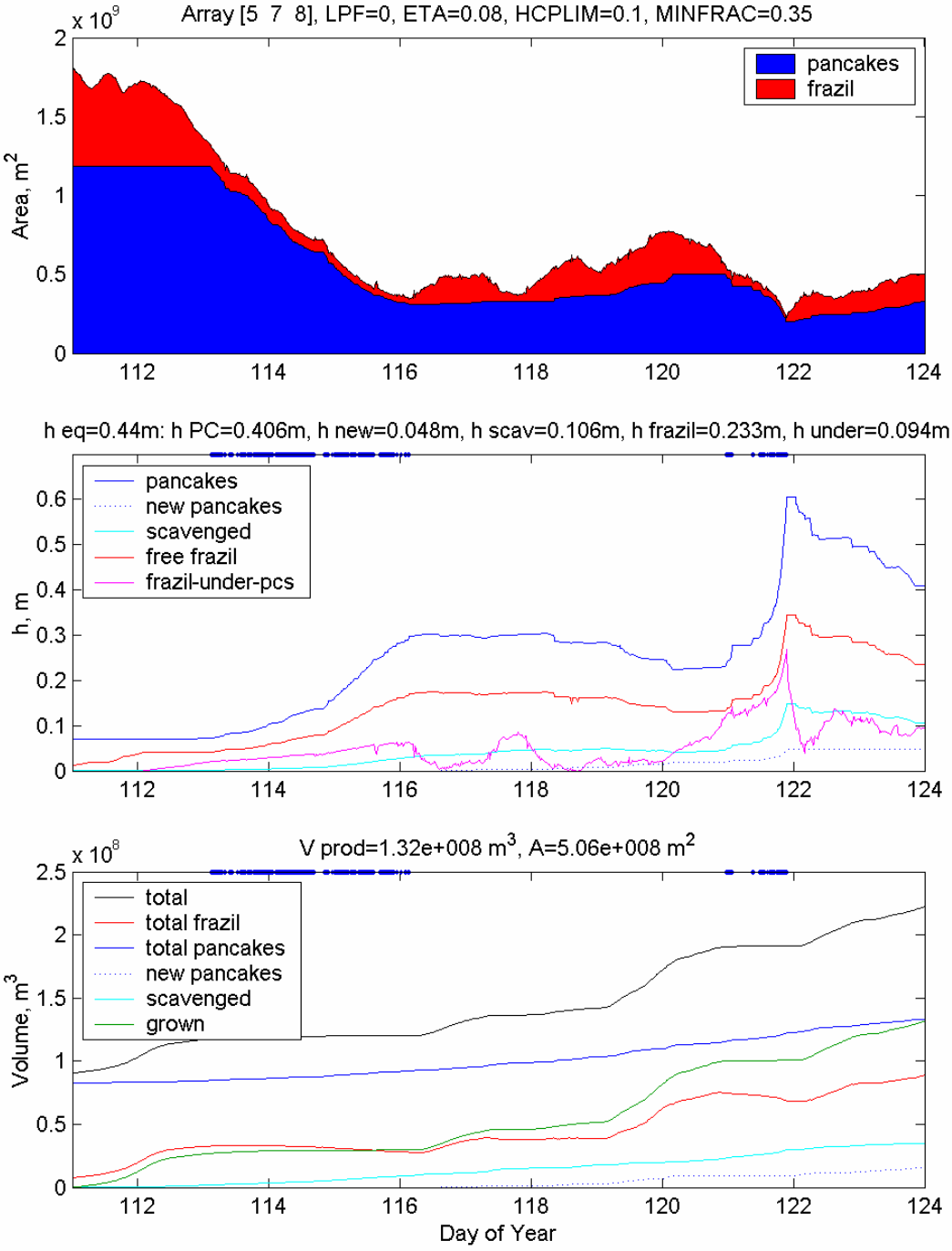

Figure 4.5: Output of the frazil/pancake redistribution model. The top graph shows the areas of frazil and pancake ice. Positive steps in pancake area indicate the conversion of 'aged' frazil to thin pancakes. A minimum fraction of 0.1 frazil is maintained, in accordance with hexagonal close packing. The middle graph shows the thickness of pancakes, indicating that due to scavenged frazil ice (cyan) and conversion from frazil (blue dashed). Also shown are the frazil slick thickness between pancakes (red) and underneath the whole area (magenta). The bottom graph shows the volume of the various fractions, including the thermodynamically-grown component (green). Blue dots on the upper bound of the graphs indicate that pancake rafting is taking place.

thickness, with rafting being the dominant thickening mechanism at 18.2 cm contribution. This is expected given the sustained compression undergone by the array. New pancakes, transformed from frazil ice contribute less than 5 cm of the final thickness. Final frazil slick thickness exceeds that of the pancakes, in volume fraction terms, with 9.4 cm SIE frazil underlying the whole area. Table 4.3 summarises the output of the model for various resolutions.

Table 4.3: Model output volumes and thicknesses for dynamic forcing with various low-pass filters (LPF) applied. Total and partial pancake thicknesses are shaded. The 'total' figure also includes the 7 cm SIE starting thickness of the pancakes

LPF	**20 mins**	**2 hrs**	**6 hrs**
Total ice production, x10^7 m^3	**13.2**	**13.8**	**13.7**
Frazil volume, x10^7 m^3	8.9	10.9	11.3
Pancake volume, x10^7 m^3	13.8	11.9	11.3
Equivalent thickness, cm	**44.0**	**45.0**	**45.0**
Total pancake thickness, cm	40.6	36.2	36.0
Scavenged contribution, cm	10.6	6.4	5.5
Transformed contribution, cm	4.8	4.6	4.2
Rafted contribution, cm	18.2	18.2	19.3
Interstitial frazil thickness, cm	23.3	20.8	20.7
Under-riding frazil, cm	9.4	14.2	14.8

The application of high-resolution (20 minute) dynamic forcing has very little effect on overall ice production in the frazil/pancake model. This is expected, since such forcing only serves to thin-and-thicken the frazil slick, as discussed, unlike the congelation ice case. The major effect of the high-frequency forcing is to increase the volume fraction

accounted for by pancakes and reduce the frazil fraction. This arises from increased scavenging of the frazil slick by the pancakes, as demonstrated by almost double the contribution from scavenging at 20-minute intervals (10.6 cm) as for two-hour (6.4 cm) or six-hour (5.5 cm) forcing. This is understandable, given the increased path length that the pancakes are subjected to with the high-frequency dynamics. Figure 4.6 shows the dependence of total pancake thickness, the scavenged contribution and total frazil thickness on ε. Physical thickness are shown, as opposed to solid ice equivalents. The point at which frazil ceases to be deeper than the pancakes is then shown by the crossing point of the two curves ($\varepsilon \cong 17\%$). Other contributions to pancake thickness (rafting, transformation) remain similar, as would be expected from the dominance of large-scale dynamics in these processes.

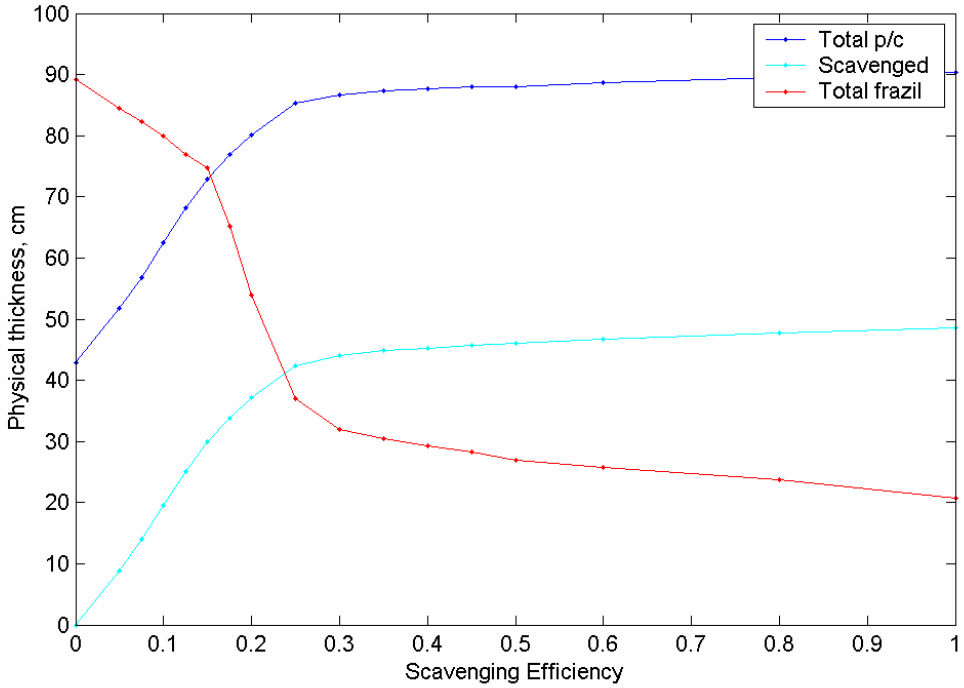

Figure 4.6: The effect of scavenging efficiency ε on the scavenged and total pancake thickness. Also shown is the total frazil thickness (interstitial + under-riding). All figures are generated at the full (20 minute) resolution forcing and show physical (rather than SIE) thicknesses.

The scavenging efficiency has a rather linear effect on the contribution of frazil ice until a value of 0.25, where the contribution reaches 40 cm physical thickness. The frazil slick thickness drops rapidly over the same interval, resulting in a severely reduced frazil volume for the scavenging to operate upon. Increasing scavenging efficiency beyond this point therefore has a much smaller effect. The 'irreducible' frazil thickness of 20 cm with 100% scavenging efficiency results from the divergent period at the end of the simulation: the pancakes do not converge sufficiently to scavenge the ice produced during this cold-air outbreak.

Also interesting is to examine how the choice of ε impacts the influence of the HF motion, in terms of the scavenged contribution to pancake thickness. Scavenged layer thickness for 20-minute and six-hour resolution runs is plotted in Figure 4.7. Increasing scavenging efficiency increases the influence of the HF motion until a maximum is reached at around $\varepsilon \cong 17\%$ - the same value at which frazil ceases to under-ride the pancakes in the full resolution simulation.

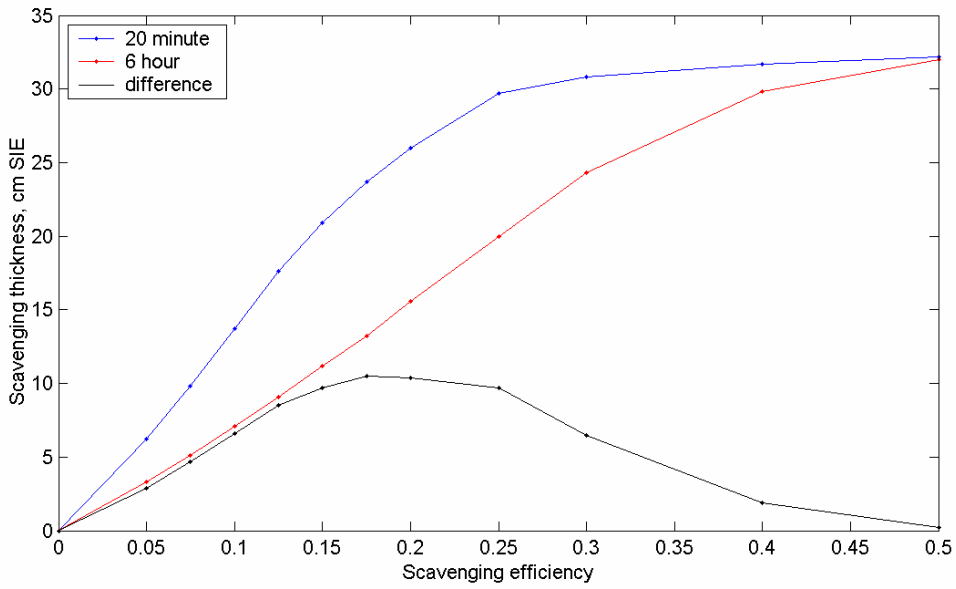

Figure 4.7: The thickness of the scavenged pancake layer versus scavenging efficiency, plotted for 20-minute forcing (blue) and six-hour forcing (red). The black curve shows the difference between the two forcing results. All figures are solid ice equivalents.

Beyond this, the increased scavenging exhausts the frazil reservoir more quickly at full resolution, while the six-hour forcing continues to scavenge effectively. An ε value of 0.5 is sufficient for even the six hour forcing to scavenge all the available frazil and build an equivalent layer thickness to that seen in the full resolution simulation.

The primary aim of the model is to compare ice volume production between high- and low-frequency forcing, and between congelation and frazil/pancake ice covers. The lack of observations of thickness or area during the consolidation period, combined with the interacting processes parameterised in the model, leave the output values open to question, however. Most questionable is the tuning parameter 'MINFRAC' – the minimum area fraction of aged frazil that must exist before transformation into pancakes occurs. The value of 0.35 was chosen with respect to field observations which showed this value to be fairly constant across the pancake zone, and a physical justification was suggested. No frazil ice was observed at Station 2, however, and this constraint may be erroneous in the presence of the sustained compression undergone by the array. The parameter effectively controls the surface area available for ice production, since the model only produces ice in the area occupied by interstitial frazil. The effect of varying MINFRAC is shown in Table 4.4, in terms of volume production and mean pancake thickness.

Turning off the constraint (setting it equal to the maximum packing density) severely limits ice production to unrepresentative levels. Production and maximum thickness are reasonably stable around values suggested by observations, however (range 0.3 to 0.4).

Table 4.4: Dependence of ice volume production and equivalent thickness *H* on MINFRAC; the minimum area fraction of frazil ice necessary to allow its conversion to pancakes. A value of 0.1 is equivalent to removing the parameter, since this minimum fraction cannot be reduced due to packing density constraints. The value chosen in the model (0.35) is shown in bold.

MINFRAC	**Volume x10^7 m^3**	***H*, cm**
(0.1)	5.8	29.4
0.2	9.0	35.6
0.3	11.7	41.1
0.35	**13.2**	**44.0**
0.4	14.5	46.6
0.5	16.6	50.9

4.3.3 Rate–based approach

The explicit dynamics-based approach used in the previous sections can be compared with the rate-based method developed in Chapter 3. The thermodynamic model is run with the buoys' meteorological forcing to determine the frazil production rate, per square metre of interstitial frazil area (*i.e.* taking no account of the area fraction of frazil). The production per timestep is then adjusted by the ratio determined in Section 3.3.2.6 to determine the ice production in the frazil-pancake cover. This is finally combined with the area of the array during that step and the cumulative ice production estimated. The procedure is expressed in Equation 4.4 and illustrated in Figure 4.8:

$$V = \frac{\Delta t}{\rho_i} \sum_{i=1}^{n} RR.FR_i \, a_i \qquad \text{(Eq. 4.4)}$$

Where *RR* is the relative rate of top layer formation, compared to frazil ice (5.5:9.5), FR_i is the calculated frazil formation rate at timestep i and a_i is the area of the array at timestep i. ρ_i is the density of ice and Δt is the timestep in seconds.

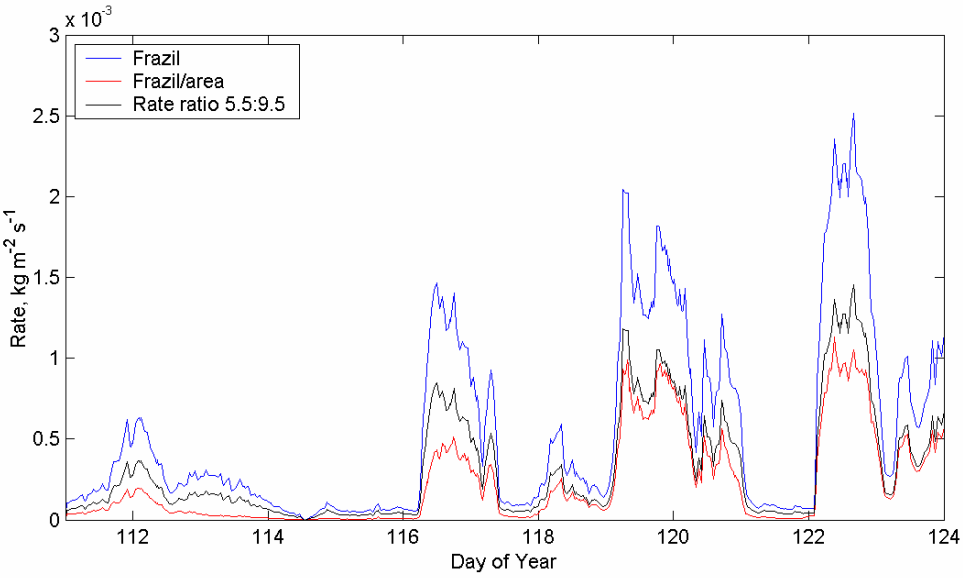

Figure 4.8: The rate of ice production until consolidation. The blue line plots the rate per square metre of frazil ice, the red line shows the rate per square metre of total array area and the black line applies the rate ratio to the blue curve to give the effective top layer ice production, as determined in Section 3.3.2.6.

The exercise suggests a total volume production of around 1.44×10^8 m^3, which represents an increase of only 10% over the figure produced by the redistribution model.

4.4 Discussion

The agreement between rate-based and redistribution models for ice production is initially surprising, since the former model does not explicitly parameterise the change in productive area. The area fraction of frazil within the array is constrained within the limits of 10% (maximum packing density of pancakes) and around 35%, however, since transformation into pancakes is allowed to occur above that value. The rate ratio of

5.5:9.5 was developed with a similar area fraction (0.35) and, presumably, a similar dynamic regime. Though the buoy array undergoes dramatic convergence during the period of investigation, such convergence is quite normal given the constant passage of low-pressure atmospheric systems past the ice edge. Such self-similar area fractions and dynamic conditions suggest that the rate ratio may vary significantly in other applications, however.

The redistribution model offers a more widely applicable solution to the modelling of frazil-pancake ice covers. The simulation results in a frazil slick thickness which is significantly higher than field observations suggest is realistic, however. The very limited number of observations in the Weddell Sea and Odden have never observed the frazil slick to be deeper than the pancakes embedded within it, whereas the model suggests a physical frazil thickness of nearly 82 cm, compared to a physical pancake thickness of 58 cm. The interacting nature of the various processes in the model render it difficult to establish which factor is responsible for this shortcoming, since frazil slick thickness may be reduced by any of the following means:

1. The scavenging efficiency can be increased. The 5% value is based on a modelled frazil thickness at the end of Event 1, which may itself be erroneous. Significant increases in the value of the parameter are required to reduce final frazil thickness to values more in line with field observations, though the model is relatively insensitive for $\varepsilon > 25\%$, at which point frazil thickness is more in line with observed conditions in the field. Such a radical shift in value for ε would require that the frazil slick thickness at the end of Event 1, from which the value was originally derived, was in fact 17 cm instead of the modelled 27 cm, which is quite possible. Ice volume production is unchanged.
2. The scavenging efficiency may vary with the area fraction of the slick. It can be envisaged that significantly reduced frazil area fractions are more efficiently scavenged onto the surface of the pancakes, since a mutual barrier exists to prevent the frazil crystals being pushed aside rather than over the pancakes. This is similar to the formation of pancake rims described in Pedersen and Coon (2004), which describes frazil being “pumped over the two converging edges of

cakes". No data exist on this process, though it may be tractable to numerical simulation or study in an ice tank. Again, ice volume production is unaffected.

3. Significant volumes of frazil may be transformed into pancakes by the 'classical' bottom accretion method, not parameterised here
4. The rate of frazil production may drop as the frazil slick thickens, as discussed in Chapter 3
5. Ice volume may not be conserved within the array.

The uncertainly over the scavenging efficiency hampers the assessment of the importance of the high frequency motion, since it directly impacts the one process which varies significantly with this small-scale oscillation. The impact of the process varies significantly over the range $0.10 < \varepsilon < 0.25$ and is relatively insensitive at other values. This range also encompasses the 'maximum impact value' of 0.175, at which the HF relative motion has the most effect on scavenged layer thickness, as indicated by the maximum difference between 20-minute and six-hour results.

It is interesting to note that this maximum impact coincides with the disappearance of the under-riding frazil layer. The correspondence is far from co-incidental and demonstrates an emergent property of the model parameterisation, which does not consider the under-riding frazil to participate in the scavenging process. The under-riding frazil thus acts as a reservoir to replace the interstitial frazil removed by scavenging, enabling the increased scavenging efficiency to directly increase the scavenged volume. Once this reservoir is exhausted, however, continued scavenging will deplete the interstitial frazil thickness, reducing the impact of more efficient frazil removal. The six-hour simulation can then 'catch up' with the 20-minute results, since it takes longer for this reservoir to be depleted in the absence of the HF motion.

4.6 Summary

- The concept of ‘scavenging efficiency’ was introduced and defined as the percentage of frazil slick volume traversed by the pancakes which goes to increase the top layer thickness of those pancakes. A value of 5% was derived with reference to the magnitude of the divergence calculated in Chapter 2 and the top layer pancake growth determined in Chapter 3.
- The effect of the high frequency oscillations on a hypothetical congelation ice cover was examined using a redistribution model. 20-minute and six-hour resolution dynamic forcing resulted in a difference in ice production of 8% - a similar order to the percentage of total array area involved in the oscillation.
- A frazil-pancake redistribution model is described, incorporating many of the processes occurring during pancake formation. The new ice production is found to be insensitive to the high-frequency oscillations, though these increase the volume of ice scavenged from the surrounding frazil slick. The balance between final pancake and frazil volumes is thus significantly different.
- The HF motion had maximum effect on the scavenged ice volume at a scavenging efficiency of 17%, which corresponded to full utilisation of the under-riding frazil volume.
- Ice production was found to be approximately double that of a congelation ice cover undergoing the same dynamical and meteorological forcing.
- Ice production was compared to the rate-based model of Chapter 3, and good agreement was found (within 10%), though that model takes no account of convergent dynamics. It is suggested that the convergent regime was similar during the formation of the observed pancakes (prior to buoy deployment) and hence the rate ratio was pre-tuned for the representative dynamics.
- It was suggested that the frazil slick thickness produced at the end of the simulation by the redistribution model was too high compared with field observations and possible reasons were examined, centring on the value of the scavenging efficiency parameter. Increasing this from 5% to 25% gave results which were more in accordance with field measurements.

CHAPTER 5: DISCUSSION AND CONCLUSIONS

The observations and analysis in this thesis have examined the formation of sea ice in the presence of turbulence and quantified the high frequency motion and growth rate of this ice for the first time. A new mechanism for the transformation of frazil to pancake ice was introduced and a coherent 'family' of pancake morphologies delineated. The findings were combined in a physical model to simulate the timing and volume of ice production in the region, from the beginnings of the ice cover to its final consolidation thickness. As is normal in scientific investigations, the journey has thrown up many questions along the way and underlined the uncertainties in our understanding of the young sea ice cover, mostly arising from a lack of field observations.

The following chapter highlights the major findings of the study and discusses their merits and shortcomings. The importance of the study is considered in the wider context of determining the timing and volume of ice production in large scale models. Finally, further investigations are suggested to address the main uncertainties.

5.1 Dynamics

Striking differences were seen between the drift of pancake ice and the immediately-following consolidated pack ice. Relative motion between the buoys displayed the most marked change, with DKPs during the pancake phase exhibiting high amplitude oscillations which ceased overnight when the ice cover consolidated. The amplitude of the DKPs (1.5×10^{-5} s^{-1}) was approximately two orders of magnitude higher than previously seen in Weddell Sea pack ice and was dominantly due to the meridional component, consistent with the zonal orientation of the ice edge and the consequent freedom in the north-south direction. The high amplitude oscillations were only evident at the full, 20-minute resolution: two-hour low pass filtered DKPs showed a much reduced contrast across the consolidation boundary. The relatively short sampling interval of the buoys (compared with previous Argos-based investigations) was thus able to demonstrate this motion for the first time, though short sampling interval GPS drifters have been used in previous experiments in other regions (e.g. Leppäranta *et al.* 2001). The MIZ has long been recognised as having higher magnitude DKPs than pack ice (e.g. Hibler III *et al.* 1974) but the pancake ice was found to be unique in having such an elevated level of energy at periods less than six hours, having an almost 'flat'

(white noise) spectrum in this range, as opposed to the red-noise (reducing power with increasing frequency) character of the both the consolidated ice cover and the summer MIZ as the buoys broke out into the open ocean at the end of December.

The forcing mechanism responsible for this HF motion is currently unclear, though the action of waves – either surface gravity or internal – is postulated as the most likely candidate. Investigation of pancakes' motion during convergence-divergence appeared intractable with significant theoretical difficulties and inconclusive ice tank results (Frankenstein 1996). The stochastic approach detailed in Shen and Squire (1998) parameterises collisions between pancakes to determine their contribution to wave attenuation and may be adaptable to consider relative separations between pancakes, though it necessarily deals with monochromatic waves rather than real-world spectra.

Other parameters suggested that the unconsolidated pancake phase represented a starting point (minimum) in a cycle of constraint. This constraint reached a maximum in mid-August (mid winter), when the buoys were embedded deep in the pack ice of the Weddell Sea, and was progressively relaxed as the buoys approached the ice edge at the end of winter. The cycle of constraint was largely expressed at periods shorter than 12-hours, though simple drift speeds exhibited the same trends.

Derivation of momentum transfer functions (wind factor, turning angle) for pancake ice were hampered by the failure of the on-board compasses for those buoys which remained in unconsolidated ice for the longest. ECMWF winds were not accurate while the buoys were close to the ice edge, but best fit values of 2.9% and 13° with respect to the 10 m winds were in accordance with values derived from the northern hemisphere Odden. The agreement suggests that these values can be used globally for pancake ice.

5.2 Thermodynamics

Two disparate mechanisms of frazil ice transformation into pancakes were identified: the classical accretion process by which the frazil first begins to agglomerate; and the

significantly faster subsequent frazil over-topping which occurs once platforms exist to support it. A 'family' of pancake types was identified which was consistent with the two processes, including a composite congelation-frazil structure (*Type-D*). It is suggested that these were examined during earlier studies of the area (Lange *et al.* 1989; Lange and Eicken 1991) but were not recognised at the time.

Many uncertainties have emerged during the course of this study, centred on the modification of ocean-atmosphere heat fluxes by the evolving pancake-frazil ice cover. The treatment of Chapter 2 makes no assumptions about any reduction in heat flux, since the frazil production modelled there simply represents a maximum rate for comparison with the observed pancake and frazil thicknesses. The redistribution model presented in Chapter 4 does assume that (a) only the interstitial frazil area contributes to ice production; and (b) the rate is not modified from the 'free surface' figure. These two assumptions have opposite effects on the ice production. Chapter 4's model produces a frazil slick which is far thicker than the limited field observations would suggest, though the overall volume (and hence equivalent thickness) of the ice cover is in close agreement with the figure suggested by field measurements. It is left to the 'scavenging efficiency' tuning factor to reduce the frazil thickness to values which are perceived to be less extreme, shifting the volume to be dominantly pancake ice as observed.

Little literature exists to aid our understanding of these effects. Most measurements and theory development have been focussed on frazil formed at low area concentrations in relatively small leads or polynyas, which is subsequently herded downwind until it collects against the edge of the lead or polynya and freezes into a solid ice sheet. Important considerations in this type of modelling are wind speed and fetch (lead width), which indirectly parameterise the turbulence which both limits frazil production and mixes the frazil crystals down into the water column, determining their volume concentration.

These parameters have little relevance to the vast frazil/pancake fields of the Antarctic: turbulence levels there are largely determined by the high amplitude swell impinging on the ice cover from the Southern Ocean. Turbulence is thus determined by non-local

wind forcing (distant storms) and the dimensions of the ice cover (thickness, area concentration, distance) between the measurement site and the open ocean, plus the properties of the waves themselves (amplitude, period). Pedersen and Coon (2004) nonetheless presented a non-physical best-fit of Alam and Curry's (1998) wind speed to ice thickness relation for the Odden. This is partly justified since the relatively small-scale of the Odden implies a closer proximity to storm wind forcing and a far less significant degree of damping of the resulting ocean waves by the ice cover. They found that an empirical 'lead width' of 1.5 km fitted the observed pancake thickness best, though the scatter was considerable.

Additional disconnections between the lead-derived and MIZ frazil treatments are the lack of a 'dead zone' in the MIZ, where the frazil damps the short period waves and consolidates, other than at the limit of the frazil-pancake zone itself. Langmuir circulation appears to play little or no role in the frazil-pancake cover, which invariably forms a homogenous mixture and is not observed to organise into downwind rows, except in very low areal concentrations at the ice edge.

Conceptually, it seems unlikely that only the interstitial frazil area contributes to ice production. Indeed, it is difficult to see how 35% of the productive area can produce ice at 58% of the overall free-surface rate – as demonstrated by modelled top layer growth in Chapter 3 - with this assumption intact. The pancakes are small and highly mobile and it is therefore not unreasonable to assume that the entire area "sees" the cold atmosphere at the integrated timescales over which heat loss from the ocean occurs. The situation is analogous to the heat exchange over leads, where the area-integrated heat flux is initially very sensitive to lead width and spacing, but becomes markedly less sensitive as ice concentrations drop below about 70% (Worby and Allison 1991). Worby and Allison point out that the air over the additional open water area has "already been modified" by the open water immediately upwind. Additionally, the pancakes are porous, unlike congelation ice, and the water within them is therefore less insulated from the cold air than would be the case under a congelation ice sheet.

An opposite effect is the modification of ocean-atmosphere heat fluxes by the presence of a frazil/pancake ice cover. Turbulent fluxes dominate heat exchange during frazil formation and the various methods of calculating these each use parameters that are modified by an ice cover. Bulk formulae use an exchange coefficient, while Monin-Obukov similarity theory requires a roughness length, which is certainly different from the open water value. Very thick frazil slicks, such as that observed in the Odden (Figure 4.2) will modify the area-integrated surface temperature from the freezing point of seawater, as will the presence of pancakes, the cooling of whose top surfaces will also account for some fraction of the heat flux which would otherwise contribute to ice formation (Leonard *et al.* 1998).

Given the supposed over-production of Chapter 4's frazil model, the rate reduction effect may be expected to dominate. This expectation is enhanced by the tank measurements of Smedsrud (2001), which determined a rate less than one third of the unmodified production with similar fluxes, though various reservations were expressed (Chapter 3) as to the equivalence of tank and field conditions, centring on the relative turbulence and mixing levels.

5.3 Scavenging model

The scavenging redistribution model, presented in Chapter 4 represents a first attempt at realistically simulating the timing and volume of ice production in the period before consolidation. It is perhaps fortuitous that the model reproduces the 60 cm thick ice cover suggested by earlier field observations (Wadhams *et al.* 1987), given the many assumptions discussed above. Consolidation is directly caused by the cessation of wave motion, rather than thickening of the pancakes *per se*, of course. Attenuation of the open ocean wave field occurs as the waves pass through the frazil-pancake zone from the open ocean. The loss of energy by the waves is a complex function of the penetration, ice concentration, the dimensions of the various ice types present and the wave properties (period, amplitude) themselves.

The model does give considerable insight into the processes involved, though it pushes the existing data to the limits of their applicability. Its usefulness lies in defining the

questions that need to be asked to improve the model, discussed in Section 5.4.2, which centre on placing the phenomenological parameterisation of scavenging efficiency into a more physically justified framework .

5.4 Conclusions

The thesis began by posing three main questions which bear repeating here:

1. What is the rate of ice production during pancake formation?
2. What are the implications of differential motion for ice production?
3. Do the results have any relevance for the wider modelling community and hence require incorporating into larger-scale models?

Though many new questions have arisen in the course of the investigation, the study has provided robust answers to these questions and these are summarised below.

Ice production in the pancake/frazil process proceeds at approximately double the rate of a thin congelation ice cover. This doubling holds for both the ice cover observed during the field experiment (top layers) and during the subsequent modelled growth to consolidation. The rate of ice formation, relative to the limiting free-surface frazil production, was found to be 0.58 during the formation of the pancakes' top layers. Applying this ratio to the meteorological data provided by the buoys until the onset of consolidation gave a total ice production figure (1.4×10^{9} m^3) within 10% of the value determined by the redistribution/scavenging simulation (1.3×10^{9} m^3). The congelation redistribution model formed 6.8×10^{8} m^3 during the same period. Mean ice production was determined as 5.5×10^{-4} kg m^{-2} s^{-1} during the formation of the top layers, 80% more than tank experiments with a comparable ocean-atmosphere heat flux (Smedsrud 2001) but well below estimates for frazil production in polynyas (Bauer and Martin 1983).

Initial stages of pancake formation appeared to be much slower, producing ice at approximately the same rate as for congelation ice. Several explanations for this discrepancy were advanced, primarily due to the unknown state of the sea surface temperature prior to the freezing event (was it immediately 'ready to freeze' at the onset

of the cold air outbreak?) and possible melting of the frazil and pancake cover between the two formation periods which the poor ECMWF 2 m air temperatures during that period cannot adequately constrain.

The oscillatory motion at high frequencies, which appeared so dramatic in the DKPs for the outer array, did not significantly enhance ice production in the hypothetical congelation ice cover. The impact of the motion was of the same order as the fractional area undergoing the motion (8% and 5% respectively).

For frazil/pancake ice, HF motion significantly affected the partitioning of ice volume between frazil and pancake phases, through increased scavenging of the frazil crystals onto the top surface of the pancakes. The HF motion had maximum effect when the interstitial frazil thickness matched the pancake thickness at the end of the simulation. For the simulated period, this corresponded to a scavenging efficiency, ε, of 17%, at which value the proportion of pancake ice was modified from 61% (six-hour forcing) to 79% (20-minute forcing) of the total ice volume. The model did not incorporate any mechanism for enhancing ice production with HF motion in a frazil/pancake ice cover, however, since the frazil slick was assumed not to modify the sea-air heat flux from the open water value and relaxes to take up any divergent area.

5.4.1 Implications for large scale models

The main impact of this study for the modelling community has been to quantitatively demonstrate the discrepancy between ice production by congelation (as is generally the case for the Arctic) and by the frazil-pancake process (which dominates Antarctic ice production), with the latter rate being generally double the congelation value.

Such a discrepancy will seriously impact large-scale modelling attempts to simulate heat and momentum fluxes between the ocean and atmosphere, as well as salt rejection and subsequent water mass modification. Failure to properly account for these processes can have dramatic results in the peak of the growth season: Hibler and Ackley (1983) found that their model under-represented ice coverage by over one million square kilometres and the actual ice edge advance was typically much faster than modelled.

Constraining the ice edge location with respect to satellite imagery removes the coverage shortfall, but ice volume continues to be significantly under-represented.

The agreement between the simple, rate-based, parameterisation and the more complex scavenging/transformation approach suggests that the incorporation of a simple "rate tuning factor" (=2) into large scale models would be a worthwhile enhancement.

The assumptions and empirical parameters used in this study render the conclusions open to question, however. Does the suggested rate factor hold for all cases, even those with disparate meteorological forcing, or does it just apply to this single case study? What variation can be expected? Only a robust physical parameterisation can address these questions, and future work to constrain these processes is therefore considered in the next section.

Dynamically, the inclusion of the newly-demonstrated high frequency differential motion appears unnecessary for these larger scale models. Our current, limited, understanding of the heat fluxes between ocean and atmosphere in the presence of a frazil-pancake ice cover – and hence the parameterisation in the model - suggests that convergence-divergence cycling has no effect on the overall ice production in such a system, only determining the balance between pancake and frazil ice volumes. The limited enhancement of ice production in a hypothetical congelation ice cover undergoing the same motion suggests that the effect of any 'missing' process on ice production would be minor.

5.4.2 Future work

Shortcomings of the models presented in this study have two main areas where assumptions or empirical parameterisations are required in place of robust physical justifications. These relate to (a) the value of the scavenging efficiency parameter, ε, and (b) the effect of the frazil/pancake ice cover on ocean-atmosphere heat fluxes. Future studies to address these problems are therefore discussed.

Scavenging efficiency

Accurate knowledge of the path length traversed by an individual pancake is required to constrain the scavenging efficiency. Uncertainties arise in two phases of the motion: (a) the oscillation observed in the DKPs, where even the mechanism responsible for the pancakes' motion on the 20 minute timescale is undetermined; and (b) the smaller-scale displacements which take place as swell waves move through the ice cover.

In the first instance, the post-SA era GPS accuracy can be exploited to decrease the interval between position measurements still further, to around one minute. This sampling rate would determine whether oscillation occurred at internal-wave periods (10-15 minutes), as postulated, and will give accurate 'long-period' (compared to swell wave periods) measurements of an individual pancake's path length.

Centimetric scale measurements of the separation between adjacent pancakes as swell waves move past are required to examine compression/rarefaction at the trough/crest of the waves and the down-wave motion. Tank experiments form an obvious first step, though attempts by other investigators have been inconclusive. Field measurements are more difficult to achieve, though video photography from a hovering helicopter is suggested, possibly using marked pancakes (*e.g.* red dye or chalk powder).

The partitioning between top-layer growth and bottom or lateral accretion is also crucial to assigning the correct importance to the scavenging process. Again, tank measurements are the obvious way forward. A first attempt at this was made by the author in the Hamburg ice tank in 2001, placing markers on the top of growing pancakes and observing subsequent top layer growth, as reported in Doble *et al*. (2003). A more systematic approach is required which also marks the bottom surface, and this will be done in future experiments at the same facility.

Ocean-atmosphere heat fluxes

Heat flux measurements over a growing pancake-frazil ice cover are required to resolve these problems, relating the measured heat flux to that which would be expected in the absence of the ice cover. The author is not aware of any such field measurements to date, and the unique nature of the ice cover makes the usual measurement methods

difficult to apply. Over consolidated pack ice, turbulent heat fluxes are usually measured from meteorological buoys with air temperature and wind speed sensors at two heights (usually 2m and 4m). The turbulent heat fluxes can then be calculated by Monin-Obukov similarity theory (e.g. Vihma *et al.* 2002).

Such buoy-based measurements are difficult or impossible in a growing pancake ice field, partly due to stability of the buoy in the wavefield (any inclination will wildly vary the measurement height), partly due to the variation of the buoy's height with respect to the atmospheric boundary layer as it rises and falls in the waves and partly due to icing from the freezing spray encountered there. Instrumented turbulence masts on ships suffer the same problems as the vessel pitches in the waves – such masts are always carefully dismounted and covered when outside the pack ice in freezing conditions (pers. obs.) for just these reasons.

Aircraft-based observations remain feasible, however, either using towed sondes from helicopters (Vihma *et al.* 2005) or instrumented fixed-wing aircraft. Measurements require co-ordination with *in situ* observations of pancake and frazil thickness, as has been done for investigations of leads in pack ice (e.g. Lüpkes *et al.* 2004). A series of measurements over varying area fractions of frazil and pancake ice are required to untangle the effects of the frazil and pancake fractions, *i.e*. whether the area covered by pancakes contributes to the heat fluxes in the same manner as the frazil slick on the integrated timescales of interest, as postulated. Transects perpendicular to the ice edge, from open water to pack ice, are suggested as the most valuable measurements to resolve this issue.

References

Alam, A. and J. A. Curry (1998). Evolution of new ice and turbulent fluxes over freezing winter leads. *J. Geophys. Res.* **103**(C8): 15,783-15,802.

Andreas, E. L. and Claffey (1995). Air-ice drag coefficients in the Western Weddell Sea. *J. Geophys. Res.* **100**(C3): 4821-4831.

Armstrong, T., B. Roberts and C. Swithinbank (1973). *Illustrated Glossary of Snow and Ice*. Cambridge, Scott Polar Research Institute/UNESCO.

Bauer, J. and S. Martin (1983). A model of grease ice growth in small leads. *J. Geophys. Res.* **88**(C5): 2912-2925.

Budillon, G., G. Fusco and G. Spezie (2000). A study of surface heat fluxes in the Ross Sea (Antarctica). *Antarctic Science* **12**(2): 243-254.

Clarke, D. B. and S. F. Ackley (1984). Sea ice structure and biological activity in the Antarctic marginal ice zone. *J. Geophys. Res.* **89**(C2): 2087-2095.

Cox, G. F. N. and W. F. Weeks (1988). Numerical simulations of the profile properties of undeformed first-year sea ice during the growth season. *J. Geophys. Res.* **93**(C10): 12,449-12,460.

Crane, D. and P. Wadhams (1996). Sea-ice motion in the Weddell Sea from drifting buoy and AVHRR data. *J. Glaciol.* **42**(141): 249-254.

Crane, D. R. and S. Wells (1994). *Sea ice kinematics data collection for use in empirical modelling*. Oceanology International, Kingston upon Thames, Spearhead Exhibitions Ltd.

Dethleff, D. (2005). Entrainment and export of Laptev Sea ice sediments, Siberian Arctic. *J. Geophys. Res.* **110**(C07009): doi:10.1029/2004JC002740.

Doble, M., M. Coon and O. Peppe (2001). Study of the winter Antarctic marginal ice zone. *Berichte zur Polar- und Meeresforschung* **402**: 158-161.

Doble, M. J., M. D. Coon and O. Peppe (2000). Cruise Report: F/S Polarstern ANT-XVII/3. Cambridge, Scott Polar Research Institute.

Doble, M. J., M. D. Coon and P. Wadhams (2003). Pancake ice formation in the Weddell Sea. *J. Geophys. Res.* **108**(C7): doi: 10.1029/2002JC001373.

Doble, M. J. and P. Wadhams (2006). Dynamical contrasts between pancake and pack ice, investigated with a drifting buoy array. *J. Geophys. Res.* **111**(C11S24): doi:10.1029/2005JC003320.

Drucker, R., S. Martin and R. Moritz (2003). Observations of ice thickness and frazil ice in the St. Lawrence island polynya from satellite imagery, upward looking sonar and salinity/temperature moorings. *J. Geophys. Res.* **108**(C5): doi:10.1029/2001JC001213.

ECMWF (1997). The description of the ECMWF/WCRP Level III-A Global Atmospheric Data Archive. Reading, U.K., European Centre for Medium-range Weather Forecasts.

Eicken, H. (1992). Salinity profiles of Antarctic sea ice: field data and model results. *J. Geophys. Res.* **97**(C10): 15,545-15,557.

Emery, W. J. and R. E. Thomson (1998). *Data Analysis Methods in Physical Oceanography*. Oxford, Pergamon.

Frankenstein, S. (1996). The effects of waves on pancake ice. *Dept. of Civil and Environmental Eng.* New York, Clarkson University. **Ph.D.:** 244.

Geiger, C. A., S. F. Ackley and W. D. Hibler III (1998). Sea ice drift and deformation processes in the Western Weddell Sea. *Antarctic Sea Ice: Physical Processes, Interactions and Variability*. M. O. Jeffries. Washington D.C., Amer. Geophys. U. **74:** 141-160.

Geiger, C. A., Y. Zhao, A. K. Liu and S. Hakkinen (2000). Large scale comparison between buoy and SSM/I drift and deformation in the Eurasian Basin during winter 1992-1993. *J. Geophys. Res.* **105**(C2): 3357-3368.

Gordon, A. L. and B. A. Huber (1990). Southern Ocean winter mixed layer. *J. Geophys. Res.* **95**(C7): 11,655-11,672.

Gow, A. J., S. F. Ackley, K. R. Buck and K. M. Golden (1987). Physical and structural characteristics of Weddell Sea pack ice. Hanover, N.H., Cold Regions Res. and Eng. Lab.

Guest, P. S. and K. L. Davidson (1991). The aerodynamic roughness of different types of sea ice. *J. Geophys. Res.* **96**(C3): 4709-4721.

Guest, P. S., J. W. Glendening and K. L. Davidson (1995). An observational and numerical study of wind stress variations within marginal ice zones. *J. Geophys. Res.* **100**(C6): 10,887-10,904.

Haapala, J. and M. Leppäranta (1996). Simulations of the Baltic Sea ice season with a coupled ice ocean model. *Tellus* **48A**: 622-643.

Haarpaintner, J., J.-C. Gascard and P. M. Haugen (2001). Ice production and brine formation in Storfjorden, Svalbard. *J. Geophys. Res.* **106**(C7): 14,001-14,013.

Hammar, L. and H. T. Shen (1995). Frazil evolution in channels. *J. Hydraulic Res.* **33**: 291-306.

Hanley, T. O. D. and G. Tsang (1984). Formation and properties of frazil in saline water. *Cold Regions Science and Technology* **8**: 209-221.

Hibler III, W. D. and S. F. Ackley (1983). Numerical simulation of the Weddell Sea pack ice. *J. Geophys. Res.* **88**(C5): 2873-2887.

Hibler III, W. D., W. F. Weeks, A. Kovacs and S. F. Ackley (1974). Differential sea ice drift I: Spatial and temporal variations in sea ice deformation. *J. Glac.* **13**(69): 437-455.

Hoeber, H. (1991). Sea-ice dynamics in the Weddell Sea in winter. *Ann. Glaciol.* **15**: 9-16.

Holland, P. R., D. L. Feltham and S. F. Daly (2007). On the Nusselt number for frazil ice growth - a correction to "Frazil evolution in channels" by Lars Hammer and Hung-Tao Shen. *J. Hydraulic Res.* **45**(3): 421-424.

Hopkins, M. A. (1998). Four stages of pressure ridging. *J. Geophys. Res.* **103**(C10): 21,883-21,891.

Hopkins, M. A. and H. H. Shen (2001). Simulation of pancake ice dynamics in a wave field. *Ann. Glaciol.* **33**: 355-360.

Kempema, E. W. and D. Dethleff (2006). The role of Langmuir circulation in suspension freezing. *Ann. Glaciol.* **44**: 58-62.

Koentopp, M., O. Eisen, C. Kottmeier, L. Padman and P. Lemke (2005). Influence of tides on sea ice in the Weddell Sea: Investigations with a high-resolution dynamic-thermodynamic model. *J. Geophys. Res.* **110**(C02014): doi:10.1029/2004JC002405.

Kondo, J. (1975). Air-sea bulk transfer coefficients in diabatic conditions. *Boundary Layer Meteorol.* **9**: 91-112.

Kottmeier, C., S. F. Ackley, E. Andreas, D. Crane, H. Hoeber, J. King, J. Launianen, D. Limbert, D. Martinson, R. Roth, L. Sellmann, P. Wadhams and T. Vihma (1997). Wind, temperature and ice motion statistics in the Weddell Sea. Geneva, World Climate Research Programme.

Kottmeier, C., J. Olf, W. Frieden and R. Roth (1992). Wind forcing and ice motion in the Weddell Sea region. *J. Geophys. Res.* **97**(D18): 20,373-20,383.

Kottmeier, C. and L. Sellmann (1997). Buoy based observations of mixed layer variability in the Weddell Sea. Cambridge, International Programme for Antarctic Buoys.

Laevestu, T. (1960). Factors affecting the temperature of the surface layer of the sea. *Commentat. Phys. Math.* **25**: 1-36.

Lange, M. A., S. F. Ackley, P. Wadhams, G. S. Dieckmann and H. Eicken (1989). Development of sea ice in the Weddell Sea. *Ann. Glaciol.* **12**: 92-96.

Lange, M. A. and H. Eicken (1991). Textural characteristics of sea ice and the major mechanisms of ice growth in the Weddell Sea. *Ann. Glaciol.* **15**: 210-215.

Lange, M. A., P. Schlosser, S. F. Ackley, P. Wadhams and G. S. Dieckmann (1990). ^{18}O concentrations in sea ice of the Weddell Sea, Antarctica. *J. Glaciol.* **36**(124): 315-323.

Large, W. G. and S. Pond (1982). Sensible and latent heat flux measurements over the ocean. *J. Phys. Oceanog.* **12**: 464-482.

Lebedev, V. V. (1938). Rost l'do v arkticheskikh rekakh i moriakh v zavisimosti ot otritsatel'nykh tempertur vozdukha. *Problemy Arktiki* **5**: 9-25.
Leonard, G. H., H. Shen and S. F. Ackley (1998a). *Dynamic growth of a pancake ice cover*. 14th International Symposium on Ice: Ice in Surface Waters, Potsdam, New York, Balkema.
Leonard, G. H., H. H. Shen and S. F. Ackley (1998b). Initiation and evolution of pancake ice in a wave field. *Antarctic J.* **33**.
Leppäranta, M. (1998). The dynamics of sea ice. *The Physics of Ice Covered Seas*. M. Leppäranta. Helsinki, Helsinki University. **1:** 305-342.
Leppäranta, M. (2005). *The Drift of Sea Ice*. Chichester, Springer.
Leppäranta, M. and W. D. Hibler (1987). Mesoscale sea ice deformation in the Greenland Sea marginal ice zone. *J. Geophys. Res.* **92**(C7): 7060-7070.
Leppäranta, M., Z. Zhanhai, J. Haapala and T. Stipa (2001). Sea-ice kinematics measured with GPS drifters. *Ann. Glac.* **44**: 151-156.
Lindsay, R. W. (2002). Ice deformation near SHEBA. *J. Geophys. Res.* **107**(C10): doi: 10.1029/2000JC000445.
Liu, A. K., P. W. Vachon, C. Y. Peng and A. S. Bhogal (1992). Wave attenuation in the marginal ice zone during LIMEX. *Atmos. Ocean* **30**(2): 192-206.
Longuet-Higgins, M. S. and R. H. Stewart (1964). Radiation stresses in water waves; a physical discussion, with applications. *Deep Sea Res.* **11**: 529-562.
Lüpkes, C., J. Hartmann and G. Birnbaum (2004). Convection over Arctic leads. *Berichte zur Polar- und Meeresforschung*(481): 47-62.
Lytle, V. I. and S. F. Ackley (1996). Heat flux through sea ice in the western Weddell Sea: convective and conductive transfer processes. *J. Geophys. Res.* **101**(C4): 8853-8868.
Markus, T., C. Kottmeier and E. Fahrbach (1998). Ice formation in coastal polynyas in the Weddell Sea and their impact on oceanic salinity. *Antarctic Sea Ice: Physical Processes, Interactions and Variability*. M. O. Jeffries. Washington D.C., Amer. Geophys. U. **74:** 273-292.
Martin, S. (1981). Frazil ice in rivers and oceans. *Ann. Rev. Fluid Mech.* **13**: 379-397.
Martin, S. and P. Kaufmann (1981). A field and laboratory study of wave damping by grease ice. *J. Glaciol.* **27**(96): 283-313.
Martinson, D. G. (1990). Evolution of the Southern Ocean winter mixed layer and sea ice: open ocean deepwater formation and ventilation. *J. Geophys. Res.* **95**(C7): 11,641-11,654.
Martinson, D. G. and R. A. Iannuzzi (1998). Antarctic ice-ocean interaction: Implications from bulk property distributions in the Weddell Gyre. *Antarctic Sea Ice: Physical Processes, Interactions and Variability*. M. O. Jeffries. Washington D.C., Amer. Geophys. U. **74:** 243-272.
Massom, R. A. (1992). Observing the advection of sea ice in the Weddell Sea using buoy and satellite passive microwave data. *J. Geophys. Res.* **97**(C10): 15,559-15,572.
Maykut, G. A. (1978). Energy exchange over young sea ice in the central Arctic. *J. Geophys. Res.* **83**(C7): 3646-3654.
Maykut, G. A. (1982). Large-scale heat exchange and ice production in the central Arctic. *J. Geophys. Res.* **87**: 7971-7984.
Maykut, G. A. (1986). The surface heat and mass balance. *The Geophysics of Sea Ice*. N. Untersteiner. Washington, Plenum Press. **146**.
Maykut, G. A. and P. E. Church (1973). Radiation climate of Barrow, Alaska, 1962-1966. *J. Appl. Meteorol.* **12**: 620-628.
Maykut, G. A. and D. K. Perovich (1987). The role of shortwave radiation in the summer decay of a sea ice cover. *J. Geophys. Res.* **92**(C7): 7032-7044.
McPhee, M. (1987). A time-dependent model for turbulent transfer in a stratified oceanic boundary layer. *J. Geophys. Res.* **92**(C7): 6977-6986.
McPhee, M., C. Kottmeier and J. H. Morison (1999). Oceanic heat flux in the central Weddell Sea during winter. *J. Phys. Oceanog.* **29**: 1166-1179.

McPhee, M. G. (1980). An analysis of pack ice drift in summer. *Sea Ice Processes and Models*. R. S. Pritchard. Seattle, University of Washington Press**:** 62-75.
Meldrum, D. T., D. J. L. Mercer and O. C. Peppe (2000). *Orbcomm - an Antarctic evaluation*. Developments in Buoy Technology, Communications and Data Applications: DBCP Scientific and Technical Workshop, Victoria, Canada, WMO, Geneva.
Muench, R. D., P. H. LeBlond and L. E. Hachmeister (1983). On some possible interactions between sea ice and waves in the marginal ice zone. *J. Geophys. Res* **88**(C5): 2819-2826.
Newyear, K. and S. Martin (1997). A comparison of theory and laboratory measurements of wave propagation and attenuation in grease ice. *J. Geophys. Res.* **102**(C11): 25,091-25,099.
Onstott, R. G., P. Gogineni, A. J. Gow, T. C. Grenfell, K. C. Jezek, D. K. Perovich and C. T. Swift (1998). Electromagnetic and physical properties of sea ice formed in the presence of wave action. *IEEE Trans. Geosci. Rem. Sens.* **36**(5): 1764-1783.
Osterkamp, T. E. (1978). Frazil ice formation: A review. *Proc. Amer. Soc. of Civil Engineers*: 1239-1255.
Padman, L. and C. Kottmeier (2000). High-frequency ice motion and divergence in the Weddell Sea. *J. Geophys. Res.* **105**(C2): 3379-3400.
Pedersen, L. T. and M. D. Coon (2004). A sea ice model for the marginal ice zone with an application to the Greenland Sea. *J. Geophys. Res.* **109**(C03008): doi:10.1029/2003JC001827.
Rogers, R. R. and M. K. Yau (1989). *A Short Course in Cloud Physics*. Oxford, Pergamon Press.
Rothrock, D. A., Y. Yu and G. A. Maykut (1999). Thinning of the Arctic sea ice cover. *Geophys. Res. Lett.* **26**(23): 3469-3472.
Rudels, B., H. J. Friedrich, D. Hainbucher and G. Lohmann (1999). On the parameterisation of oceanic sensible heat loss to the atmosphere and to ice in an ice-covered mixed layer in winter. *Deep Sea Res.* **46**(6-7): 1385-1426.
Ruhmer, R. R., R. Crissman and A. Wake (1979). Ice transport in the Great Lakes. Ann Arbor, Great Lakes Env. Res. Lab.
Shen, H. H. and S. F. Ackley (1995). A laboratory-produced pancake ice cover in a two-dimensional wave field. *Antarctic J.* **30**: 106-107.
Shen, H. H., S. F. Ackley and M. A. Hopkins (2001). A conceptual model for pancake ice formation in a wave field. *Ann. Glaciol.* **33**: 361-367.
Shen, H. H. and V. A. Squire (1998). Wave damping in compact pancake ice fields due to interactions between pancakes. *Antarctic Sea Ice: Physical Processes and Variability*. M.O.Jeffries. Washington, Amer. Geophys. U. **74:** 325-341.
Simonsen, K. and P. M. Haugan (1996). Heat budgets of the Arctic Mediterranean and sea surface heat flux parameterizations for the Nordic Seas. *J. Geophys. Res.* **101**(C3): 6553-6576.
Smedsrud, L. H. (2001). Frazil ice entrainment of sediment: large-tank laboratory experiments. *J. Glac.* **47**(158): 461-471.
Smedsrud, L. H. and A. Jenkins (2004). Frazil ice formation in an ice shelf water plume. *J. Geophys. Res.* **109**(C03025): doi:10.1029/2003JC001851.
Smedsrud, L. H. and R. Skogseth (2006). Field measurements of Arctic grease ice properties and processes. *Cold Reg. Sci. & Tech.* **44**: 171-183.
Smith, S. D. (1988). Coefficients for sea surface wind stress, heat flux and wind profiles as a function of wind speed and temperature. *J. Geophys. Res.* **93**(C12): 15,467-15,472.
Squire, V. A. (1998). The marginal ice zone. *The Physics of Ice Covered Seas*. M. Leppäranta. Helsinki, University of Helsinki. **1:** 381-446.
Tenhunan, T., T. Vihma and M. J. Doble (2007). Mesoscale modelling of the atmosphere over Antarctic sea ice: a case study. *Monthly Weather Rev.* **In press**.

Thomas, D. (1999). The quality of sea ice velocity estimates. *J. Geophys. Res.* **104**(C6): 13,627-13,652.
Thomas, D. N. and J. P. Wilkinson (2001). European ARCTELAB large scale facility: Final report, INTERICE 3. Bangor, University of Wales.
Thorndike, A. S. and R. Colony (1982). Sea ice motion in response to geostrophic winds. *J. Geophys. Res.* **87**(C8): 5845-5852.
Thorndike, A. S., D. A. Rothrock, G. A. Maykut and R. Colony (1975). The thickness distribution of sea ice. *J. Geophys. Res.* **80**(33): 4501-4513.
Tison, J.-L. and V. Verbeke (2001). Chlorinity/salinity distribution patterns in experimental granular sea ice. *Ann. Glaciol.* **33**: 13-20.
Torrence, C. and G. P. Compo (1998). A practical guide to wavelet analysis. *Bull. of the Amer. Met. Soc.* **79**(1): 61-78.
Uotila, J., T. Vihma and J. Launianen (2000). Response of the Weddell Sea pack ice to wind forcing. *J. Geophys. Res.* **105**(C1): 1135-1151.
Ushio, S. and M. Wakatsuchi (1993). A laboratory study on supercooling and frazil ice production processes in winter coastal polynyas. *J. Geophys. Res.* **98**(C11): 20,321-20,328.
Vihma, T. and J. Launianen (1993). Ice drift in the Weddell Sea in 1990-1991 as tracked by a satellite buoy. *J. Geophys. Res.* **98**(C8): 14,471-14,485.
Vihma, T., J. Launianen and J. Uotila (1996). Weddell Sea ice drift: kinematics and wind forcing. *J. Geophys. Res.* **101**(C8): 18,279-18,296.
Vihma, T., C. Lüpkes, J. Hartmann and H. Sarvijarvi (2005). Modelling of cold-air advection over Arctic sea ice in winter. *Boundary Layer Met.* **117**(2): 275-300.
Vihma, T., J. Uotila, B. Cheng and J. Launianinen (2002). Surface heat budget over the Weddell Sea: buoy results and model comparisons. *J. Geophys. Res.* **107**(C2): 10.1029/2000JC000372.
Voropayev, S. I., H. J. S. Fernando and L. A. Mitchell (1995). On the rate of frazil ice formation in Polar regions in the presence of turbulence. *J. Phys. Oceanog.* **25**: 1441-1450.
Wadhams, P. (1973). Attenuation of swell by sea ice. *J. Geophys. Res.* **78**: 3552-3563.
Wadhams, P., J. C. Comiso, E. Prussen, S. Wells, M. Brandon, E. Aldworth, T. Viehoff, R. Allegrino and D. R. Crane (1996). The development of the Odden ice tongue in the Greenland Sea during winter 1993 from remote sensing and field observations. *J. Geophys. Res.* **101**(C8): 18,213-18,235.
Wadhams, P. and N. R. Davis (2000). Further evidence of ice thinning in the Arctic Ocean. *Geophys. Res. Lett.* **27**(24): 3973-3975.
Wadhams, P., M. A. Lange and S. F. Ackley (1987). The ice thickness distribution across the Atlantic sector of the Antarctic Ocean in midwinter. *J. Geophys. Res.* **92**(C13): 14,535 - 14,552.
Wadhams, P. and V. A. Squire (1986). The effect of the marginal ice zone on the directional wave spectrum of the ocean. *J. Phys. Oceanog.* **16**(2): 358 - 376.
Wadhams, P., V. A. Squire, D. J. Goodman, A. M. Cowan and S. C. Moore (1988). The attenuation rates of ocean waves in the marginal ice zone. *J. Geophys. Res.* **93**(C6): 6799-6818.
Wadhams, P. and J. P. Wilkinson (1999). The physical properties of sea ice in the Odden ice tongue. *Deep Sea Res.* **46**(6-7): 1275-1301.
Wakatsuchi, M. and N. Ono (1983). Measurements of salinity and volume of brine excluded from growing sea ice. *J. Geophys. Res.* **88**: 2943-2951.
Wamser, C. and D. G. Martinson (1993). Drag coefficients for winter Antarctic pack ice. *J. Geophys. Res.* **98**(C7): 12,431-12,437.
Warren, S. G., C. S. Roesler, V. I. Morgan, R. E. Brandt, I. D. Goodwin and I. Allison (1993). Green icebergs formed by freezing of organic-rich seawater to the base of Antarctic ice shelves. *J. Geophys. Res.* **98**(C4): 6921-6928.

Weeks, W. F. (1998). Growth conditions and structure and properties of sea ice. *Physics of Ice Covered Seas*. M. Leppäranta. Helsinki, University of Helsinki. **1:** 25-105.
Weller, G. (1972). Radiation flux investigation. *AIDJEX Bulletin* **14**: 28-30.
Wilkinson, J. P. (2005). Sea ice, convection and the Greenland Sea. *School of Ocean & Earth Science*. Southampton, University of Southampton. **Ph.D.:** 257.
Wilkinson, J. P. and P. Wadhams (2003). A salt flux model for salinity change through ice production in the Greenland Sea and its relationship to winter convection. *J. Geophys. Res.* **108**(C5): doi:10.1029/2001JC001099.
Winsor, P. and G. Björk (2000). Polynya activity in the Arctic Ocean from 1958 to 1997. *J. Geophys. Res.* **105**(C4): 8789-8803.
Worby, A. P. and I. Allison (1991). Ocean-atmosphere energy exchange over thin, variable concentration Antarctic pack ice. *Ann. Glac.* **15**: 184-190.

Appendix A: Wavelet algorithm details

A Morlet wavelet was used, since it is (a) non-orthogonal; most commonly used in time series analysis where smooth continous variations in wavelet amplitude are expected, and (b) complex, to return phase and amplitude information – better adapted for capturing oscilliatory behaviour (Torrence and Compo 1998). The Morlet wavelet has the additional advantage that its scale s is almost equivalent to the Fourier period λ for the commonly used mother wavenumber of 6 (in fact $\lambda = 1.03s$).

Scales are chosen such that the smallest (s_0) is equal to the Nyquist frequency, $2\Delta t$, or 40 minutes. The largest scale should be less than half the total length of the timeseries, and we choose a scale equivalent to the duration of the pancake phase, O(10 days). The family of scales is defined as

$$s_j = s_0 . 2^{j \delta j} \qquad \text{(Eq. A.1)}$$

where δj is the sub-scale interval. Choosing δj = 0.25 gives sufficient resolution between scales and implies a maximum j of 64, corresponding to a maximum scale of approximately 7 days.

Time series are padded with zeroes to the next largest power of two samples, in order to remove edge effects for large scale wavelets. Zero-padding introduces edge effects of its own, however, decreasing the wavelet power at larger scales as more zeroes enter the analysis. The "*cone of influence*", or the region where edge effects become important, is therefore marked. It is defined as the *e*-folding time for the autocorrelation of wavelet power at each scale.

To determine significance levels (and remove the major objection to wavelet analysis) it is necessary to determine the background spectrum on top of which the signal of interest is imposed. The spectral analysis of the preceding section suggested a red noise

background – *i.e*. having increasing power with decreasing frequency. This background spectrum can be modelled as:

$$P_k = \frac{1-\alpha^2}{1+\alpha^2-2\alpha\cos\left(2\pi k/M\right)} \qquad \text{(Eq. A.2)}$$

where $k = 0 \ldots M/2$ is the frequency index and α is the 'assumed lag-1 autocorrelation' (Torrence & Compo, 1998). This lag-1 autocorrelation is given by (Emery & Thompson, 1998):

$$\alpha = \frac{1}{N-1}\sum_{n=1}^{N-1} y_n y_{n+1} \qquad \text{(Eq. A.3)}$$

An alpha value of zero gives a white noise spectrum and a value of 1 gives a pure red noise spectrum. The velocity spectra in the present study deviate only slightly from this latter log-log linearity, and this is confirmed by their α values close to unity, typically 0.97-0.98. If a peak in the wavelet power spectrum is above this background level, it can be assumed to be a true feature at a given confidence level. The confidence testing performed here assumes a normally distributed random input variable, choosing the confidence level as the chi-squared percentile at two degrees of freedom. This assumption is justified in the case of the component velocities, but not in the case of scalar speeds, since these appear to have Rayleigh distribution instead.

Appendix B: Thermodynamic model details

This Appendix gives details of the equations underlying the thermodynamic ice growth model described in Chapter 3. The model is one dimensional and treats the ice as a homogenous conducting slab. Figure B.1 shows the various heat fluxes at the top and bottom surfaces of the ice.

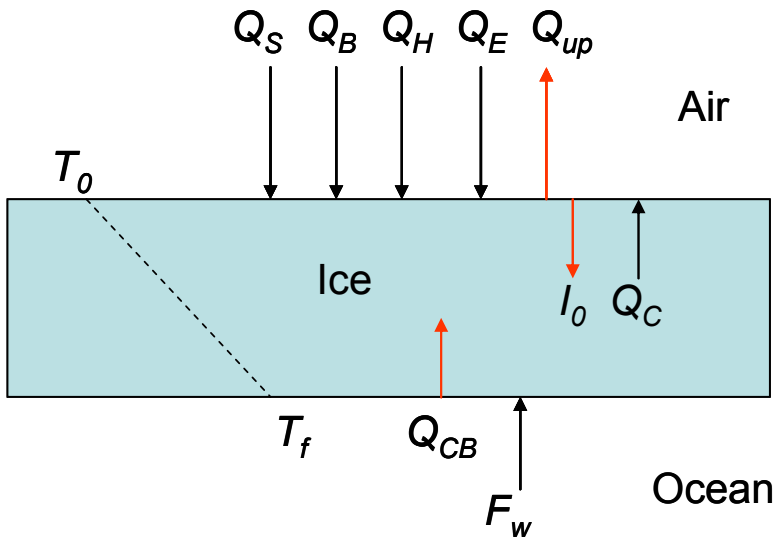

Figure B.1: The model scheme, showing heat fluxes at top and bottom surfaces of the ice. A linear temperature profile is indicated, from T_0, the surface ice temperature to T_f, the freezing point of seawater, at the bottom surface. Negative terms (away from an interface) are shown in red.

At the top surface of the ice the heat fluxes are:

$$Q_S - I_0 + Q_B - Q_{up} + Q_H + Q_E + Q_C = Q_{net} \qquad \text{(Eq. B.1)}$$

Where α is the albedo, Q_S is the downwelling SW radiation flux, I_0 is the SW radiation which penetrates the ice, Q_B is the downwelling longwave (LW) radiation flux from the

air, Q_{up} is the upwelling LW radiation flux from the ice surface, Q_H is the sensible heat flux, Q_E is the latent heat flux and Q_C is the conductive heat flux upward to the ice surface. Terms away from the surface are negative, those towards the surface are positive, as commonly used in ice modelling. The sum is zero if the ice surface is below freezing point, with the balance determined by the (unknown) ice surface temperature, T_0 (Maykut 1986).

Terms which do not depend on T_0 (independent terms; Q_S, I_0, Q_B) are solved first, the equation (B.1) is solved iteratively to give T_0 . If the melting temperature (-0.6°C at an assumed constant salinity of 11 psu, as observed for the pancakes) is reached without balance being achieved – i.e. Q_{net} is still on a downward trend – the surface temperature is set to this melting value (Simonsen and Haugan 1996) and the unbalanced flux is used to melt ice on the top surface according to the equation:

$$\frac{\partial h_{top}}{\partial t} = -\frac{Q_{net}}{\rho_i L} \qquad \text{(Eq. B.2)}$$

where L is the latent heat of fusion, taken as that for ice with 10% brine volume = 295.8 kJ kg^{-1} (Haarpainter *et al*, 2001). The negative sign indicates that a positive Q_{net} (towards the air-ice interface) will reduce ice thickness. In fact, top melt never occurred during the period of interest, with all ice thickness reductions coming from bottom melt instead.

At the bottom surface the situation is simpler, with just the ocean-ice heat flux (F_{w} , positive from the ocean to the ice) and the conductive heat flux from the ocean to the ice (Q_{CB} , negative away from the ice-ocean interface) contributing. No balance occurs, and the net heat flux at the bottom surface of the ice either grows or melts ice depending on its sign. The bottom surface of the ice is assumed to be at the freezing temperature of seawater (T_f = -1.89°C) for the measured mixed-layer salinity (34.35 psu, held constant). The rate of change in ice thickness at the bottom surface is then given by (Maykut and Perovich 1987):

$$\frac{\partial h}{\partial t} = -\frac{1}{\rho_i L}\left(Q_{CB} + F_w\right) \qquad \text{(Eq. B.3)}$$

where h is the ice thickness (m), ρ_i is the density of ice (taken as 920 kg m^{-3}) and L is the latent heat of fusion, 295.8 kJ kg^{-1} - equivalent to ice containing 10% brine volume (Haarpaintner *et al.* 2001). Estimates of F_w in the study area range from 5 Wm^{-2} (Lytle and Ackley 1996), through 27.4 Wm^{-2} (McPhee *et al.* 1999) to more than 40 Wm^{-2} (Gordon and Huber 1990). An intermediate value of 25 Wm^{-2} (Martinson 1990; Martinson and Iannuzzi 1998) is used, since the relatively thick pycnocline at the beginning of winter will reduce the heat flux to well below its maximum value.

Frazil ice growth was accomplished using a similar scheme, omitting the conduction terms and setting $T_0 = T_f$. The equation, balanced by the ice formation and taking heat gain by the ocean as positive, becomes:

$$Q_H + Q_E + Q_B - Q_{up} + Q_S = -\rho_i L \frac{\partial h}{\partial t} \qquad \text{(Eq. B.4)}$$

where $\frac{\partial h}{\partial t}$ is the frazil formation rate in metres per second of equivalent solid ice and L is the latent heat of fusion for frazil ice. The value for L is problematic since sea ice is a multiphase medium which changes its volume of brine inclusion both instantaneously during the formation of frazil and over the longer ageing process undergone by pancakes and consolidated ice. Haarpainter *et al* (2001) took the value for ice crystals forming in freezing seawater given by Markus *et al*. (1998); 234.14 kJ kg^{-1} and this is followed in the current model. The value is considerably less than used for the congelation ice growth process (L = 295.8 kJ kg^{-1}). The ice density, ρ_f, is taken as 950 kg m^{-3} (Martin and Kaufmann 1981). This is higher than the value taken for congelation ice, since the crystals are considered as a solid mass, lacking the 10% brine volume assumed for the consolidated ice.

The detailed derivations of the individual fluxes are next discussed.

Independent terms

The downwelling short-wave radiation flux (sum of direct and diffuse) is derived from the Q_{S0}, or "global radiation" term modified by the albedo of the surface, α, calculated for young ice (Maykut 1982):

$$Q_S = (1-\alpha)\, Q_{S0} \qquad \text{(Eq. B.5)}$$

where

$$\alpha = 0.08 + 0.44h^{0.28} \qquad \text{(Eq. B.6)}$$

and h is the ice thickness in m. Albedo is calculated as that of snow-free thin-ice (Weller 1972). For the times when the ship was not on station, the shortwave downwelling flux is derived from basic equations:

$$Q_{so} = T_r S_0 \cos\eta \qquad \text{(Eq. B.7)}$$

T_r is the clear-sky transmittance, S_0 the solar constant (1353 Wm^{-2}) and $\cos\ \eta$ the solar zenith angle. T_r is usually taken from the Zillman model most commonly used for polar conditions, e.g. (Markus *et al.* 1998). An alternative formulation, which gives higher T_r, was developed from this model for polar regions (Budillon *et al.* 2000). Though less commonly used in the literature, it is a refinement of the more-widely used model and this is adopted here:

$$T_r = \frac{\cos\eta}{\cos\eta + (1+\cos\eta)e_p \times 10^{-5} + 0.046} \qquad \text{(Eq. B.8)}$$

where e_p is the water vapour pressure (in hPa or mb) at the ambient air temperature T_a. It is derived from the saturation vapour pressure over water (e_s), given by the experimentally-determined equation (Rogers and Yau 1989) below. This is valid to

within 0.1% in the range –30°C to 35°C. For this equation, T_a is required in °C rather than Kelvin:

$$e_s = 6.112 \exp\left(\frac{17.67 T_a}{T_a + 243.5}\right) \qquad \text{(Eq. B.9)}$$

The final vapour pressure is then modified by the relative humidity, given in the *in situ* data. The solar zenith angle (degrees from the vertical) is given by:

$$\cos\eta = \sin\phi \sin\iota + \cos\phi \cos\iota \cos\tau \qquad \text{(Eq. B.10)}$$

where ϕ is the latitude and ι, the solar inclination angle

$$\iota = 23.44 \cos(172 - d) \qquad \text{(Eq. B.11)}$$

where d is the day-of-year. τ is the solar hour angle,

$$\tau = 15(12 - t_s) \qquad \text{(Eq. B.12)}$$

t_s is the solar time (hours), which is 4 minutes behind UTC for every degree West of longitude:

$$t_s = UTC + lon/15 \qquad \text{(Eq. B.13)}$$

The downwelling SW flux is reduced by the cloud correction factor, C_f, which is calculated from the fractional cloud cover, T_{cc}, (Laevestu 1960):

$$C_f = 1 - 0.6\ T_{cc}^{\ 3} \qquad \text{(Eq. B.14)}$$

The measured in situ "*globRad*" is then finally obtained:

$$Q_S = Q_{s0}.C_f \qquad \text{(Eq. B.15)}$$

This short wave flux is partially absorbed by the ice, with that fraction being given by (Maykut 1982):

$$I_0 = 0.805\ Q_S \exp(-1.5h + 0.15) \qquad \text{(Eq. B.16)}$$

The net downwelling shortwave flux is therefore

$$Q_{Snet} = Q_S - I_0 \qquad \text{(Eq. B.17)}$$

The downwelling longwave flux, Q_B, is given by (Maykut and Church 1973):

$$Q_B = \varepsilon_a \sigma T_a^4 \qquad \text{(Eq. B.18)}$$

where T_a is the air temperature in Kelvin, σ is the Stephan-Boltzmann constant (5.67×10^{-8} W m^{-2} K^{-4}) and ε_a is the emissivity of the air, which increases with cloud cover fraction T_{cc}:

$$\varepsilon_a = 0.7829(1 + 0.2232\ T_{cc}^{2.75}) \qquad \text{(Eq. B.19)}$$

Dependent terms

Dependent terms are derived in an iterative loop, designed to balance the Q_{net} term at the (unknown) surface temperature, T_0. If the air temperature is less than the freezing temperature of seawater, T_f, surface temperatures between T_a and the melting temperature for ice of 11 psu (the observed value) ($T_{\text{melt}} = -0.6^{\circ}$C) are tested. If the air temperature is greater, only temperatures between T_f and T_{melt} are used. The search for T_0 and the balance of fluxes as this varies is illustrated in Figure B.2.

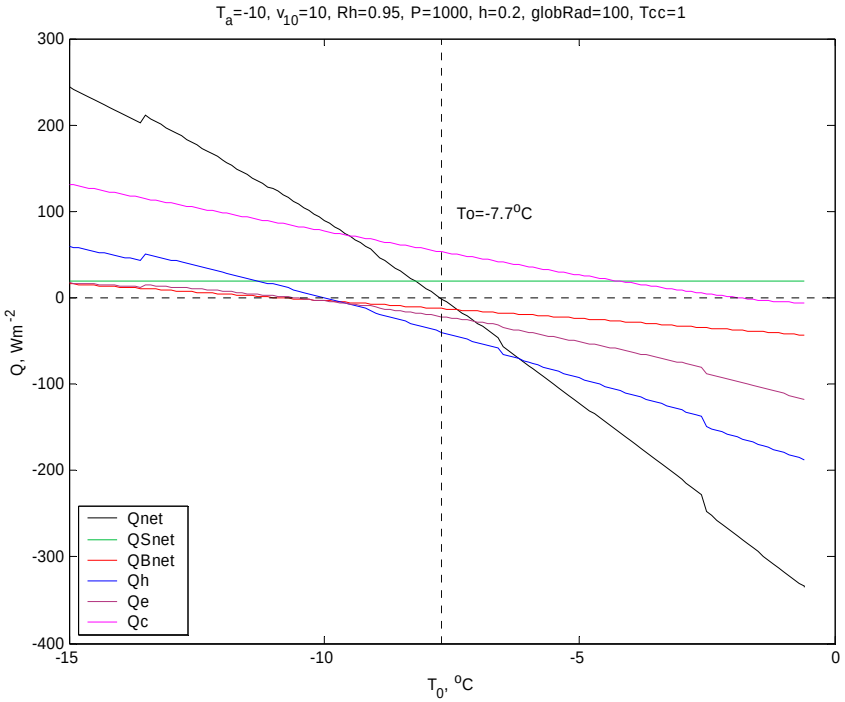

Figure B.2: Heat flux values using fixed meteorological data and varying the surface ice temperature, T_0. The net downwelling shortwave flux Q_{Snet} is fixed. The net downwelling longwave flux Q_{Bnet} is slightly positive at the lowest T_0 values, but becomes negative due to the increasing emission from the ice surface (Q_{up}) as the temperature increases. The sign of the sensible heat flux Q_H depends on the balance of the (T_a – T_0) term. The latent heat flux Q_E becomes more negative as the increasing T_0 allows the saturation specific humidity at that temperature to rise. The conduction term Q_C is positive (from ocean to atmosphere) while the air temperature is lower than the ice base temperature. The zero value of Q_{net} occurs at a surface temperature of –7.7°C in this case, between T_a (-10°C) and the freezing temperature of 34.45 psu seawater (-1.9°C). Steps in the turbulent and net fluxes arise from changes in the turbulent heat coefficient lookup values.

Q_{up}, the longwave flux upwards from the ice surface is given by:

$$Q_{up} = \varepsilon_i \sigma T_0^4 \qquad \text{(Eq. B.20)}$$

where ε_i is the emissivity of the ice surface, taken as a constant 0.97.

Q_E, the latent heat flux arising from evaporation/sublimation is given by:

$$Q_E = \rho_A L C_E \left|\overline{V}_{10}\right|(q_A - q_S) \qquad \text{(Eq. B.21)}$$

where ρ_a is the density of moist air, L is the latent heat of vaporisation (over water) or sublimation (over ice), C_E is the turbulent exchange coefficient, v_{10} is the wind speed at 10 m height. q_a and q_S are the specific humidity at T_a and the saturation specific humidity at T_0, respectively.

The saturation vapour pressure e_s is first determined over water as defined in Eq. B.9. This is valid to within 0.1% in the range –30°C to 35°C. The programme takes an additional water/ice flag, which if set to ice (= 1) corrects the saturation vapour pressure (for both temperatures) to that over ice, with T expressed in Kelvin:

$$e_i = e_s \Big/ \left(\frac{273.15}{T_a}\right)^{2.66} \qquad \text{(Eq. B.22)}$$

The vapour pressure e_p is then given by multiplying the saturation pressure by the relative humidity, which lies in the range $0 \rightarrow 1$. This is required for the T_a relation only.

Vapour pressures are then converted to specific humidities (the mass of water vapour per unit mass of moist air) according to:

$$q = \varepsilon \frac{e}{p - (1 - \varepsilon)e} \qquad \text{(Eq. B.23)}$$

where ε is the ratio of gas constants for dry air and water vapour (~0.622) and p is the atmospheric pressure. Values for the partial specific humidity at T_a and the saturated specific humidity at T_0 are calculated.

The mixing ratio (mass of water vapour per unit mass of dry air), w, at T_a is also needed and is given by

$$w = \varepsilon \frac{e}{p - e} \qquad \text{(Eq. B.24)}$$

The density of moist air at T_a is then calculated using a correction to the usual gas equation (T in Kelvin)

$$\rho_A = \frac{p}{R(1 + 0.6w)T_a} \qquad \text{(Eq. B.25)}$$

where p is the mean sea level pressure in Pa (= mb×100), T_a is in Kelvin and R is the gas constant for dry air (287 J kg^{-1} K^{-1})

L is the latent heat of vaporisation (over water) or sublimation (over ice). L over ice is virtually constant at negative temperatures, ranging from 2834 kJ kg^{-1} at 0°C to 2839 kJ kg^{-1} at –40°C. A constant figure of 2837 kJ kg^{-1}, corresponding to –10°C, is taken. The water/ice flag, if set to water, determines the temperature-dependent latent heat of vaporisation as (Rogers and Yau 1989):

$$L = (-2.4T_a + 2501) \times 10^3 \qquad \text{(Eq. B.26)}$$

The turbulent exchange coefficient C_E itself depends on wind speed and atmospheric stability. Estimates in the literature range from 1.1×10^{-3} (Large and Pond 1982) to 2.5×10^{-3} (Maykut 1978). An intermediate value of 1.75×10^{-3} was used by Budillon *et al* (2000) in the Ross Sea. A lookup table containing 7 classes of surface-air temperature difference and 6 classes of windspeed, is used to derive an appropriate value. The table is derived from an appendix by Kondo (1975). The lookup table is defined in Table B.1.

Table B.1: Look-up table for the turbulent heat coefficient C_E. Column headings give the middle range of windspeeds over which the value is defined. Row headings give the range of temperature differences (surface-air)

	2	**4**	**6.5**	**9**	**13**	**18**
20	2.0	1.9	1.8	1.7	1.5	1.4
10	2.0	1.7	1.6	1.5	1.4	1.4
5	2.0	1.6	1.5	1.4	1.4	1.3
2	2.0	1.4	1.4	1.3	1.3	1.3
0	1.1	1.1	1.2	1.2	1.2	1.2
-2	0.2	0.7	1.0	1.1	1.2	1.2
-5	0.1	0.3	0.8	0.9	1.1	1.2

Q_H, the sensible heat flux resulting from the processes of conduction and convection, is given by:

$$Q_H = \rho_A C_p C_H \left|\overline{V}_{10}\right|\left(T_a - T_0\right) \qquad \text{(Eq. B.27)}$$

where C_H is the turbulent exchange coefficient, discussed above, and C_p is the specific heat capacity of air, taken as 1004 J K^{-1} kg^{-1}. The sensible and latent heat fluxes are sometimes lumped together under the heading of "turbulent heat flux" (Haarpaintner *et al.* 2001), but are parameterised separately in this model.

Q_C, The conductive heat flux through the ice (positive towards the surface, out of the ice) is given by:

$$Q_C = \frac{\kappa_i}{h}\left(T_f - T_0\right) \qquad \text{(Eq. B.28)}$$

where κ_i is the conductivity of the ice of salinity S_i psu (T_i in ^{o}C). S_i is held constant at 11 psu.

$$\kappa_i = \kappa_0 + \frac{0.13 S_i}{T_i} \qquad \text{(Eq. B.29)}$$

and κ_0 is the conductivity of pure ice,

$$\kappa_0 = 9.828 \exp\left(-0.0057 T_i\right) \qquad \text{(Eq. B.30)}$$

The ice temperature T_i is assumed to be the mean of the surface (T_0) and base temperatures (assumed to be the freezing point, T_f).

The conductive heat flux through the bottom of the ice (Q_{CB}, positive downwards) is given in a similar manner to Equation B.28, with T_f and T_0 reversed – *i.e.* the term in brackets becomes ($T_0 - T_f$). Conductivity is calculated in an exactly similar manner.

A summary of global constants used in the programme is given in Table B.2.

Table B.2: Global constants used in the flux balance model

Symbol	Value	Description
DT	21600 s	Timestep (six hours)
HMIN	0.01 m	Minimum ice thickness
SAL_ICE	11.00 psu	Salinity of top surface of pancakes
SAL_ML	34.45 psu	Mixed layer salinity
MELT_TEMP	-1.89°C	Melting temperature of the pancake surface
FW	25 Wm^{-2}	Oceanic heat flux
RHOI	920 kg m^{-3}	Density of pancake ice
L_SUBLIM	2837 kJ kg^{-1}	Latent heat of sublimation
L_FUSION	295.8 kJ kg^{-1}	Latent heat of fusion
SIGMA	5.67×10^{-8} W m^{-2} K^{-4}	Stefan-Boltzmann constant
ABS_ZERO	-273.15 K	Absolute zero (used for °C to K conversion)
EI	0.97	Emissivity of ice
CP	1004 J K^{-1} kg^{-1}	Specific heat capacity of air